DOT/FAA/AR-10/3

Air Traffic Organization
NextGen & Operations Planning
Office of Research and
and Technology Development
Washington, DC 20591

Fatigue Crack Growth Databases and Analyses for Threshold Behavior in Rotorcraft Materials

March 2010

Final Report

This document is available to the U.S. public through the National Technical Information Services (NTIS), Springfield, Virginia 22161.

U.S. Department of Transportation
Federal Aviation Administration

NOTICE

This document is disseminated under the sponsorship of the U.S. Department of Transportation in the interest of information exchange. The United States Government assumes no liability for the contents or use thereof. The United States Government does not endorse products or manufacturers. Trade or manufacturer's names appear herein solely because they are considered essential to the objective of this report. This document does not constitute FAA certification policy. Consult your local FAA aircraft certification office as to its use.

This report is available at the Federal Aviation Administration William J. Hughes Technical Center's Full-Text Technical Reports page: actlibrary.tc.faa.gov in Adobe Acrobat portable document format (PDF).

Technical Report Documentation Page

1. Report No.	2. Government Accession No.	3. Recipient's Catalog No.
DOT/FAA/AR-10/3		

4. Title and Subtitle	5. Report Date
FATIGUE CRACK GROWTH DATABASES AND ANALYSES FOR THRESHOLD BEHAVIOR IN ROTORCRAFT MATERIALS	March 2010
	6. Performing Organization Code
7. Author(s) James C. Newman, Jr., Anthony J. Vizzini, and Yoshinori Yamada	8. Performing Organization Report No.
9. Performing Organization Name and Address Mississippi State University Mississippi State, MS 39762	10. Work Unit No. (TRAIS)
	11. Contract or Grant No.
12. Sponsoring Agency Name and Address U.S. Department of Transportation Federal Aviation Administration Air Traffic Organization NextGen & Operations Planning Office of Research and Technology Development Washington, DC 20591	13. Type of Report and Period Covered Final Report
	14. Sponsoring Agency Code ASW-112

15. Supplementary Notes

The Federal Aviation Administration Airport and Aircraft Safety R&D Division COTRs were Drs. Dy Le, Felix Abali, and John Bakuckas.

16. Abstract

Accurate representation of fatigue crack thresholds is extremely important for many rotorcraft applications. If the measured threshold is unconservatively high, then a structural component designed with these data may fail long before fatigue analyses predict. Currently, in North America, the threshold crack growth regime is experimentally defined by using ASTM Standard E 647, which has been shown to exhibit anomalies due to the load-reduction test procedure. The load-reduction test procedure has been shown to induce remote crack surface closure, which prematurely slows crack growth and produces an abnormally high threshold for some materials.

The scope of this research project was to (1) further develop the compression precracking (CP) threshold test methods, (2) determine fatigue crack growth rates in the near-threshold regime and over a wide range in rates (from threshold to near fracture) for three materials (7075-T651, Ti-6Al-4V β-STOA, and 4340 steel), and (3) analyze fatigue crack growth data on three rotorcraft materials (7050-T7451, Ti-6Al-4V β-STOA, and Mg AZ91E) tested at the National Aeronautics and Space Administration (NASA) Langley Research Center (LaRC). In addition, a few tests on the 7050 alloy were conducted at Mississippi State University (MSU) using the new threshold test methods. At MSU, three types of tests were conducted on each material: (1) ASTM E 647 load-reduction procedure, (2) CP constant-amplitude test method, and (3) CP load-reduction test method. An additional test method, CP constant-ΔK, was also used on two materials. All tests were conducted under a laboratory air environment at room temperature. Alternative methods to determine thresholds and near-threshold fatigue crack growth rate behavior for metallic materials were developed. The titanium (β-STOA) alloy showed large differences between the ASTM LR and CP tests but the 7075 and 4340 steel showed small differences.

17. Key Words	18. Distribution Statement
Fatigue, Crack growth, Thresholds, Compression, Crack closure, Stress analysis, Stress-intensity factor, Fracture toughness	This document is available to the U.S. public through the National Technical Information Service (NTIS), Springfield, Virginia 22161

19. Security Classif. (of this report)	20. Security Classif. (of this page)	21. No. of Pages	22. Price
Unclassified	Unclassified	110	

Form DOT F 1700.7 (8-72) Reproduction of completed page authorized

TABLE OF CONTENTS

		Page
EXECUTIVE SUMMARY		xiii
1.	INTRODUCTION	1
1.1	Purpose	2
1.2	Background	2
1.3	Research Objectives	3
2.	LABORATORY TEST SPECIMENS	3
3.	MATERIALS	5
3.1	Aluminum Alloy 7050-T7451	5
3.2	Aluminum Alloy 7075-T651	6
3.3	Titanium Alloy Ti-6Al-4V β-STOA	7
3.4	Magnesium Alloy AZ91E	8
3.5	Steel 4340	8
4.	TEST METHODS	9
4.1	ASTM LR Threshold Tests	10
4.2	The CP Threshold Tests	11
4.2.1	Stress-Intensity Factors Under Compressive Loading	11
4.2.2	V-Notch Effects on Stress-Intensity Factors	12
4.2.3	Crack Growth Under Compressive Loading	13
4.2.4	Residual Stresses and Stabilization of Crack-Opening Stresses	14
4.2.5	The CP and Crack Extension Criteria	17
4.2.6	Constant-ΔK Tests	17
4.2.7	The CPCA Tests	18
4.2.8	The CPLR Tests	19
4.3	Back-Face Strain Gage Crack Length Monitoring System	19
5.	MATERIALS TESTED AT MSU	19
5.1	Aluminum Alloy 7075-T651	20
5.1.1	Fatigue Crack Growth Tests	20
5.1.2	Crack Closure Analyses	24
5.2	Titanium Alloy Ti-6Al-4V β-STOA	31

5.2.1 Fatigue Crack Growth Tests (LS Orientation) 31
5.2.2 Fatigue Crack Growth Tests (SL Orientation) 34
5.2.3 Fatigue Crack Growth Tests (TS Orientation) 36
5.2.4 Validation of Crack Extension Criterion for Titanium Alloy 37
5.2.5 Comparison of Stress Ratio Data 39
5.2.6 Crack Closure Analyses 41

5.3 Steel 4340 43

5.3.1 Fatigue Crack Growth Tests 43
5.3.2 Crack Closure Analyses 51

6. MATERIALS TESTED AT NASA LaRC 57

6.1 Aluminum Alloy 7050-T7451 57

6.1.1 Fatigue Crack Growth Tests 57
6.1.2 Crack Closure Analyses 60
6.1.3 Validation of Crack Extension Criterion for 7050 Alloy 64

6.2 Titanium Alloy Ti-6Al-4V β-STOA 65

6.2.1 Fatigue Crack Growth Tests 65
6.2.2 Crack Closure Analyses 68

6.3 Magnesium Alloy AZ91E 72

7. DISCUSSION 75

8. CONCLUSIONS 77

9. REFERENCES 78

APPENDICES

A—Crack Length and Back-Face Strain Gage Relation for Compact Specimens
B—Plasticity-Induced Crack Closure Modeling

LIST OF FIGURES

Figure		Page
1	Typical Fatigue Crack Growth Data Under CA, LR, and CPCA Loading	3
2	Standard and Modified Compact Specimen Configurations	4
3	Beveled Pinhole Configuration in Compact Specimens	4
4	Crack Front Shape Near Threshold in 4340 Steel Compact Specimens	4
5	Compact Specimen Layout in Titanium Alloy Forging	7
6	Definition of ASTM E 647 LR Procedure	10
7	Compressive Loading Options on C(T) Specimens	11
8	Normalized Stress-Intensity Factors for C(T) Specimen Under Compressive Loading at Pinholes or Edges	12
9	Normalized Stress-Intensity Factors for Crack Emanating From V-Notch in Standard C(T) and M(T) Specimens	13
10	Crack Extension Under Compressive Loading for a Variety of Materials	14
11	Comparison of Crack-Opening Loads for CA and CPCA Loading	15
12	Comparison of CTODs for CA and CPCA Loading	16
13	Crack Extension Length Unaffected by Compressive Yielding	16
14	Definition of CPCK Loading	18
15	Definition of CPCA Loading	18
16	Definition of CPLR Loading	19
17	Crack Extension Under Compressive Loading for Two 7075-T651 C(T) Specimens	20
18	Fatigue Crack Growth During ASTM LR and CPCA Tests on 7075-T651 at R = 0.1	21
19	Fatigue Crack Growth During Standard and Nonstandard ASTM LR Tests	22
20	Comparison of Results From C(T) and M(T) Specimens on 7075-T651	23

21	Fatigue Crack Growth Data Over a Wide Range in Stress Ratios and Rates for 7075-T651	24
22	Indirect Determination of Crack-Opening Loads and Constraint Factor for 7075-T651	25
23	Effective Stress-Intensity Factor Range Against Rates for 7075-T651	26
24	Effective Stress-Intensity Factor Range Thresholds for 7075-T651	27
25	Elastic Stress-Intensity Factors at Failure for 7075-T651 C(T) Specimens	28
26	Measured and Predicted Crack Growth Rates on 7075-T651 at R = 0.9	29
27	Measured and Predicted Crack Growth Rates on 7075-T651 at R = 0.7	30
28	Measured and Predicted Crack Growth Rates on 7075-T651 at R = 0.4	30
29	Measured and Predicted Crack Growth Rates on 7075-T651 at R = 0.1	31
30	Crack Extension Under Compressive Loading for Ti-6Al-4V β-STOA (LS)	32
31	Fatigue Crack Growth During ASTM LR and CPCA Testing for Ti-6Al-4V β-STOA (LS) at R = 0.1	32
32	Fatigue Crack Growth During ASTM LR and CPLR Testing for Ti-6Al-4V β-STOA (LS) at R = 0.4	33
33	Fatigue Crack Growth Data Over a Wide Range in Stress Ratios and Rates for Ti-6Al-4V β-STOA (LS)	34
34	Fatigue Crack Growth During ASTM LR and CPLR Tests for Ti-6Al-4V β-STOA (SL) at R = 0.4	35
35	Fatigue Crack Growth Data Over a Wide Range in Stress Ratios and Rates for Ti-6Al-4V β-STOA (SL)	35
36	Fatigue Crack Growth During ASTM LR and CPLR Tests for Ti-6Al-4V β-STOA (TS) at R = 0.1 and 0.4	36
37	Fatigue Crack Growth Data Over a Wide Range in Stress Ratios and Rates for Ti-6Al-4V β-STOA (TS)	37
38	Crack Growth Rates Affected by Tensile Residual Stresses for Ti-6Al-4V β-STOA (LS)	38

39	Crack Growth Rates Affected by Tensile Residual Stresses for Ti-6Al-4V β-STOA (SL)	38
40	Crack Growth Rates Affected by Tensile Residual Stresses for Ti-6Al-4V β-STOA (TS)	39
41	Comparison of Ti-6Al-4V β-STOA Data at High Stress Ratio	40
42	Comparison of Ti-6Al-4V β-STOA Data at Low Stress Ratio	40
43	Indirect Determination of Crack-Opening Loads and Constraint Factors for Ti-6Al-4V β-STOA	41
44	Effective Stress-Intensity Factor Range Against Rates for Ti-6Al-4V β-STOA (LS)	42
45	Effective Stress-Intensity Factor Range Against Rates for Ti-6Al-4V β-STOA (SL)	42
46	Effective Stress-Intensity Factor Range Against Rates for Ti-6Al-4V β-STOA (TS)	43
47	Crack Growth at V-Notch Affected by Possible Residual Stresses or Recast Zone From Machining Notch	44
48	Ratio of Local and Applied Stress-Intensity Factors Over V-Notch-Affected Region	45
49	Crack Extension Under Compressive Loading for 4340 Steel C(T) Specimens	46
50	Fatigue Crack Growth During ASTM LR and CPLR Tests on 4340 Steel at R = 0.1	47
51	Fatigue Crack Growth During ASTM LR and CPCA Tests on 4340 Steel at R = 0.4	48
52	Fatigue Crack Growth Data on 4340 Steel at R = 0.1	48
53	Fatigue Crack Growth Data on 4340 Steel at R = 0.4	49
54	Fatigue Crack Growth Data on 4340 Steel at R = 0.7	49
55	Fatigue Crack Growth Data Over a Wide Range in Stress Ratios and Rates for 4340 Steel	50
56	Expanded View of Fatigue Crack Growth Rate Data in Near-Threshold Regime	51
57	Effective Stress-Intensity Factor Range Against Rates for 4340 Steel	52
58	Effective Stress-Intensity Factor Range Thresholds for 4340 Steel	53
59	Elastic Stress-Intensity Factors at Failure and Limit-Load Analyses	54

60 Elastic Stress-Intensity Factors at Failure and TPFC Analyses 55

61 Measured and Predicted Crack Growth Rates on 4340 Steel at R = 0.1 56

62 Measured and Predicted Crack Growth Rates on 4340 Steel at R = 0.4 56

63 Measured and Predicted Crack Growth Rates on 4340 Steel at High R 57

64 Crack Growth Data Over a Wide Range in Stress Ratios and K_{max} Test for 7050-T7451 58

65 Crack Growth Data for R = 0.1 Test Conditions for 7050-T7451 58

66 Crack Growth Data for R = 0.1, CPLR, and CPCA Test Conditions for 7050-T7451 (LT) 59

67 Crack Growth Data for R = 0.1 and CPLR Test Conditions for 7050-T7451 60

68 Effective Stress-Intensity Factor Range Against Rates for 7050-T7451 (LT) 61

69 Effective Stress-Intensity Factor Range Thresholds for 7050-T7451 (LT) 62

70 Measured and Predicted Crack Growth Rates on 7050-T7451 for R = 0.1 and 0.7 63

71 Measured and Predicted Crack Growth Rates on 7050-T7451 for R = 0.1 63

72 CPCK Test Results of 12.7-mm-Thick 7050-T7451 (LT) 64

73 CPCK Test Results of 6.35-mm-Thick 7050-T7451 (TL) 65

74 Fatigue Crack Growth Data Over a Wide Range in Stress Ratios and K_{max} Test Conditions for Ti-6Al-4V β-STOA 66

75 Fatigue Crack Growth Data for R = 0.1 Test Conditions for Ti-6Al-4V β-STOA 67

76 Fatigue Crack Growth Data for R = 0.1 and CPCA Test for Ti-6Al-4V β-STOA 67

77 Indirect Determination of Crack-Opening Loads and Constraint Factor for Ti-6Al-4V β-STOA Tested at NASA LaRC 68

78 Effective Stress-Intensity Factor Range Against Rates for Ti-6Al-4V β-STOA 69

79 Effective Stress-Intensity Factor Range Thresholds for Ti-6Al-4V β-STOA 70

80 Measured and Predicted Crack Growth Rates on Ti-6Al-4V β-STOA for a Wide Range in Stress Ratios 71

81 Measured and Predicted Crack Growth Rates on Ti-6Al-4V β-STOA for Near-Threshold Regime for R = 0.1 71

82 Fatigue Crack Growth Data for R = 0.1 and 0.7 for Mg AZ91E 72

83 Effective Stress-Intensity Factor Range Against Rates for Mg AZ91E 73

84 Measured and Predicted Crack Growth Rates on Mg AZ91E for Low and High Stress Ratios 74

85 Fatigue Crack Growth Data for R = 0.1 and CPCA Test Conditions for Mg AZ91E 75

LIST OF TABLES

Table		Page
1	Materials and Compact Specimen Configurations Tested	5
2	Chemical Composition of 7050-T7451 Aluminum Alloy	6
3	Chemical Composition of 7075-T651 Aluminum Alloy	6
4	Chemical Composition of Ti-6Al-4V β-STOA Titanium Alloy	7
5	Chemical Composition of AZ91E Magnesium Alloy	8
6	Chemical Composition of 4340 Steel	9
7	Effective Stress-Intensity Factor Range Against Rate Relation for 7075-T651 (B = 5.7 mm)	29
8	Effective Stress-Intensity Factor Range Against Rate Relation for 4340 Steel (B = 6.35 mm)	52
9	Effective Stress-Intensity Factor Range Against Rate Relation for 7050-T7451 (B = 6.35 mm)	61
10	Effective Stress-Intensity Factor Range Against Rate Relation for Ti-6Al-4V β-STOA (B = 12.7 mm)	69
11	Effective Stress-Intensity Factor Range Against Rate Relation for Mg AZ91E (B = 6.35 mm)	73
12	Materials Tested With Three Threshold Test Methods (ASTM LR, CPCA, and CPLR)	75

LIST OF SYMBOLS AND ACRONYMS

α	Constraint factor
Δc	Crack growth increment, mm
ΔK	Stress-intensity factor range, MPa√m
ΔK_o	Effective stress-intensity factor range threshold, MPa√m
ΔK_{th}	Stress-intensity factor range threshold, MPa√m
ΔK_{eff}	Effective stress-intensity factor range, MPa√m
$(\Delta K_{eff})_T$	Effective stress-intensity factor range at flat-to-slant crack growth, MPa√m
σ_o	Flow stress (average of σ_{ys} and σ_u), MPa
σ_{ys}	Yield stress (0.2 % offset), MPa
σ_u	Ultimate tensile strength, MPa
B	Specimen thickness, mm
C_i	Crack growth equation coefficients
c	Crack length, mm
c_i	Initial crack length, mm
c_n	Notch length, mm
c/W	Crack length to width
dc/dN	Fatigue crack growth rate, m/cycle
E	Modulus of elasticity, MPa
F	Boundary correction on stress-intensity factor
H_N	Notch height
K	Stress-intensity factor
K_{eff}	Effective stress-intensity factor
K_{Ie}	Elastic stress-intensity factor at failure, MPa√m
K_{max}	Maximum applied stress-intensity factor, MPa√m
K_{min}	Minimum applied stress-intensity factor, MPa√m
K_N	V-notch stress-intensity factor, MPa√m
N	Number of cycles
P	Applied load, kN
P_{max}	Maximum applied load, kN
P_{min}	Minimum applied load, kN
P_o	Crack-opening load, kN
R	Stress ratio (K_{min}/K_{max} or P_{min}/P_{max})
R_c	Hardness
S_o	Crack-opening stress, MPa
u	Crack-opening load ratio
ν	Poisson's ratio
W	Width of specimen, mm
BFS	Back-face strain
CA	Constant-amplitude
CMOD	Crack mouth opening displacement
CP	Compression precracking
CPCA	Compression-compression precracking constant-amplitude
CPCK	Compression precracking constant-ΔK

CPLR	Compression-compression precracking load-reduction
C(T)	Compact tension
CTOD	Crack tip opening displacement
EDM	Electron discharge machining
FAA	Federal Aviation Administration
L	Longitudinal
LaRC	Langley Research Center
LI	ΔK increasing
LR	Load reduction
LS	Longitudinal-short
LT	Longitudinal-transverse
MSU	Mississippi State University
M(T)	Middle-crack tension
NASA	National Aeronautics and Space Administration
S	Short
SL	Short-longitudinal
STOA	Solution-treated and over-aged
TPFC	Two-Parameter Fracture Criterion
TS	Transverse-short

EXECUTIVE SUMMARY

Accurate representation of fatigue crack thresholds, the region defining crack growth as either very slow or nonexistent, is extremely important for many rotorcraft applications. If the measured threshold is unconservatively high, then a structural component designed with these data may fail long before fatigue analyses predict. Currently, in North America, the threshold crack growth regime is experimentally defined by using ASTM Standard E 647, which has been shown to exhibit anomalies due to the load-reduction (LR) test procedure. The LR test procedure has been shown to induce remote crack surface closure, which prematurely slows down crack growth and produces an abnormally high threshold for some materials.

The scope of this research was to (1) further develop the compression precracking (CP) threshold test methods, (2) determine fatigue crack growth rates in the near-threshold regime and over a wide range in rates (from threshold to near fracture) for three materials (7075-T651, Ti-6Al-4V β-STOA, and 4340 steel), and (3) analyze the fatigue crack growth data from three rotorcraft materials (7050-T7451, Ti-6Al-4V β-STOA, and Mg AZ91E) tested at the National Aeronautics and Space Administration (NASA) Langley Research Center (LaRC). In addition, a few tests on the 7050-T7451 alloy were conducted at Mississippi State University (MSU) using the new threshold test methods. At MSU, three types of threshold tests were conducted on each material: (1) ASTM E 647 LR procedure, (2) compression-precracking constant-amplitude (CPCA) test method, and (3) compression-precracking load-reduction (CPLR) test method. An additional test method, compression precracking constant-ΔK (CPCK), was also used on one material tested at NASA LaRC and another material tested at MSU. All tests were conducted in a laboratory air environment at room temperature. Test results were used to develop alternative test methods to determine thresholds and near-threshold fatigue crack growth rate behavior for metallic materials. The titanium (β-STOA) alloy showed large differences between the ASTM LR and CPCA/CPLR tests, but the 7075-T651 and 4340 steel showed small differences. But even for the latter two materials, the CPCA/CPLR methods produced slightly lower thresholds than the ASTM LR method.

Of the nine materials tested under Federal Aviation Administration (FAA)- and Office of Naval Research-sponsored research using the three threshold test methods, two of the materials (7075-T651 and 4340 steel) showed very little difference, while five materials (7050-T7451, 7075-T7351, Ti-6Al-4V STOA, Ti-6Al-4V β-STOA, and Inconel-718) showed large differences, with the CPCA and CPLR test methods producing lower thresholds and faster rates in the near-threshold regime. One of the aluminum alloys, 2324-T39, produced slightly lower thresholds using the CPCA method than the LR method; and for the magnesium alloy (AZ91E), not enough CP tests were conducted to make an assessment. The materials that showed very little difference had crack surfaces that were very flat and straight, while the materials that showed a significant difference exhibited either very rough crack surface profiles or produced fretting debris along the crack surfaces. Thus, it is suspected that load-history effects due to residual plastic deformations in combination with roughness- and fretting debris-induced crack closure caused the ASTM LR method to induce inadvertently high thresholds and slower crack growth rates in the midregion approaching threshold conditions due to premature crack surface contact. Whereas, the CP methods produce a tensile residual-stress field that causes initially high (invalid) rates. However, the crack must be grown under constant-amplitude (CA) loading, at least two compressive

plastic-zone sizes from the crack starter notch, to approach steady-state conditions. At this point, CA loading could either be continued or an LR test could be conducted.

For some materials, like 4340 steel, a crack could not be initiated at the standard crack starter notch at the ΔK level corresponding to the maximum-allowed rate (1E-8 m/cycle) in the ASTM LR standard, and higher ΔK levels were required. However, CP tests allowed cracks to be initiated at ΔK levels close to ΔK_{th} values, and thus, load-history effects would be minimized.

For both the Inconel-718 and Ti-6Al-4V STOA titanium alloy, a width effect on thresholds was observed using the ASTM LR method, where larger-width specimens produced higher thresholds and slower fatigue crack growth rates in the near-threshold regime. But threshold and near-threshold results using the CPCA test method were found to be independent of width.

In another project sponsored by the FAA with NASA LaRC, four rotorcraft materials (7050, 4340 steel, magnesium AZ91E, and Ti-6Al-4V β-STOA) were tested with the ASTM LR test method. But the CPCA results were presented on only one of the materials (7050), and only a few tests at stress ratio R = 0.1 were conducted. They found differences, but attributed this to tensile residual stresses from CP. From these results, it was concluded that the ASTM LR method showed little or no apparent load-history effects when ASTM E 647 LR procedures were strictly followed. Because extensive CP tests were not conducted on the 7050 alloy, a proper assessment between the ASTM LR and CPCA/CPLR methods could not be made. But on a similar β-STOA titanium alloy, tested at MSU, significant differences were observed between the methods. However, due to the large-grain microstructure and possible forging residual stresses, the large scatter observed in this material are of concern. But the CP methods consistently produced lower thresholds and faster crack growth rates in the near-threshold regime. Also, the 4340 steels tested at NASA LaRC and MSU showed drastic differences in behavior in the threshold and near-threshold regimes, even using the same test method.

It is suspected that the maximum-allowed rate in the ASTM LR standard (10^{-8} m/cycle) is too high for some materials and produces elevated thresholds and slower crack growth rates. But in the CPLR method, the CP allows the initial ΔK levels to be nearly a factor of 2 lower and at a corresponding rate nearly an order of magnitude (10^{-9} m/cycle) lower than the ASTM standard LR method. Therefore, much less residual plastic deformations are left along the crack surfaces than in the current LR method (if started at the maximum-allowed rate).

From a mechanic standpoint, when using the ASTM LR method, it is difficult to discount load-history effects because as the ΔK level is reduced, crack surface displacements also become progressively smaller, until the crack surfaces contact plasticity, roughness, and fretting debris mechanisms. Elimination of any of these mechanisms would delay crack surface contact and cause higher crack growth rates. On the other hand, the CP methods induce tensile residual stresses at the crack starter notch and develop fully open cracks before CA loading is applied. Here, the crack surface displacements increase as the crack grows, making it more difficult for the crack surfaces to contact. However, the crack must be grown at least two compressive plastic-zone sizes to eliminate notch effects, tensile residual-stress effects, and stabilization of the crack closure mechanisms.

1. INTRODUCTION.

Fatigue crack growth in a metallic material is typically quantified by the length of the crack, c, and the rate at which the crack propagates (dc/dN). The crack growth rate in a given material is defined in terms of the linear elastic fracture mechanics parameter, ΔK, the stress-intensity factor range at a given stress ratio (R = minimum to maximum load ratio). The relationship between ΔK and dc/dN was originally shown to be nearly linear on a log(ΔK)-log(dc/dN) scale by Paris and Erdogan [1] for a large number of materials. However, the relation between ΔK and dc/dN is nonlinear when the cracked body is approaching fracture [2], and when the crack growth rate is very slow [3]. Therefore, the three regions of crack growth are defined as the threshold region (slow growth), the linear midregion (Paris regime), and the fracture region (rapid growth).

Accurate representation of fatigue crack growth thresholds is extremely important for many structural applications. Presently, in the United States, the threshold regime is experimentally defined by using a load-reduction (LR) test procedure [4]. In the early 1970s, an LR test method was developed by Paris, et al. [5 and 6], to generate data at low values of stress-intensity factor ranges and approaching threshold conditions. Later, Hudak, et al. [7], and Bucci, et al. [8], finalized the method, which was incorporated into ASTM E 647 fatigue crack growth rate test standard. During the same time, Ohta, et al. [9], and Minakawa and McEvily [10] showed a rise in the crack closure levels as the threshold conditions were approached using similar LR methods. This behavior was attributed to roughness- and fretting debris-induced crack closure effects. Later, Newman [11 and 12] and McClung [13] showed a rise in the crack closure level using the LR method on strip yield and finite element models, respectively. These models showed that the LR test method exhibited anomalies due to load-history effects from residual plastic deformations. The current ASTM LR test method may also produce data, which exhibits "fanning" in the threshold regime with stress ratio. (Fanning is larger spread in the threshold regime than in the midregion for fatigue crack growth rate data with stress ratio, R.) It is suspected that the LR test method induces remote closure, which prematurely slows down crack growth and produces abnormally high thresholds for low stress ratio conditions. Fanning could also be caused by environment, which naturally produces oxide and/or fretting debris and higher closure levels [14 and 15]. It has also been suspected that crack surface roughness is more prevalent in the threshold regime, which could also cause higher closure levels at low stress ratio conditions [15 and 16].

Alternative test methods have also been proposed, such as the constant K_{max} test procedure [17], to define the low crack growth rate and threshold regimes. But the current K_{max} test procedure produces data at variable stress ratios (R) and fatigue crack growth thresholds at extremely high stress ratios (>0.9). The K_{max} test procedure also produces what has been referred to as the K_{max} effect, in that, lower thresholds are obtained using higher K_{max} values [18 and 19]. But extensive literature data reviewed by Vasudevan, et al. [20], on a wide variety of materials do not show the K_{max} effect. These mixed results suggest that something is different in either the test procedure or test specimens that exhibit different behavior in the near-threshold regime. Recently, Yamada and Newman [21 and 22], using local measurement techniques, have measured crack closure under high-R and K_{max} test conditions. Thus, the K_{max} effects are more likely due to crack closure effects.

To generate fatigue crack growth rate data in the threshold and near-threshold regimes, without appreciable load-history effects, a "compression-compression" precracking method, developed by Hubbard [23], Topper and Au [24], Pippan, et al. [25 and 26], Forth, et al. [27 and 28], Newman, et al. [29], and Ruschau and Newman [30 and 31], was used. Using these new threshold test methods, environmental effects, such as oxide and/or fretting debris-induced closure, crack surface roughness-induced closure, and plasticity-induced closure would naturally develop under constant-amplitude (CA) loading conditions.

1.1 PURPOSE.

The purpose of this study was to further develop the compression precracking (CP) threshold testing methods, to conduct fatigue crack growth tests on three materials (aluminum alloy, titanium alloy, and steel) from threshold to near fracture, and to analyze the fatigue crack growth rate data generated at the National Aeronautics and Space Administration (NASA) Langley Research Center (LaRC) on three additional rotorcraft materials [32].

1.2 BACKGROUND.

A schematic of the expected behavior for LR and compression precracking constant-amplitude (CPCA) loading is shown in figure 1. The objective was to determine steady-state CA results (solid curve) at a constant stress ratio (R), without any load-history effects. The traditional LR scheme was shown to induce higher thresholds than steady-state conditions [27-31]. Also, the thresholds were shown to be influenced by the initial ΔK level at which the LR procedure was applied [33]. An LR test normally starts at an initial ΔK_i level, such as ΔK_2, and the maximum and minimum loads are reduced as the crack grows to slowly reduce ΔK and to maintain constant R. If a lower ΔK value is used, such as ΔK_1, a lower threshold may be generated. After the threshold is reached, an increasing load test is generally conducted to obtain the upper region of the ΔK-rate curve. This is referred to as a "load-reduction and load-increasing" test.

On the other hand, a crack grown under the CPCA loading is fully open at the start of CA loading (constant ΔP_i at a given R) after CP. During CA loading, the crack may slow rapidly and approach the steady-state curve. The crack, which is initially fully open, grows because of the tensile residual stresses induced by compressive yielding at the crack starter notch, and the CA load range is fully effective (no crack closure). Currently, trial-and-error procedures are required to select the initial tensile loading ΔP_i (constant R) to start the test at the unknown threshold value. If a tensile load range that would produce a stress-intensity factor range below the threshold is selected, such as ΔP_1, then the crack may initially grow but become a nonpropagating crack. However, if the load is high enough, the crack will grow. At higher load amplitudes, such as ΔP_3, the crack will continue to grow. It is estimated that the crack must be grown several compressive plastic-zone sizes before the effects of the tensile residual stresses (due to compressive yielding at the notch) have decayed and the crack-opening stresses have stabilized under steady-state conditions. The effective stress-intensity factor (ΔK_{eff}) curve (dash-dot curve) is the ΔK-rate curve for high stress ratios and is characteristic behavior of a fully open crack. The ΔK_{eff} curve may or may not be parallel the steady-state curve due to a three-dimensional constraint and environmental effects. Thus, the LR test may be referred to as an

upper-bound method, and the CPCA test may be referred to as a lower-bound method for determination of thresholds and near-threshold behavior.

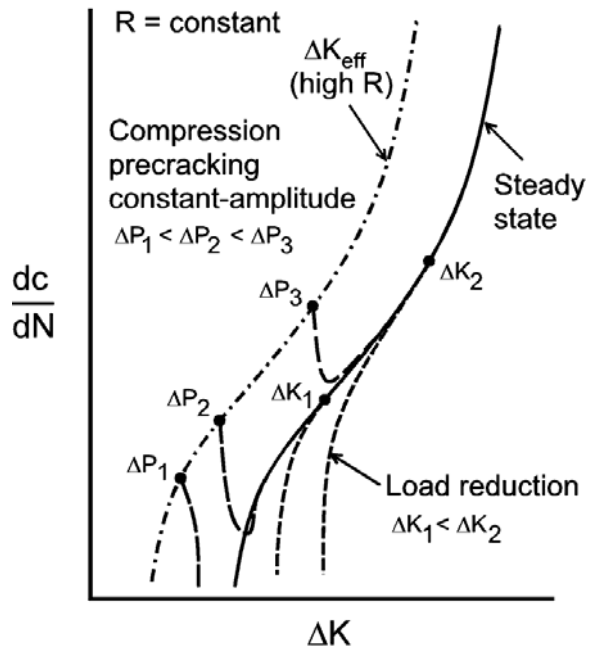

Figure 1. Typical Fatigue Crack Growth Data Under CA, LR, and CPCA Loading

1.3 RESEARCH OBJECTIVES.

The scope of the proposed research is to (1) further develop the CP threshold test methods, (2) determine the fatigue crack growth rates in the near-threshold regime and over a wide range of rates (from threshold to near fracture) for three materials (7075-T651, Ti-6Al-4V β-STOA, and 4340 steel), and (3) analyze the fatigue crack growth data from three rotorcraft materials (7050-T7451, Ti-6Al-4V β-STOA, and Mg AZ91E) tested at the NASA LaRC [32]. In addition, some tests on the 7050-T7451 alloy were conducted at Mississippi State University (MSU) using the new threshold test methods. In general, three types of tests were conducted on each material at MSU. They were: (1) the ASTM E 647 LR procedure, (2) the compression-compression precracking, constant-amplitude (CPCA) test method, and (3) the compression-compression precracking load-reduction (CPLR) test method. An additional test method, compression precracking constant-ΔK (CPCK) was also used on one material tested at NASA LaRC. All tests were conducted under a laboratory air environment. These test results were used to develop alternative test methods to determine threshold and near-threshold fatigue crack growth rate behavior for metallic materials.

2. LABORATORY TEST SPECIMENS.

Test specimens used at both MSU and the NASA LaRC were standard plan-form compact tension C(T) specimens (see figure 2); however, the MSU tests had beveled pinholes to help minimize out-of-plane bending influence on crack-front shapes in threshold tests.

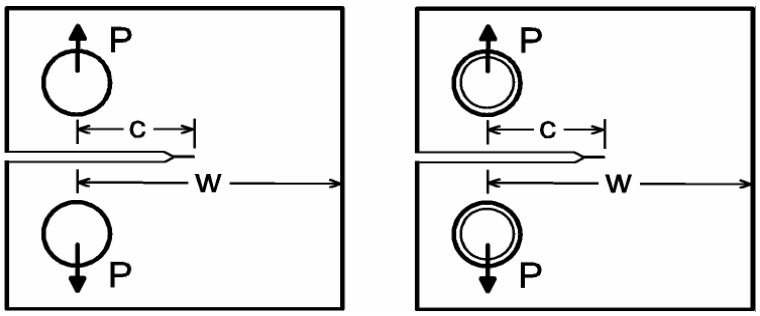

(a) Standard pinholes (b) Beveled pinholes

Figure 2. Standard and Modified Compact Specimen Configurations

Because of slight misalignments in compact-clevis pin-loading fixtures, the pin may contact the outer edges of the pinholes and cause out-of-plane bending on the specimen. Thus, stress-intensity factors at the crack tip on one side of the specimen will be higher than on the other and cause a nonstraight crack front. The beveled pinhole (shown in figure 3) causes the pin to automatically contact near the centerline of the specimen. This reduces the out-of-plane bending and produces a straighter crack front, as shown in figure 4 on 4340 steel C(T) specimens.

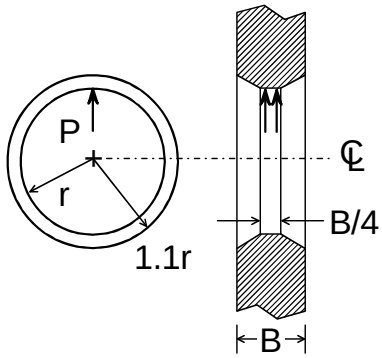

Figure 3. Beveled Pinhole Configuration in Compact Specimens

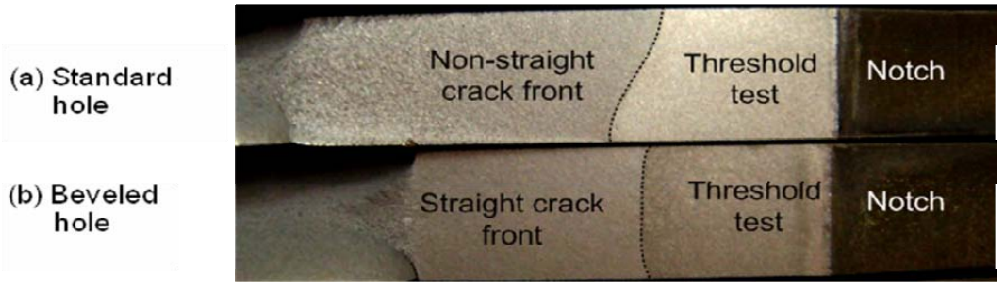

Figure 4. Crack Front Shape Near Threshold in 4340 Steel Compact Specimens

One specimen had the standard pinhole configuration and produced a nonstraight crack front as the threshold condition was approached; whereas, the specimen with beveled pinholes produced a nearly straight crack front during a similar threshold test.

The C(T) specimens tested at MSU and NASA LaRC were either nominally 51 or 76 mm wide (W). The crack starter V-notch had either a 45- or 60-degree angle included. In the MSU tests, the notch length-to-width (c_n/W) ratio varied from 0.33 to 0.35 to increase the sensitivity of the back-face strain (BFS) gage crack monitoring system.

A summary of the materials and C(T) specimen configurations tested at MSU and NASA LaRC are listed in table 1.

Table 1. Materials and Compact Specimen Configurations Tested

Material	Alloy and Temper	B (mm)	W (mm)	Laboratory
Aluminum alloy	7050-T7451	6.35, 12.7	51	NASA LaRC and MSU
Aluminum alloy	7075-T651	5.7	76	MSU
Titanium alloy	Ti-6Al-4V β-STOA	9.5	76	MSU
Titanium alloy	Ti-6Al-4V β-STOA	12.7	76	NASA LaRC
Magnesium alloy	AZ91E	6.35	51	NASA LaRC
Steel	4340	6.35	51	MSU

B = Specimen thickness

3. MATERIALS.

A number of materials used in the rotorcraft industry were used to generate fatigue crack growth rate data over a wide range of stress ratios ($R = P_{min}/P_{max}$) from threshold to near fracture. Most materials were obtained from Sikorsky Aircraft Corporation or Boeing Rotorcraft Systems, but the 7075-T651 alloy was obtained from Northrop Grumman Corporation. These materials were selected to cover the broad range of materials and to study the threshold and near-threshold behavior using the current ASTM LR test procedure and the newly developed CP methods. For the materials tested at NASA LaRC, the CP methods were not used as widely as they should have been. Thus, limited results are presented for these materials.

3.1 ALUMINUM ALLOY 7050-T7451.

NASA LaRC machined all of the 7050 specimens from a 152-mm-thick plate that had been obtained in an over-aged T7451 heat-treat condition per specification AMS 4050G. The chemical composition of this alloy [34] is listed in table 2. Some specimens were also provided to MSU.

Tensile tests were conducted according to ASTM Standard E8 using 6.4-mm-round-bar tension specimens. The specimens were tested in the both the longitudinal (L) and short (S) orientations at room temperature. The yield stress, ultimate tensile strength, and modulus of elasticity were calculated from two tests for each orientation. For the L orientation at room temperature, the yield stress was 470 MPa, the ultimate tensile strength was 525 MPa, and the modulus of elasticity was 76 GPa.

Table 2. Chemical Composition of 7050-T7451 Aluminum Alloy

Element	Symbol	Percentage
Aluminum	Al	Balance
Chromium	Cr	0.04
Copper	Cu	2.0-2.6
Iron	Fe	0.15
Magnesium	Mg	1.9-2.6
Manganese	Mn	0.1
Silicon	Si	0.12
Titanium	Ti	0.06
Zinc	Zn	5.7-6.7
Zirconium	Zr	0.08-0.15
Others		0.2

3.2 ALUMINUM ALLOY 7075-T651.

The 7075-T651 aluminum alloy material was obtained from Northrop Grumman that was machined from a 50-mm-thick plate to simulate the location of the outer-wing plank material. All specimens were tested in the longitudinal transverse (LT) orientation (crack plane perpendicular to the rolling direction). The chemical composition of this alloy [34] is listed in table 3.

Table 3. Chemical Composition of 7075-T651 Aluminum Alloy

Element	Symbol	Percentage
Aluminum	Al	Balance
Chromium	Cr	0.18-0.28
Copper	Cu	1.2-2.0
Iron	Fe	<0.5
Magnesium	Mg	2.1-2.9
Manganese	Mn	<0.3
Silicon	Si	<0.4
Titanium	Ti	<0.2
Zinc	Zn	5.1-6.1
Others		0.15

The tensile properties were obtained from several ASTM Standard E8 specimens [35]. The average yield stress (0.2% offset) was 520 MPa, the ultimate tensile strength was 575 MPa, and the modulus of elasticity was 71.7 GPa.

3.3 TITANIUM ALLOY Ti-6Al-4V β-STOA.

The titanium alloy specimens were machined from two forging blocks that were obtained from Sikorsky Aircraft Corporation. The titanium alloy (Ti-6Al-4V) was provided in the β-STOA (solution-treated and over-aged) condition. This alloy has a very course microstructure with nearly equiaxed grains approximately 1 mm in diameter. Figure 5 shows the layout of specimens for the three orientations: longitudinal-short (LS), short-longitudinal (SL), and transverse-short (TS). Ten specimens were machined in each orientation. The chemical composition of this alloy [34] is listed in table 4.

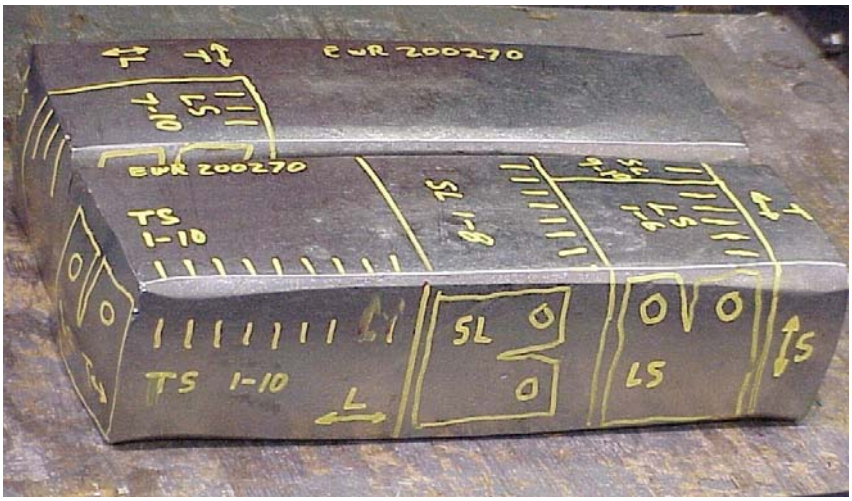

Figure 5. Compact Specimen Layout in Titanium Alloy Forging

Table 4. Chemical Composition of Ti-6Al-4V β-STOA Titanium Alloy

Element	Symbol	Percentage
Aluminum	Al	5.5-6.75
Carbon	C	0.08
Hydrogen	H_2	0.0125
Iron	Fe	0.3
Nitrogen	N_2	0.05
Oxygen	O_2	0.2
Titanium	Ti	Balance
Vanadium	V	3.5-4.5
Yttrium	Yt	0.005

The tensile properties were obtained from several ASTM Standard E8 specimens. The average yield stress (0.2% offset) was 930 MPa, the ultimate tensile strength was 1030 MPa, and the modulus of elasticity was 120 GPa [36].

3.4 MAGNESIUM ALLOY AZ91E.

The Mg AZ91E fatigue crack growth rate data from C(T) specimens were provided to MSU by NASA LaRC [37]. The magnesium alloy was provided to NASA LaRC in cast plates approximately 350 mm square and 12.7 mm thick. C(T) specimens (W = 50.8 mm and B = 6.35 mm) were machined from these plates with the specimen sides at least 10 mm from the plate edges to avoid any microstructural gradient that might have been created during processing. Additionally, the outer surfaces of the plate were milled down approximately 3 mm (creating a 6.35-mm-thick specimen from a 12.7-mm-thick plate) to avoid any microstructural gradient that may exist near the plate surface.

Unfortunately, the temper was not reported and no tensile tests were conducted to provide the yield stress and ultimate tensile strength. According to ASM International property tables [38], the T4 and T6 tempers have yield stresses that range from 90 to 145 MPa, respectively, and an ultimate tensile strength of 275 MPa. The modulus of elasticity is about 45 GPa. The nominal chemical composition of the AZ91E magnesium alloy is given in table 5.

Table 5. Chemical Composition of AZ91E Magnesium Alloy

Element	Symbol	Percentage
Aluminum	Al	8.1-9.3
Copper	Cu	0.015
Iron	Fe	0.005
Magnesium	Mg	Balance
Manganese	Mn	0.17-0.35
Nickle	Ni	0.001
Silicon	Si	0.2
Zinc	Zn	0.35-1.0
Others		0.3

3.5 STEEL 4340.

The 4340 steel C(T) specimens were provided by Boeing Rotorcraft Systems. The 51-mm-wide specimens were machined from a 150-mm-diameter by 750-mm-long rod in the LT orientation. Thirty specimens were provided to MSU. The chemical composition of this alloy [38] is listed in table 6.

Tensile properties were not obtained on this particular material. The stated minimum tensile strength from Boeing Rotorcraft Systems was from 1050 to 1180 MPa. Thus, efforts were made to determine the hardness of the material to obtain an estimate of the tensile strength, since standard tensile specimens could not be machined from the material provided to MSU. The hardness (R_c) was found to be about 37, which gave an estimated tensile strength of 1145 MPa. The tensile properties (yield stress and ultimate tensile strength) are important in the fracture toughness assessment of the steel.

Table 6. Chemical Composition of 4340 Steel

Element	Symbol	Percentage
Carbon	C	0.38-0.43
Chromium	Cr	0.7-0.9
Iron	Fe	Balance
Manganese	Mn	0.6-0.8
Molybdenum	Mo	0.2-0.3
Nickel	Ni	1.65-2.0
Phosphorous	P	<0.035
Silicon	Si	0.15-0.3
Sulphur	S	<0.04

4. TEST METHODS.

In generating fatigue crack growth rate data (crack length against cycles) on metallic materials, various test methods have been used over the past 35 years (see ASTM E 647 [4]). The primary goal has been to determine the CA fatigue crack growth rate behavior at various mean and alternating load conditions. However, to generate fatigue crack growth rate data in the near-threshold regime, CA loading conditions have not been able to initiate a crack at a crack starter notch at the extremely low stress-intensity factors required. Therefore, Schmidt and Paris [6] and Hudak, et al. [7], developed an LR scheme to initiate cracks at higher stress-intensity factor ranges and slowly reduce the ΔK range until the near-threshold and threshold behavior is obtained. The LR procedure assumed that the crack growth rate was totally controlled by the ΔK value. This procedure was standardized in ASTM E 647 and has been used for over 25 years to generate fatigue crack growth rate data from threshold to fracture conditions. Herman, et al. [17], developed an LR procedure to reduce ΔK (by reducing the load amplitude), but held the K_{max} value constant. This procedure generated low crack growth rates at very small ΔK values, but the stress ratio near and at threshold was extremely high, generally greater than 0.9. Procedures to maintain a constant ΔK value have also been used to study environmental effects. This procedure, which is also an LR procedure to maintain a constant ΔK value as the crack grows, has been widely used. All these methods assume that the crack tip behavior is totally controlled by the stress-intensity factor range.

However, fatigue crack closure under cyclic loading (Elber [39]) causes the load history to have an influence on crack growth rate behavior, such as the plastic wake and residual stresses. Thus, the stress-intensity factor range does not control fatigue crack growth. Contact of the crack surfaces and residual stresses in the plastic zone influences the crack growth rate behavior. Since Elber's discovery, several other closure (or shielding) mechanisms, such as fretting debris- and roughness-induced closures, have been discussed and modeled [40-42]. The test environment, including laboratory air, has a tremendous influence on the crack growth mechanisms that are activated, which can influence the crack closure behavior, and must be considered in developing any damage tolerance life-prediction method.

During the past decade, there has been a renewed interest in using CP test procedures, as proposed by Hubbard [23], Topper and Au [24], Pippan, et al. [25 and 26], Forth, et al. [27 and 28], Newman, et al. [29], and Ruschau and Newman [30 and 31], to generate a crack under compressive loading and then to apply either a small stress-intensity factor range or small CA loading slightly above the steady-state ΔK threshold at a given stress ratio. This test procedure should generate fatigue crack growth rate data in the near-threshold regime that minimizes any load-history effects after the crack has grown several compressive plastic-zone sizes [43 and 44].

In sections 4.1 and 4.2, two fatigue crack growth rate test methods are presented and discussed. They are (1) ASTM LR threshold tests and (2) CP threshold tests.

4.1 ASTM LR THRESHOLD TESTS.

The current LR test method defined by ASTM E 647 is designed to fully reproduce the range of fatigue crack thresholds (e.g., low and high stress ratios) needed to characterize loading conditions for many structural applications. The ASTM LR test procedure [4] was based on stress-intensity factors changing at an exponential rate. A typical LR example is shown in figure 6. The ratio of the current applied load, P_{max}, to the initial applied load, $(P_{max})_i$, is plotted against crack length. The solid curves are based on a constant rate of change in normalized plastic-zone size with crack extension. The normalized K-gradient, (dK/dc)/K, was -0.08 mm^{-1} for the upper solid curve, as recommended in the Standard. This is equivalent to a 5% change in stress every 0.5 mm of crack extension, as shown by the stair-step lines. The Standard also allows a 10% change every 0.5 mm of crack extension; if computerized, smooth LR capability is not available. This is equivalent to a normalized K-gradient of -0.2 mm^{-1}, as shown by the lower solid curve. These procedures have been used over the past 25 years to generate fatigue crack growth thresholds for a wide variety of materials.

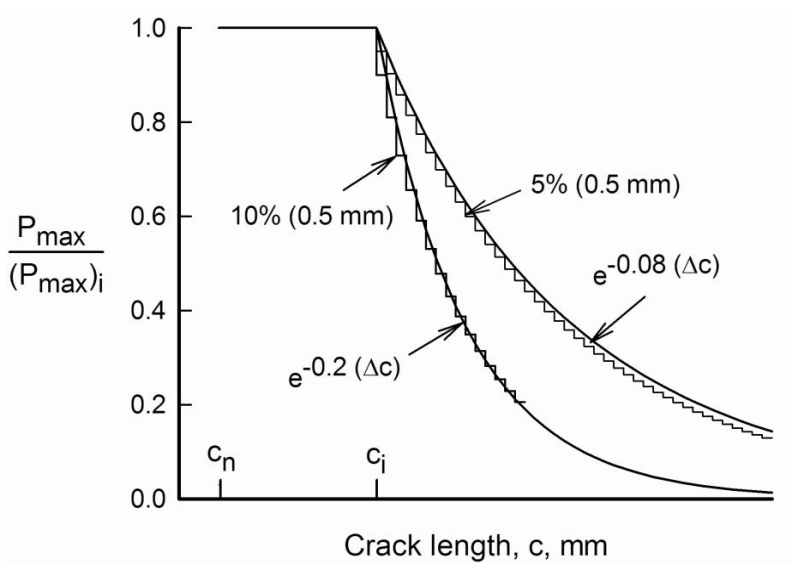

Figure 6. Definition of ASTM E 647 LR Procedure

4.2 THE CP THRESHOLD TESTS.

For CP threshold tests, the test specimen must have a sharp V-notch, so compressive yielding at the notch-root tip will induce tensile residual stresses to grow the crack under compression-compression loading. To establish the validity criteria for crack growth from the notch, several issues must be resolved. First, the stress-intensity factors for a crack under compressive loading (without surface contact) must be determined. Second, the effects of the crack starter V-notch on stress-intensity factors must be calculated. Third, the minimum compressive loading needed to initiate a crack at the V-notch must be established. Finally, the amount of crack growth from the notch tip needs to have no (or minimal) influence of the tensile residual stresses on crack growth and the amount of crack growth for crack closure behavior to stabilize under CA loading.

For CP threshold tests, there are three loading options, after CP: (1) constant stress-intensity factor range tests, (2) CA load tests, and (3) standard LR reduction tests.

4.2.1 Stress-Intensity Factors Under Compressive Loading.

Figure 7 shows how the C(T) specimens were tested under compression-compression loading to initiate a small fatigue crack (0.3 to 0.6 mm in length) at the crack starter V-notch. Two methods were used. In the first method, the standard pins were used to apply compressive loads (figure 7(a)). Here, the pins must contact the holes before the loading clevis' contact. Using this method, the pinholes are known to crack when high compressive loads are used and are applied for a large number of cycles. To help prevent pinhole cracks, the lower portion of the pinhole surfaces were polished, low compressive loads were used, and a small number of cycles were applied (less than 100,000). The beveled holes may also induce pinhole cracks due to the higher bearing stresses. In the second and most common method, small aluminum blocks were bonded to the top and bottom of the specimen edges along the load line, so the blocks would contact before the loading clevis (figure 7(b)). The standard pins were removed and smaller diameter pins were installed as safety pins to prevent the specimen from coming out of the fixture during compressive loading. Typically, less than about 60,000 cycles are required to initiate a crack at the V-notch for a wide variety of materials under the specified compressive loading. The crack would grow and naturally develop into a nonpropagating crack as the crack closure levels approached the threshold conditions under cyclic compression.

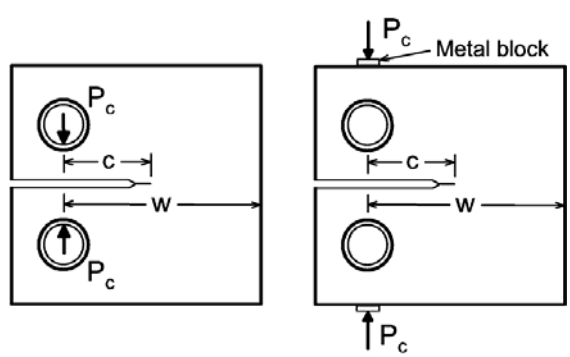

(a) Pinhole loading (b) Edge loading

Figure 7. Compressive Loading Options on C(T) Specimens

A boundary element code, FADD2D [44], was used to calculate the stress-intensity factor (K) for cracks under compressive loading (figure 7). Crack surface contact was not modeled, and the stress-intensity factors were negative. Normalized stress-intensity factors are shown in figure 8 as a function of the crack length to width (c/W) ratio. K_{CT} is the stress-intensity factor solution for the standard C(T) specimen [4]. The compressive pin loading gave higher absolute stress-intensity factors than standard pin loading (figure 2) for c/W <0.5. Whereas, the C(T) configuration with compressive loading applied at the top and bottom edges of the specimen gave essentially the same absolute stress-intensity factor solution as the standard specimen (0.5% for $0.2 \leq c/W \leq 0.7$).

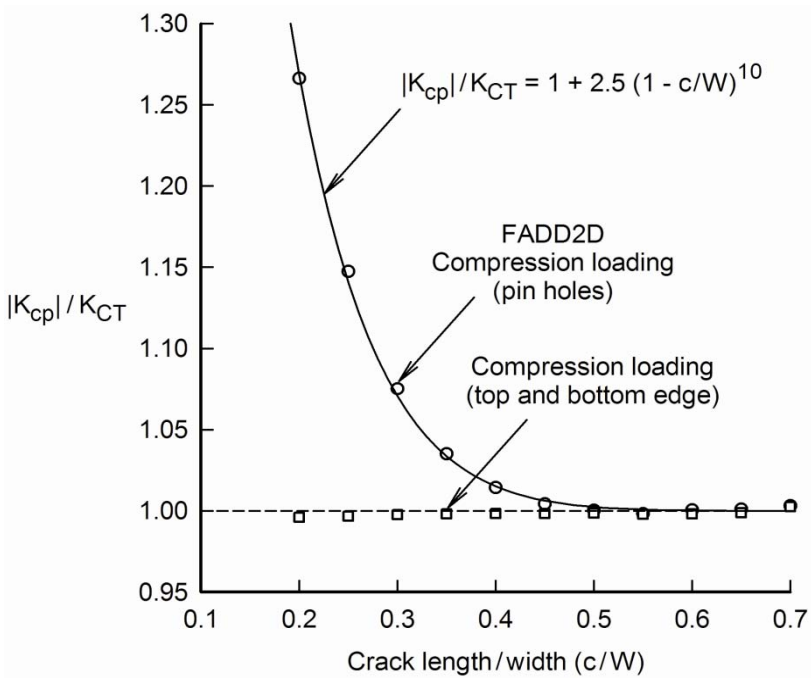

Figure 8. Normalized Stress-Intensity Factors for C(T) Specimen Under Compressive Loading at Pinholes or Edges

4.2.2 V-Notch Effects on Stress-Intensity Factors.

Figure 9 shows the results of the boundary element analyses of standard C(T) and middle-crack tension M(T) specimens with a small crack emanating from a crack starter V-notch with a notch-root radius of 0.2 mm. Boundary element analyses were conducted with the FADD 2D code [45]; and additional results were provided by Mark James (NASA LaRC, unpublished) using the FRANC2DL finite element code [46]. Crack extension from the V-notch is denoted as Δc. The stress-intensity factor for a crack emanating from the V-notch, K_N, is normalized by the standard K solution for the C(T) specimen [4] or the M(T) specimen [47]. Calculations had been made for either a 45- or 60-degree notch for a 76-mm-wide specimen with a notch length-to-width (c_n/W) ratio of 0.25. (Note that W is the width of the C(T) specimen, and 2W is the total width of the M(T) specimen.) The notch height, H_n, was 2.54 mm ($W/H_n = 30$). For crack lengths greater than or equal to 0.5 H_n from the V-notch tip, the stress-intensity factors were within about 1 percent of the standard K solutions for C(T) and M(T) specimens. Stress-intensity factors approach the standard K solution for crack lengths greater than 0.5 H_n. Although these results

are for c/W = 0.25, it is expected that the ratios of K_N/K_{CT} or K_N/K_{MT} would have similar behavior for larger c/W ratios. However, the intent is to not account for the effects of the notch on stress-intensity factors, but to grow the crack beyond the influence of the notch.

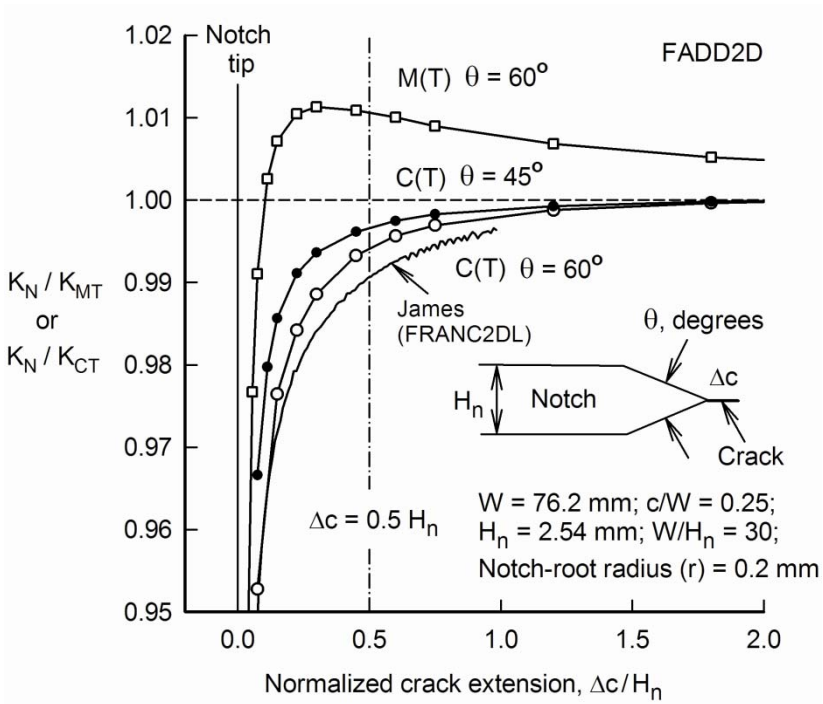

Figure 9. Normalized Stress-Intensity Factors for Crack Emanating From V-Notch in Standard C(T) and M(T) Specimens

4.2.3 Crack Growth Under Compressive Loading.

The measured crack extension, Δc, during cyclic compression on a variety of materials is shown in figure 10 as a function of the normalized compressive stress-intensity factor, $|K_{cp}|/E$. Because the tensile residual-stress zone is proportional to the compressive plastic-zone size, the intent was to find the smallest compressive loading that would initiate a fatigue crack at the V-notch tip with a reasonable root radius in a variety of materials. Thus, the affected zone of residual stresses and the amount of crack extension required for valid crack growth rate data (unaffected by residual stresses) would be minimized. The maximum compressive stress-intensity factor (K_{cp}) level that was found to produce reasonably sized fatigue cracks was estimated from the following relationship:

$$|K_{cp}| / E = 0.00032 \sqrt{m} \tag{1}$$

where E is the material elastic modulus (see dashed vertical line in figure 10).

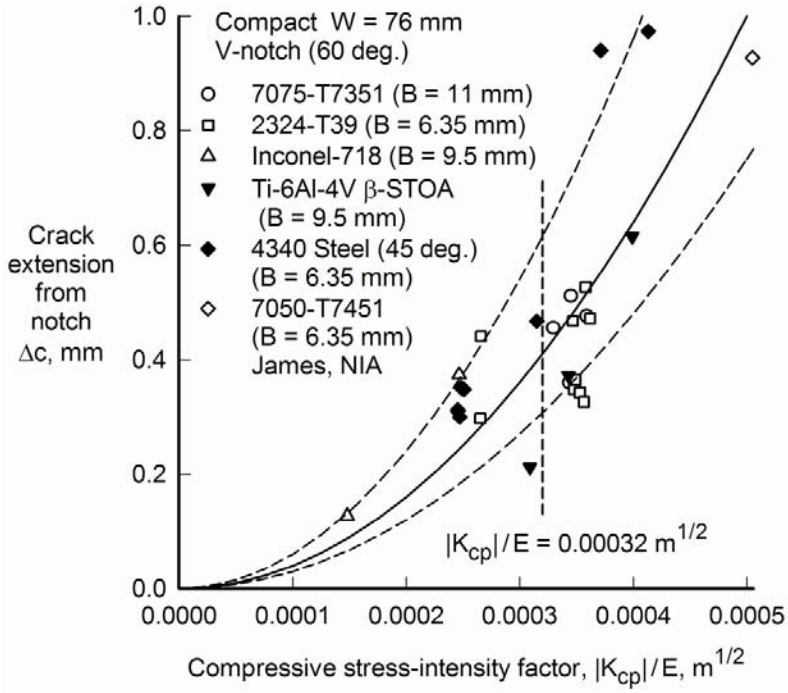

Figure 10. Crack Extension Under Compressive Loading for a Variety of Materials

4.2.4 Residual Stresses and Stabilization of Crack-Opening Stresses.

One of the major concerns with compressive precracking is the influence of the tensile residual stresses caused by compressive yielding on fatigue crack growth rate behavior. Thus, two-dimensional, elastic-plastic, finite element crack growth simulations under plane-stress conditions were conducted on C(T) specimens made of an aluminum alloy to study the (1) decay of tensile residual stresses, (2) stabilization of crack-opening loads, and (3) merging of cyclic crack tip opening displacements (CTOD) under CA and CPCA loading [44].

The finite element code used was ZIP2D [48], which was one of the first codes to simulate fatigue crack growth and crack closure effects. The finite element C(T) model had a width W = 76 mm, a notch height H_n = W/32, a notch length c_n = 0.25W, and a 45-degree V-notch with a notch-root radius of 0.127 mm. (Plate thickness was 7.6 mm.) The finite element mesh had about 30,000 nodes and 60,000 elements (~60k degrees of freedom), and the minimum element size along the crack path was 2 μm. Typical high-strength aluminum alloy properties, such as those for 7075-T6, were used (modulus of elasticity E = 70 GPa, Poisson's ratio ν = 0.3, and flow stress σ_o = 520 MPa). The material had an elastic-perfectly-plastic stress-strain behavior and neither kinematic nor isotropic hardening was modeled. Moreover, the purpose of this study was to conduct an elastic-plastic treatment of simulated fatigue crack growth after compressive yielding, rather than to use linear superposition, which is typically used to account for residual-stress fields.

In practice, it is common to consider that residual-stress distributions are maintained during fatigue crack growth and that they do not decay. Hence, linear superposition is traditionally used to account for the influence of residual stresses on fatigue crack growth. However, during these

crack growth simulations, the residual-stress field decayed as the crack grew. The tensile residual stresses created during CP were completely removed when the crack had reached about 1 plastic-zone size. Thus, crack extension values beyond one plastic-zone size should not be affected by the tensile residual stresses. This is in contrast to the linear-superposition method [43], which showed that the influence of the tensile residual stresses was about 2 compressive plastic-zone sizes.

Some typical calculations of crack-opening load stabilization and merging of the CTOD values from CA and CPCA loading are shown in figures 11 and 12, respectively. In figure 11, the curves are the calculated results under CA (R = 0) loading and the symbols show the behavior under CPCA loading. Crack-opening loads under CPCA loading merged with those from CA loading at about 1.2 plastic-zone sizes for low and high (ΔP/B) loading on the C(T) model.

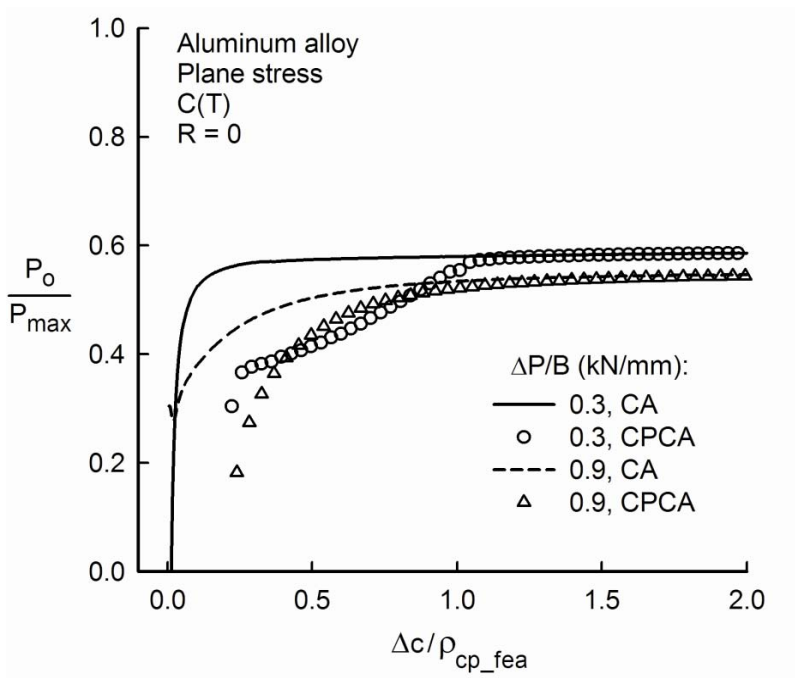

Figure 11. Comparison of Crack-Opening Loads for CA and CPCA Loading

Figure 12 shows the merging of the calculated CTOD values, which shows that about 1.8 plastic-zone sizes are required to match displacements within 1%.

Finite element crack growth simulations were made with and without CP loading over a wide range in stress ratio, R, from 0 to 0.8. The criteria to match crack-opening loads and CTOD values to within 1% are shown in figure 13. The crack extension, Δc, is normalized by the plastic-zone size from the finite element analysis (ρ_{cp_fea}) along the crack plane axis. The relationship with load ratio appears to be linear, and the crack extension in which the CP loading would have no (or minimal) influence is given by the solid line.

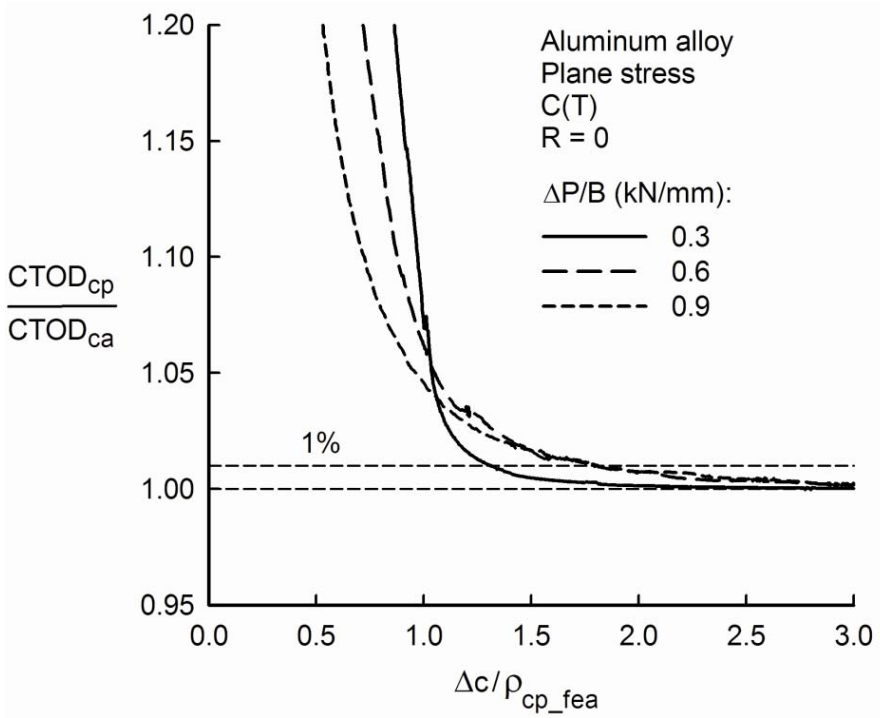

Figure 12. Comparison of CTODs for CA and CPCA Loading

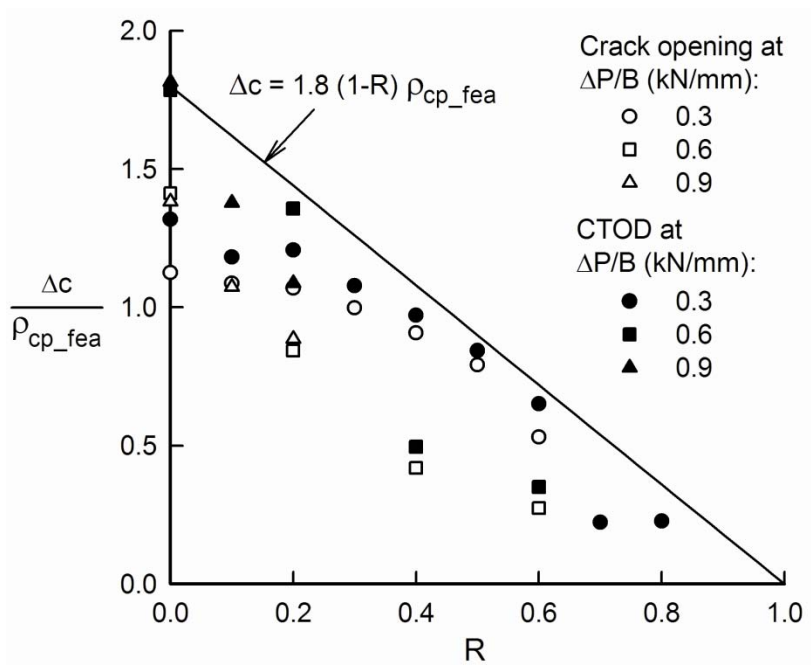

Figure 13. Crack Extension Length Unaffected by Compressive Yielding

4.2.5 The CP and Crack Extension Criteria.

For a given material and crack configuration with a sharp V-notch, the minimum compressive loading is selected by $|K_{cp}| / E = 0.00032 \sqrt{m}$ ($0.002 \sqrt{in.}$). K_{cp} is calculated from the minimum compressive load (P_{cp}) to be applied to the particular crack configuration. For C(T) specimens, the load ratio ($R = P_{cp}/P_{max}$) may be between 10 and 30, and about 30,000 to 60,000 cycles are required to initiate a crack at the V-notch in a variety of materials. The precrack length must be grown beyond the influence of the V-notch, the tensile residual-stress field caused by compressive yielding, and the stabilization of the crack closure behavior under CA loading.

Because the finite element analyses only considered plasticity-induced crack closure, and based on experimental observations (presented later), the crack extension criterion was selected as

$$\Delta c \geq 2\,(1 - R)\,\rho_c \tag{2}$$

and

$$\Delta c \geq 0.5\,H_n \tag{3}$$

whichever is the largest (ρ_c is the plane-stress compressive plastic-zone size and H_n is the notch height). Usually, equation 2 controls the amount of crack extension beyond which valid fatigue crack growth rates are produced. The plastic-zone size is calculated from the Dugdale model [49] and is given by

$$\rho_c = (\pi/8)\,(|K_{cp}| / \sigma_o)^2 \tag{4}$$

where σ_o is the flow stress and is the average between the yield stress, σ_{ys}, and ultimate tensile strength, σ_u.

4.2.6 Constant-ΔK Tests.

The researchers at NASA LaRC proposed using a CP method, which is basically a K-controlled test, as shown in figure 14. Using a notched specimen, a cyclic compressive loading would be applied to initiate a crack at the notch. Then, the specimen would be subjected to a constant ΔK (above the apparent ΔK_{th} threshold) for a given R value. The compressive loading, which yields the notch root, induces a tensile residual stress in front of the notch. The objective of using this technique was to identify the extent of the influence of these residual stresses. But this technique is also an LR procedure because the applied loading has to be decreased with larger crack lengths to maintain the constant ΔK value.

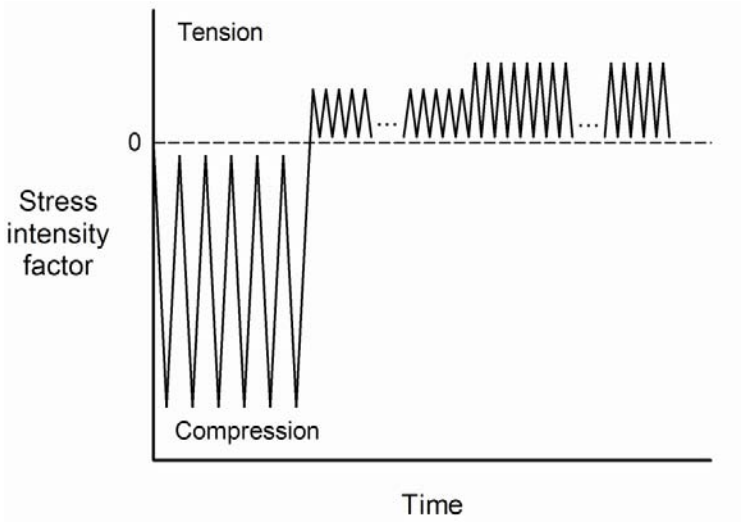

Figure 14. Definition of CPCK Loading

4.2.7 The CPCA Tests.

The CPCA loading procedure, as shown in figure 15, was designed to generate fatigue crack growth rates in the near-threshold regime under CA loading conditions with minimal load-history effects. This type of loading has been demonstrated to produce fatigue cracks at machined notches with minimal load-history effects on both compact and middle-crack tension specimens [27-31]. Once a fatigue crack has been initiated at the notch root, then small tensile loading can be applied to grow the crack under steady-state CA loading from threshold to fracture conditions. Currently, trial-and-error procedures are required to select the initial tensile loading to start the test at the unknown threshold value. If a tensile load is selected that produces a stress-intensity factor range below the threshold, then the crack will not grow; however, if the load is high enough, then the crack will grow. The applied loading is then held constant during the remainder of the test.

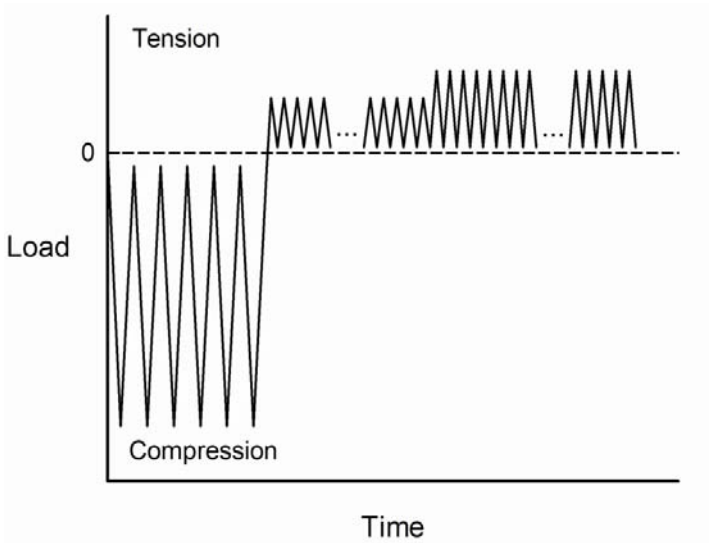

Figure 15. Definition of CPCA Loading

4.2.8 The CPLR Tests.

The CPLR test procedure, as shown in figure 16, was designed to generate a fatigue crack under CP loading and start the LR procedure (like the current ASTM E 647 standard) at a crack growth rate or initiate stress-intensity factor range much lower than the current standard. After CP loading, the crack is grown under CPCA loading until the crack extension criteria are met (equations 2 and 3). Then the LR procedure is initiated following the same guidelines as in ASTM E 647. Once the threshold conditions (less than 1E-10 m/cycle) are met, a load-increasing test is conducted. Once the crack starts to grow, the applied loading is then held constant during the remainder of the test.

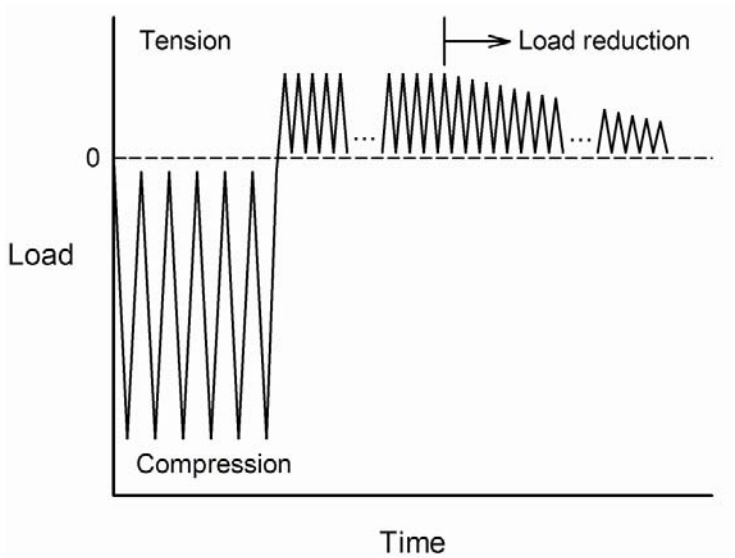

Figure 16. Definition of CPLR Loading

4.3 BACK-FACE STRAIN GAGE CRACK LENGTH MONITORING SYSTEM.

Crack lengths in C(T) specimens were monitored by using an improved BFS gage relation (see appendix A). Compliance relations were developed between the BFS and c, W, B, E, and P. Two stress analysis codes were used to obtain numerical results over a wide range in c/W ratios. An equation fit to the numerical results is given by

$$c/W = A_0 + A_1 U + A_2 U^2 + A_3 U^3 + A_4 U^4 + A_5 U^5 \qquad (5)$$

where $U = 1/(\sqrt{A} + 1)$ and $A = |\varepsilon EBW/P|$ for $0.2 < c/W < 0.95$. Equation 5 is within ±0.2% of the numerical results over a wide range in c/W ratios. The validity of equation 5 for very deep cracks ($0.77 < c/W < 0.93$) was verified on tests conducted on several materials (see appendix A).

5. MATERIALS TESTED AT MSU.

Three materials were tested at MSU using the current ASTM LR test procedure and the newly developed CP threshold test methods. Aluminum alloy, titanium alloy, and steel were tested over a wide range of load ratios with fatigue crack growth rates generated from threshold to near

fracture. Another aluminum alloy (7050) was tested at MSU only at a low load ratio (R = 0.1) to compare with more extensive tests conducted at NASA LaRC (see section 6.1).

5.1 ALUMINUM ALLOY 7075-T651.

The 7075-T651 aluminum alloy (B = 5.7 mm) material was obtained from Northrop Grumman Corporation and had been machined from near the outer surface of a 50-mm-thick plate to simulate the location of the outer wing-plank material on a naval aircraft. All specimens were tested in the LT-orientation (crack plane perpendicular to the rolling direction). Twenty-two C(T) specimens (W = 76.2 mm) were machined and ten specimens were sent to Dr. John Ruschau, University of Dayton Research Institute, to further evaluate the new CP test methods. The aluminum alloy specimens had a 60-degree V-notch that had a very small notch-root radius (0.08-mm). Fatigue crack growth tests were conducted over a wide range of stress ratios ($0.1 \leq R \leq 0.9$) using the three threshold test methods.

5.1.1 Fatigue Crack Growth Tests.

Normally, CP is performed without measuring the growth of the crack under compression-compression loading. Only the final crack extension is recorded. But two C(T) specimens were fatigue precracked under CP loads to measure crack extension during the compressive stage. Figure 17 shows the results on the aluminum alloy. These two tests were fatigue precracked at a compressive stress-intensity factor (K_{cp}) of -22 MPa√m for about 50,000 cycles. The final crack extension was about 0.15 mm (0.006 in.). The final crack extension measured in these specimens was about a factor of 2 or 3 less than what has been found on other materials. However, even with this smaller amount of crack extension, the stress-intensity factor for tension-applied loads was only about 6% lower than the standard C(T) solution due to notch effects.

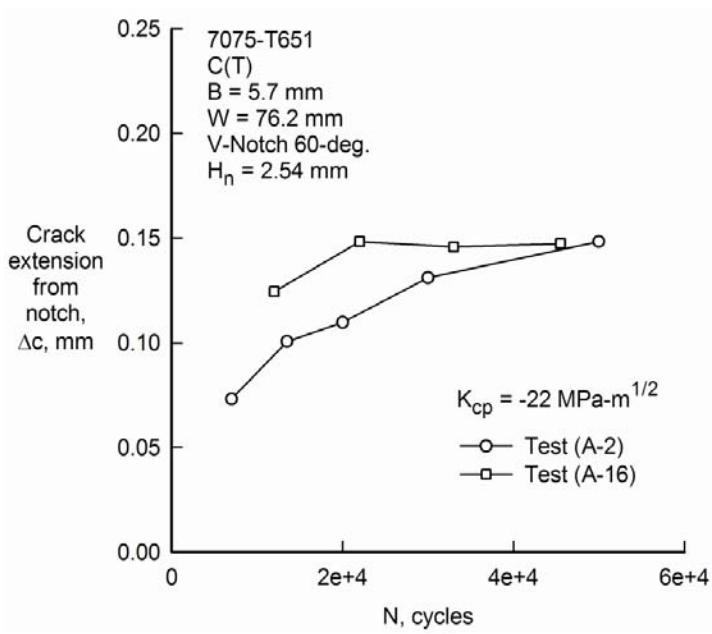

Figure 17. Crack Extension Under Compressive Loading for Two 7075-T651 C(T) Specimens

In CP tests, less than 100,000 cycles are required to stabilize the compressively grown cracks. In the proposed annex to ASTM E 647, the compressive cycling will be required to be conducted at compressive stress-intensity factor levels that will produce fatigue cracks in less than 100,000 cycles. Thus, criteria were developed on the basis of $|K_{cp}|/E$ that would apply for any material.

Four tests have been conducted on C(T) specimens at R = 0.1 and these results are shown in figure 18. Three specimens were tested using the new CPCA test method, while one specimen used the traditional ASTM LR test method. After CP, Test 1 had an initial ΔK (at constant loads) slightly higher than the estimated threshold. From the crack length against cycles data, the secant method was used to calculate ΔK against rate data. The initial data was affected by the tensile residual stresses, but the diamond symbol at the highest ΔK value shows where the crack extension criterion is met for Test 1. For higher ΔK-rate data, the results are considered valid. A second test was then conducted at a slightly lower initial ΔK value, and the data agreed with the first test results after the crack extension criterion was met. But a third test had an initial ΔK value much lower than the estimated threshold. Under the initial CA loading, the crack growth rates rapidly dropped down to almost 10^{-11} m/cycle. The maximum load was then increased by 10% and the rates again rapidly dropped. The maximum load was again increased by 5% and the rates were now sporadic, indicating that the crack was close to a threshold condition. The last load increase of 5% caused the rates to slowly increase, as shown in the figure. Again, the lowest diamond symbol shows the crack extension criterion for Test 3. From start to finish, Test 3 consumed about 15 million cycles.

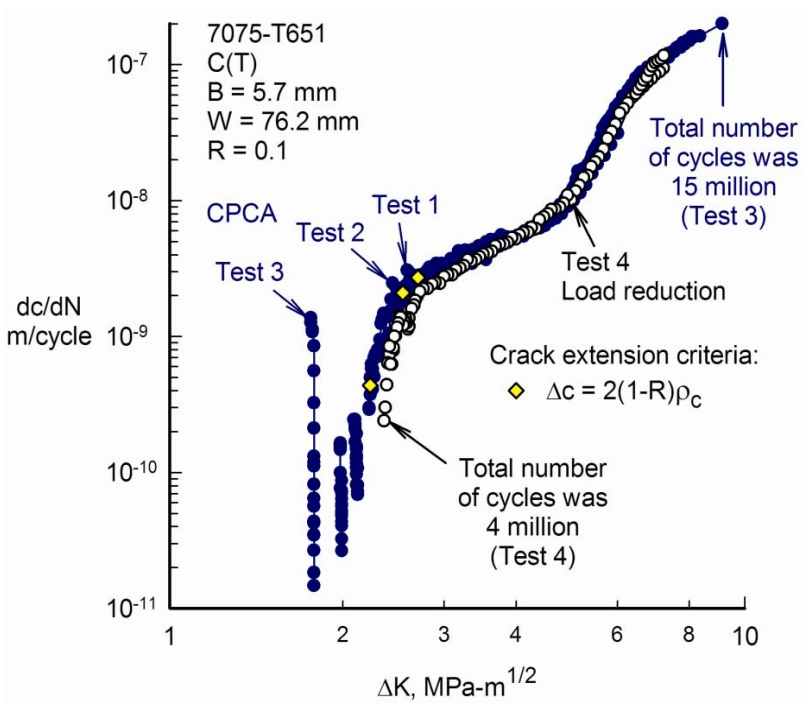

Figure 18. Fatigue Crack Growth During ASTM LR and CPCA Tests on 7075-T651 at R = 0.1

The open symbols show results of a single ASTM LR test that fell at slightly lower rates than the CPCA test results and would have produced a slightly higher threshold. The differences are not considered significant and, thus, these results are essentially in agreement. Further tests at

R = 0.1 and 0.7 (not shown) also showed good agreement between the two test methods [30]. However, the CPCA test method required a factor of 3 more cycles to achieve the same results. The CPLR test method was not used on this material, but would have took far less cycles than the CPCA method, very much like the LR test. For example, Test 1 or 2 could have been used to conduct an LR test after the crack extension criterion was met. In all tests, the crack surfaces were fairly flat and the cracks grew very straight.

Another test at R = 0.1 was intentionally grown to crack growth rates much higher than the ASTM maximum-allowed rate (1E-08 m/cycle), and then, an LR test was conducted. These test results, shown in figure 19 (square symbols), show a significant deviation from the expected behavior (ASTM LR and CPCA test results). This test also produced a deviation in the midregion as well as a significantly higher threshold. These test results help to demonstrate the load-history effects due to load shedding (from residual plastic deformations) and suggest that there may be a width effect, such as that shown by Garr and Hresko [50] and Ruschau and Newman [31]. A larger width specimen may produce a higher threshold and slower rates than the 76-mm-wide C(T) specimens. A large-width specimen will have longer cracks and lower applied loads during the load-shedding process. Thus, the crack surface displacements will be lower than in smaller-width specimens, and this may produce premature crack surface contact. The limited results do show that the threshold was elevated to about 3.5 MPa√m, a value typical of that found in older literature on the 7075 alloys, such as that shown by Pearson [51].

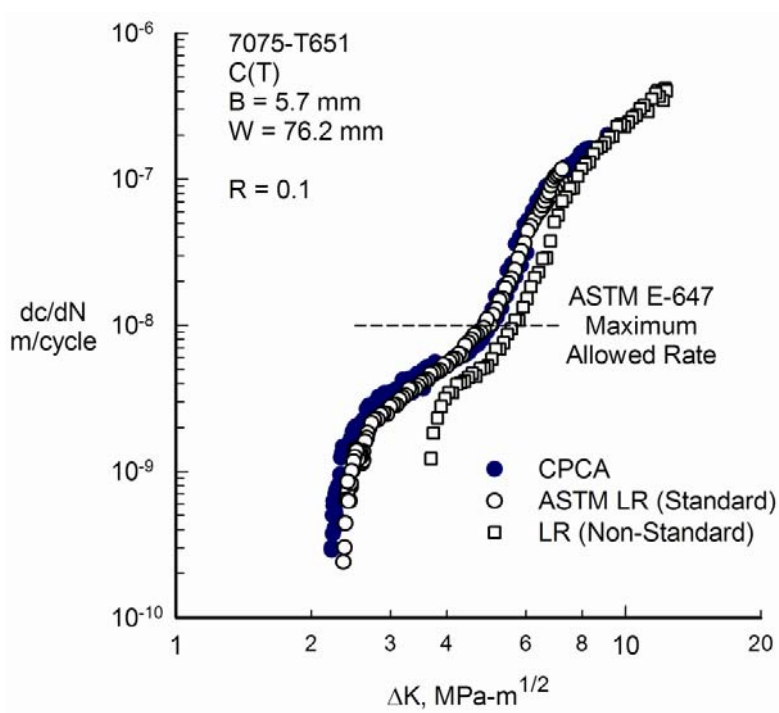

Figure 19. Fatigue Crack Growth During Standard and Nonstandard ASTM LR Tests

Figure 20 shows a comparison among crack growth rate data generated on various 7075 alloys at R = 0.1. Previous CPCA and ASTM LR tests are also shown. The solid-square symbols show the results of a CPLR test. After CP, CA loading was selected to grow the crack higher than the ΔK_{th} value and held constant until the crack had grown beyond the crack extension criterion

(equation 2). Then, a standard LR test was conducted to generate the lower crack growth region and the threshold value. The CPLR and CPCA test results agreed very well, and both were slightly lower than the ASTM LR test results. This figure also shows data from Alcoa [52] on M(T) specimens using the ASTM LR procedure (but at a relatively high humidity), which shows a significantly higher threshold. Tests under a high humidity will create more fretting oxide debris (higher crack-opening loads and higher thresholds) than tests conducted at lower humidity. The solid lines are curves fit to test data on a thin-sheet alloy tested at NASA LaRC [53], which gave a slightly lower threshold behavior for large cracks and significantly lower results for small cracks.

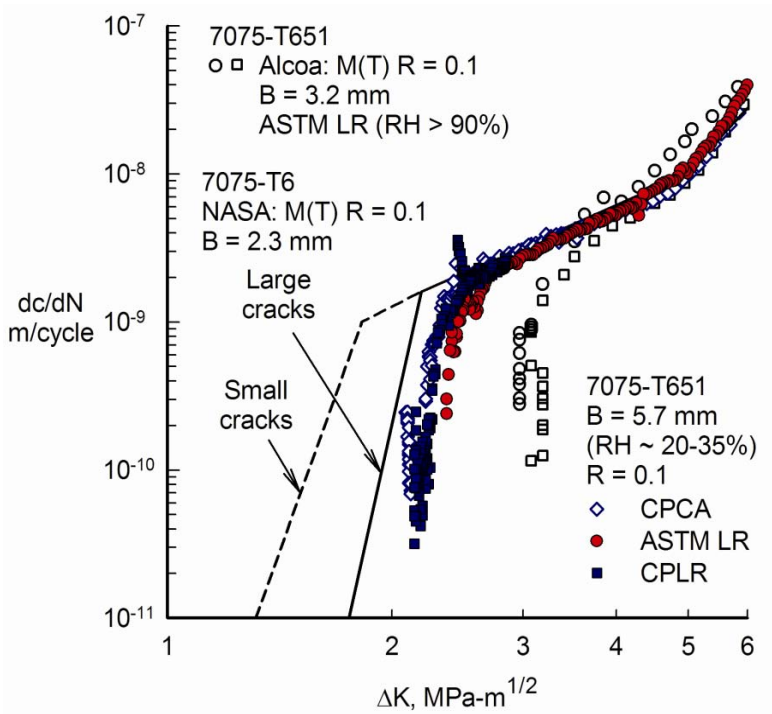

Figure 20. Comparison of Results From C(T) and M(T) Specimens on 7075-T651

A summary of all test data generated on the 7075-T651 alloy is shown in figure 21. The plot shows the typical stress ratio (R) shift in the ΔK-rate data, but the R = 0.9 results were noticeable different than the R = 0.7 test data. In the past, it had been assumed on the basis of remote crack closure measurements and plasticity-induced crack closure analyses, that above a stress ratio of about 0.7, the cracks were fully open. However, recent local measurements of crack closure for crack growth at high stress ratios (R >0.7) have shown significant amounts of crack closure [21 and 22]. Thus, it is suspected that the shift in data from R = 0.7 to 0.9 may have been caused by crack closure behavior due to roughness and/or fretting debris.

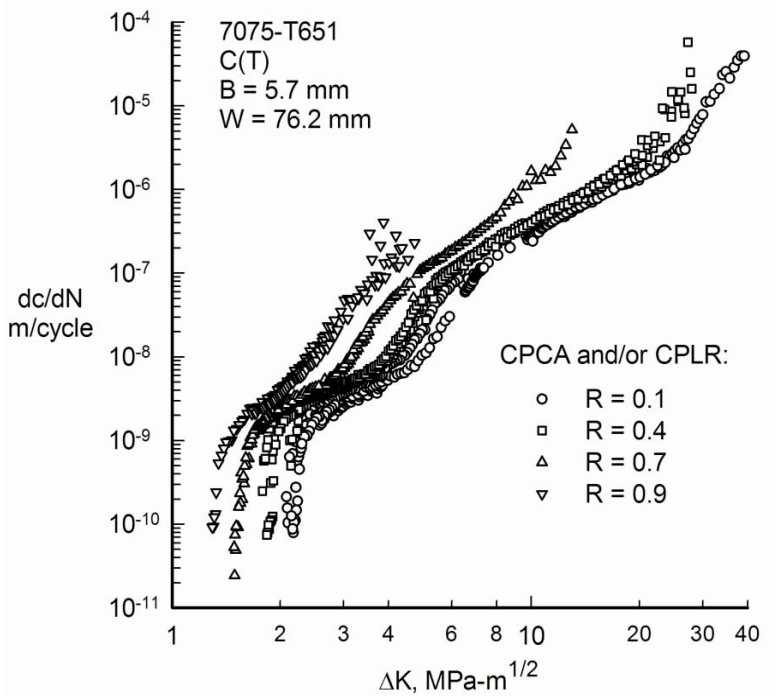

Figure 21. Fatigue Crack Growth Data Over a Wide Range in Stress Ratios and Rates for 7075-T651

5.1.2 Crack Closure Analyses.

A crack closure analysis of the fatigue crack growth rate data was made to correlate the data into a narrow band over a wide range of stress ratios and rates from the threshold regime to near fracture. A crack closure analysis was conducted on all C(T) tests to indirectly determine the crack-opening load (P_o/P_{max}) ratio for each R ratio. Because the high-R tests (R $\geq$0.7) were considered to be the results for a fully opened crack, the ΔK-against-rate results at R = 0.7 were assumed to be the effective stress-intensity factor range against rate relation (ΔK_{eff} = U ΔK where U = 1). For the C(T) specimen data, an indirect method was used to estimate the P_o/P_{max} ratio or U for each set of data at a given R. The value of U is found by trial-and-error to shift the low-R data to approximately fit the R = 0.7 curve. These results are shown in figure 22, which shows P_o/P_{max} against R. The C(T) specimen results (circular symbols) show the usual behavior as a function of R. Using the crack-opening stress (or load) equations in reference 54, a value of the constraint factor (α) was selected to fit these data. An α value of 2.0 fit the C(T) data quite well (solid curve).

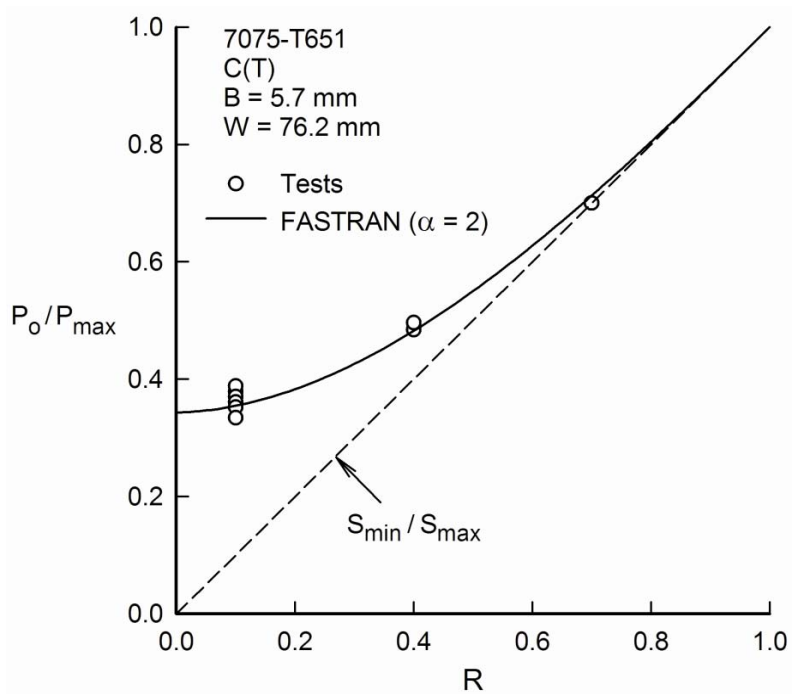

Figure 22. Indirect Determination of Crack-Opening Loads and Constraint Factor for 7075-T651

The crack-opening load ratio equation (solid curve) asymptotically approaches the fully open crack results (dashed line) as R approaches unity. This behavior is believed to be physically correct. However, if FASTRAN [55] is used to simulate crack growth under R = 0.7 conditions at $\alpha = 2$, then the crack will be fully open, i.e., $P_o = P_{min}$ or U = 1. This is due to the modeling approximations and the size of the crack growth elements, which are 20% of the cyclic plastic zone. Thus, the R = 0.7 or higher R-value results are generally assumed to be data for a fully opened crack. But currently, the crack-opening load equations slightly overestimate the P_o/P_{max} ratio for R = 0.7, as shown in figure 22. In the future, the crack-opening stress (or load) equations may be modified to more closely match the FASTRAN analyses for the high-R conditions.

The determination of the effective stress-intensity factor range against rate relation for the 7075-T651 data is shown in figure 23. The symbols show the results on specimens tested with the CPCA/CPLR test procedures over a wide range in R ratios from threshold to near fracture. Test data with R values from 0.1 to 0.7 correlated well into a narrow band over about 6 orders of magnitude in rates. The solid curve with circular symbols shows the estimated ΔK_{eff} baseline curve. At extremely high rates approaching fracture, differences were observed in the various tests as a function of R. These differences are due to the fact that linear-elastic stress-intensity factors are not controlling fracture. The fracture ΔK_c asymptote (rates going to infinity) is a function of R, roughly the elastic fracture toughness K_{Ie} (or K_c) times (1 -R). Thus, high-R tests will fail at low values of ΔK_c. The reason for the selection of the ΔK_{eff}-rate curve at lower rates than the test data in the upper region will become apparent later. Here the ΔK_{eff}-rate curve should be obtained from very large-width specimens, which would not have rates affected by the fracture toughness (see appendix B).

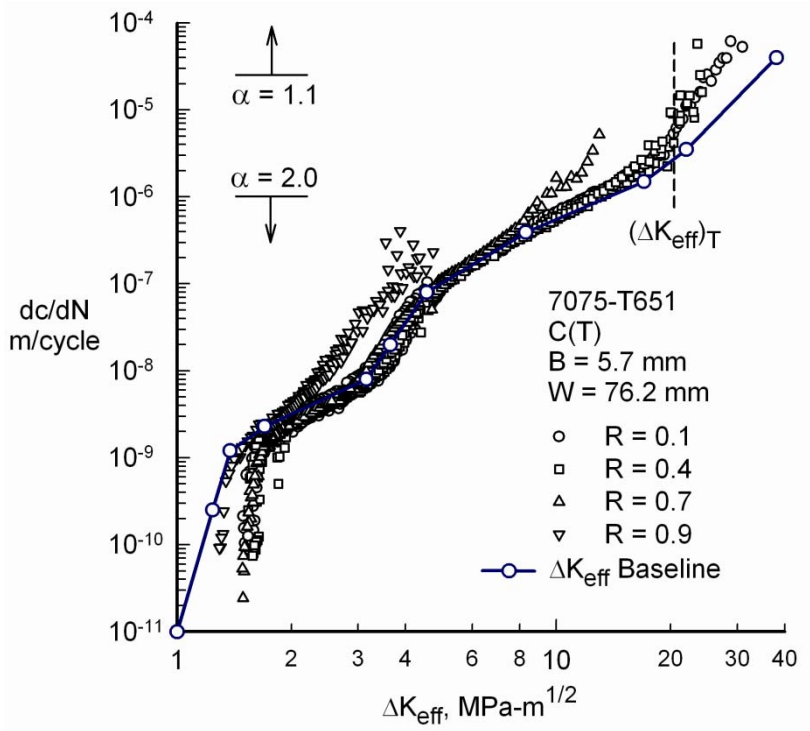

Figure 23. Effective Stress-Intensity Factor Range Against Rates for 7075-T651

Fatigue crack growth rate differences also occurred in the constraint loss regime (associated with the flat-to-slant crack growth mechanism). The vertical dashed line shows the calculated effective stress-intensity factor range at the transitional region (see appendix B).

Surprisingly, the R = 0.9 data showed a significant shift from the ΔK_{eff} baseline curve. This shift may be caused by either a K_{max} or crack closure effect. However, based on recent local crack-opening load measurements made at high-R (≥0.7) and K_{max} tests on an aluminum alloy and a superalloy [21 and 22], the shift is most likely due to crack closure behavior. It is unclear whether this shift is due to roughness- and/or fretting debris-induced crack closure. But the plasticity-induced crack closure model [55] is unable to correlate or predict these data.

In the threshold regime, the effective stress-intensity factor threshold, ΔK_o, is a function of the stress ratio, as shown in figure 24. From R = 0.1 to 0.7, the ΔK_o values were nearly constant, but dropped at R = 0.9. Similar to using a fracture term to help model the approach to fracture as a function of the stress ratio in the upper-rate regime, the crack growth rate equation has a term to model the approach to threshold (see appendix B). The functional form selected is a power-law equation, like that proposed by Klesnil and Lukas [56], except the effective stress-intensity factor range is used instead of linear-elastic ΔK_{th}. A fit to the threshold data on the 7075-T651 alloy is shown by the solid curve.

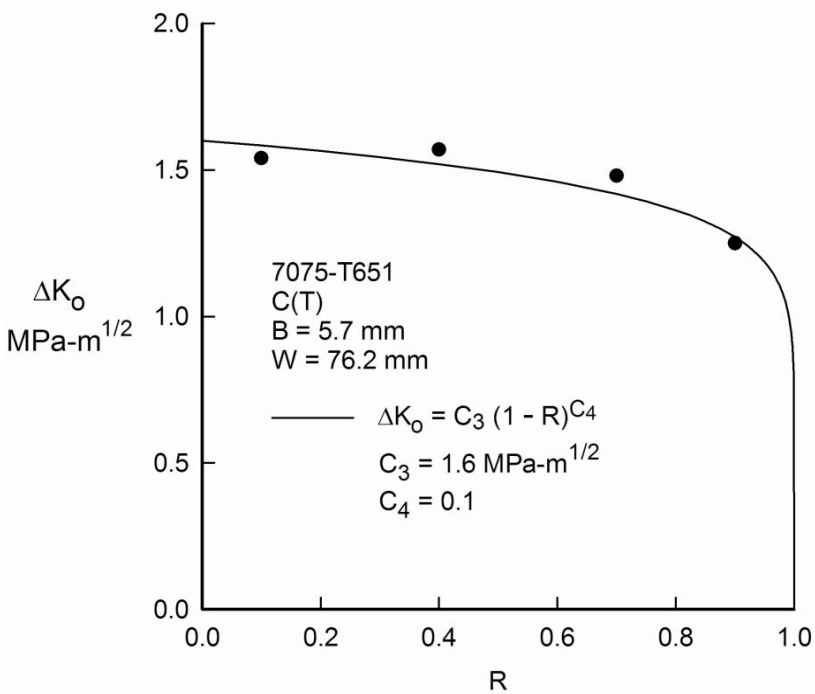

Figure 24. Effective Stress-Intensity Factor Range Thresholds for 7075-T651

To more accurately model the upper-rate region on a ΔK-rate curve, the elastic fracture toughness (K_{Ie}) must be determined. In the early 1970s, Newman [57 and 58] proposed the Two-Parameter Fracture Criterion (TPFC) to correlate fracture data and to predict failure loads on cracked metallic materials. The fracture toughness was obtained from both the fatigue crack growth specimens and from some other fracture specimens. Figure 25 shows K_{Ie} against the initial crack length-to-width (c_i/W) ratio for C(T) specimens. Both 76- and 152-inch-wide specimens were either fatigued to failure or fatigued to a given crack length and then statically pulled to failure. The crack lengths under the fatigued-to-failure conditions were quite large, greater than about 70% of the width (beyond any current fracture standards). These results show that K_{Ie} is a function of crack length and width. Larger-width specimens produced larger K_{Ie} values at failure for the same crack length, and the K_{Ie} values approached zero as the crack length approached the specimen width. The fracture toughness, K_F was found to be 88 MPa√m and m = 0.7. The TPFC fit the test data fairly well.

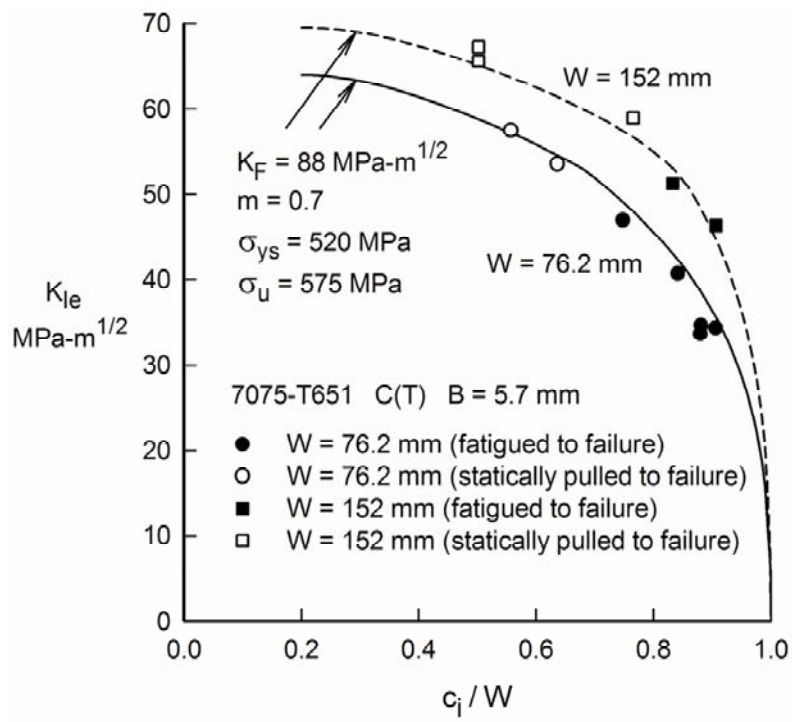

Figure 25. Elastic Stress-Intensity Factors at Failure for 7075-T651 C(T) Specimens

To illustrated how the effective stress-intensity factor threshold and elastic fracture toughness affects the ΔK-rate curve, the crack growth relation used in FASTRAN is

$$dc/dN = C_{1i}\,(\Delta K_{eff})^{C_{2i}}\,[1 - (\Delta K_o/\Delta K_{eff})^p]/[1 - (K_{max}/C_5)^q] \qquad (6)$$

where C_{1i} and C_{2i} are the coefficient and power, respectively, for each linear segment, ΔK_{eff} is the effective stress-intensity factor, ΔK_o is the effective threshold, K_{max} is the maximum stress-intensity factor, C_5 is the elastic cyclic fracture toughness ($C_5 = K_{Ie}$, which is generally a function of crack length, specimen width, and specimen type), and p and q are constants selected to best fit test data in either the threshold or fracture regimes. Whenever the applied K_{max} value reached or exceeded C_5 (or K_{Ie}), then the specimen or component would fail. Likewise, in the threshold regime, if the ΔK_{eff} is equal to ΔK_o then the crack growth rate goes to zero, and the value of p controls the shape of the rate curve in the near-threshold regime.

Because of the R = 0.9 data, the ΔK_{eff}-rate curve in the lower rate region was selected to fit these data instead of the usual R = 0.7 data. The baseline curve is shown in figure 23 as the solid lines (linear segments) with open circular symbols. The effective stress-intensity factor range against rate relation and other associated properties are given in table 7.

Table 7. Effective Stress-Intensity Factor Range Against Rate Relation for 7075-T651 (B = 5.7 mm)

ΔK_{eff}, MPa√m	dc/dN, m/cycle	ΔK_{eff}, MPa√m	dc/dN, m/cycle
1.00	1.0e-11	22.0	3.5e-06
1.24	2.5e-10	38.0	4.0e-05
1.38	1.2e-09	α_1 = 2.0	1.0e-06
1.70	2.3e-09	α_2 = 1.1	2.5e-05
3.15	8.0e-09	C_3 = 1.6 MPa√m	C_4 = 0.1
3.65	2.0e-08	q = 10	---
4.55	8.0e-08	C_5 = 45 MPa√m	q = 2
8.30	3.9e-07	K_F = 88 MPa√m	m = 0.7
17.0	1.5e-06	σ_{ys} = 520 MPa	σ_u = 575 MPa

The solid curve in figure 26 shows the predicted behavior from equation 6 for the R = 0.9 case using the properties from table 7. For simplicity, the fracture toughness, C_5,was held constant at 45 MPa√m. (In practice, however, the fracture constants, K_F and m, should be used to calculate the elastic stress-intensity factor at failure.) The fracture term in equation 6 caused the predicted rates to approach fracture at a ΔK_c value of 4.5 MPa√m. Figures 27 to 29 show the predicted behavior from equation 6 for R = 0.7, 0.4, and 0.1, respectively. The predicted results (solid curves) agreed very well with the test data from threshold to fracture.

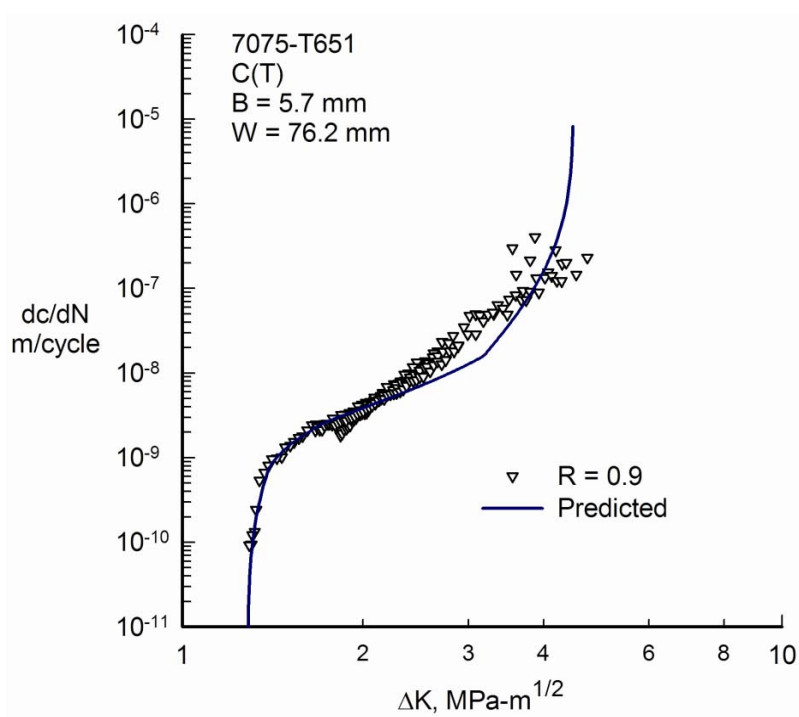

Figure 26. Measured and Predicted Crack Growth Rates on 7075-T651 at R = 0.9

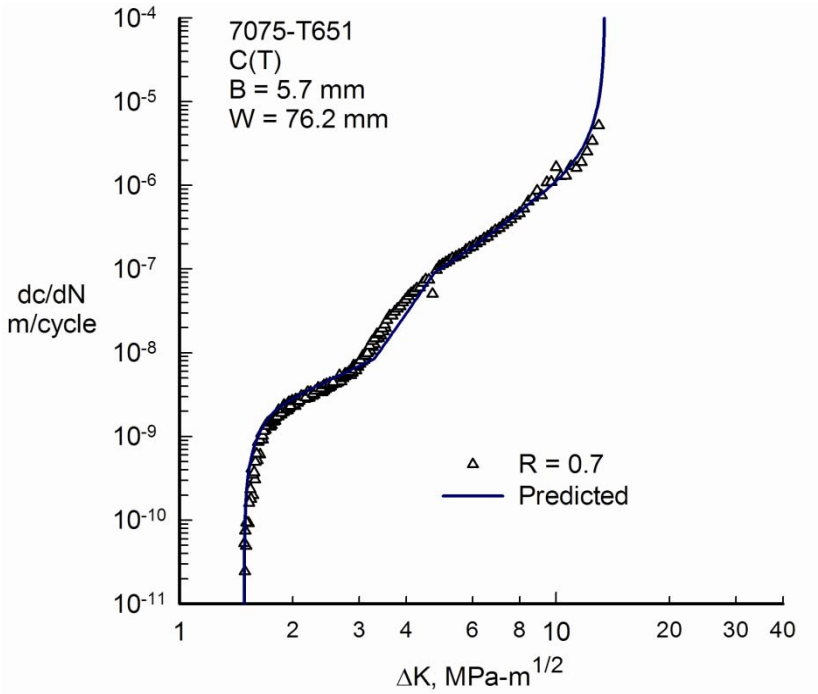

Figure 27. Measured and Predicted Crack Growth Rates on 7075-T651 at R = 0.7

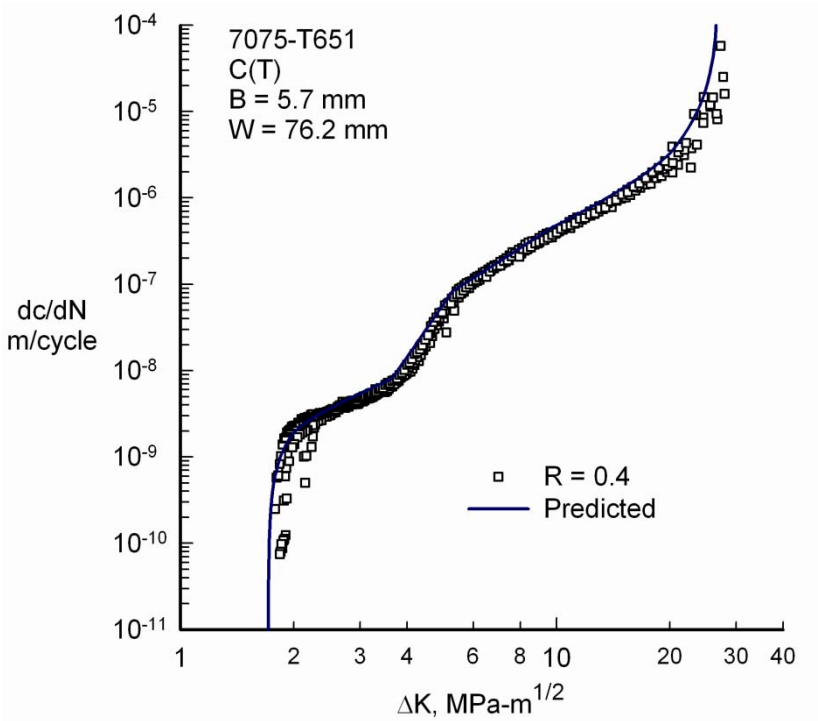

Figure 28. Measured and Predicted Crack Growth Rates on 7075-T651 at R = 0.4

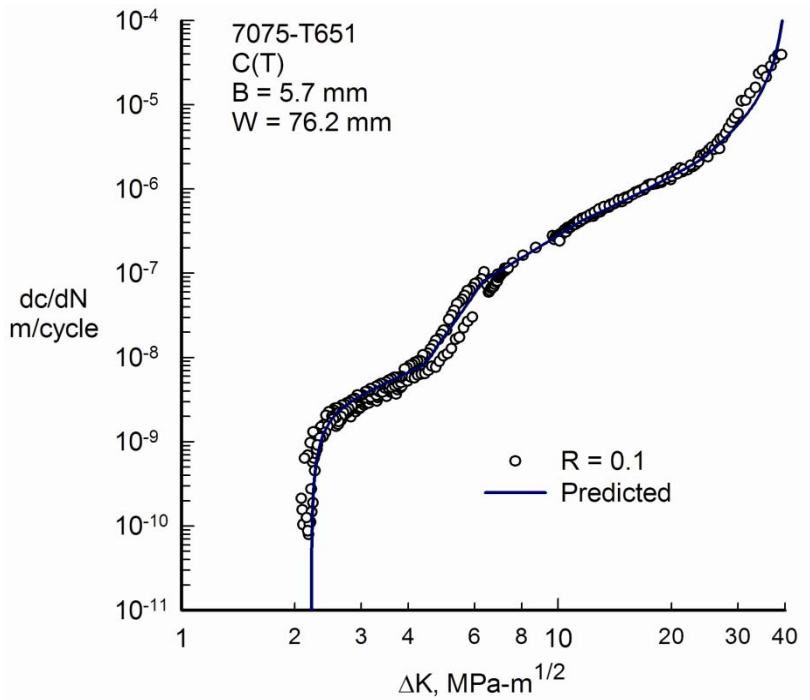

Figure 29. Measured and Predicted Crack Growth Rates on 7075-T651 at R = 0.1

5.2 TITANIUM ALLOY Ti-6Al-4V β-STOA.

The titanium alloy C(T) specimens were machined from blanks cut out of a forging block, as shown in figure 5. Thirty specimens were machined, 10 in each orientation (LS, SL, and TS). Tests were conducted over a wide range in stress ratios ($0.1 \leq R \leq 0.8$), except an R = 0.9 test was conducted on one specimen in the LS orientation. Again, the three types of threshold tests (ASTM LR, CPCA, and CPLR) were conducted, and crack growth rate data was generated from threshold to near fracture. See section 6.2 for further results on a similar titanium alloy.

5.2.1 Fatigue Crack Growth Tests (LS Orientation).

Several titanium alloy specimens were tested under compression-compression loading to measure crack growth from the V-notch. These results are shown in figure 30. Again, the crack extension from the V-notch was smaller than expected and ranged from 0.1 to 0.15 mm from the notch tip. Because the V-notch angle was 45 degrees, the stress-intensity factors under tensile loading were 5% to 8% lower than the standard C(T) specimen solution (see figure 9). However, these slightly lower values did not cause any problems in growing cracks under tensile loading.
The results shown in figures 31 and 32 show tests conducted using the ASTM LR procedures and CPCA or CPLR, respectively. The tests shown in figure 31 were conducted under R = 0.1 loading, and those in figure 32 were conducted under R = 0.4 loading. In two ASTM LR tests (LS1 and LS3), no CP loads were applied and the crack was grown from the V-notch under CA loading until the crack growth rate reached the maximum-allowed rate in ASTM E 647. Then a standard LR test with a normalized K-gradient, (dK/dc)/K, of -0.08 mm^{-1} was used. The apparent scatter in this material, due to the large-grain microstructure and possible residual stresses, caused some dramatically different behavior during these tests. Unfortunately, only one

test (LS7) was conducted with the CPCA procedures, which produced data that fell to the lower side of all these data. But LS7 results agreed well with the LS1 data until the results dropped to threshold conditions. CA loading was then used to generate data above the horizontal dashed line.

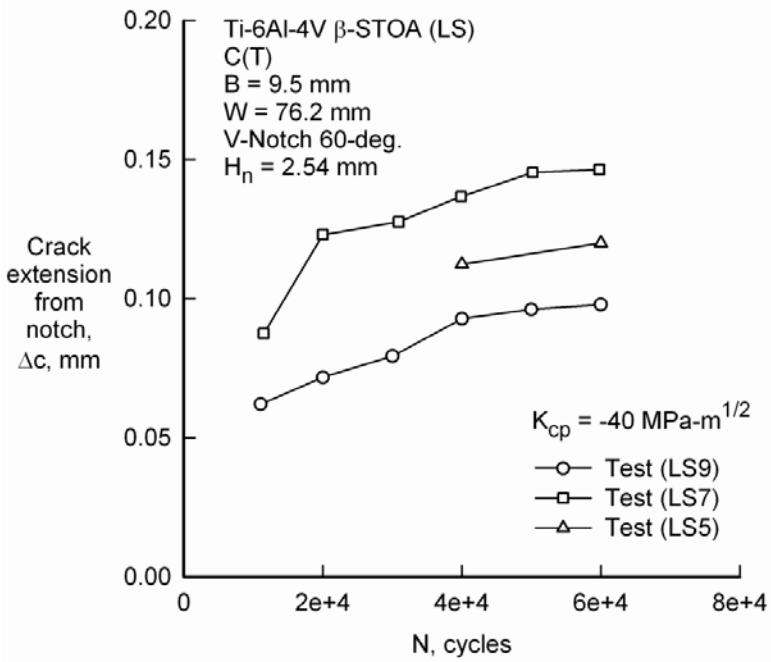

Figure 30. Crack Extension Under Compressive Loading for Ti-6Al-4V β-STOA (LS)

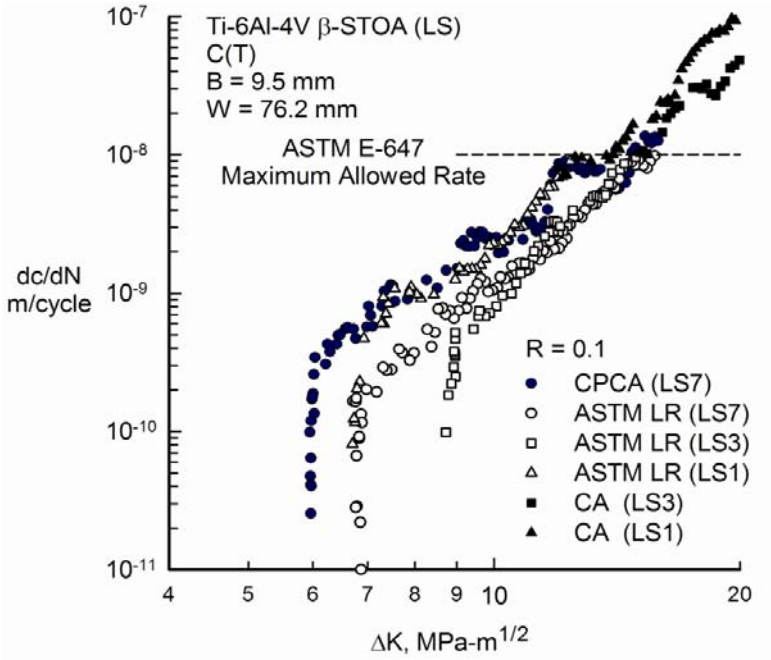

Figure 31. Fatigue Crack Growth During ASTM LR and CPCA Testing for Ti-6Al-4V β-STOA (LS) at R = 0.1

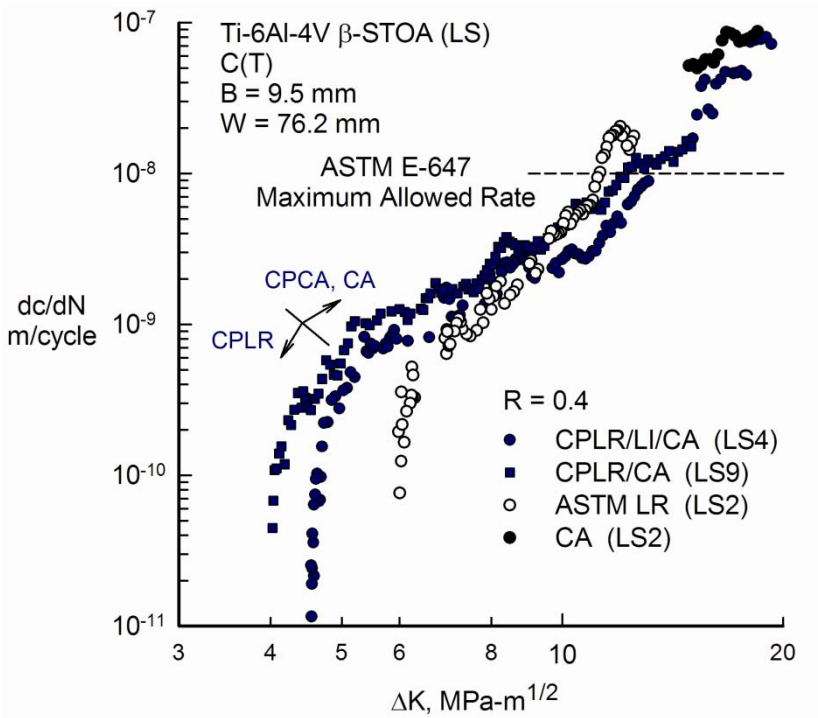

Figure 32. Fatigue Crack Growth During ASTM LR and CPLR Testing for Ti-6Al-4V β-STOA (LS) at R = 0.4

For the R = 0.4 test conditions, two tests were conducted under the CPLR test procedures. After CP and growing the crack for several compressive plastic-zone sizes from the V-notch, the standard LR test procedures were used to generate threshold data. Then CA loading at a slightly higher load was used to generate additional data at higher rates. The double arrows mark the boundary between LR and CA loading. A single ASTM LR test was conducted at R = 0.4. Unfortunately, the maximum rate exceeded the ASTM maximum-rate criteria by a factor of 2, and produced a higher threshold. Whether this was due to violating the standard, microstructural influences, or residual stresses could not be determined.

A summary of all test data generated on the titanium alloy in the LS orientation, excluding those generated using the ASTM LR test procedures, is shown in figure 33. The plot shows the typical stress ratio (R) shift in the ΔK-rate data, but the R = 0.9 results were noticeable different than the R = 0.7 test data in the threshold regime (below 1E-09 m/cycle).

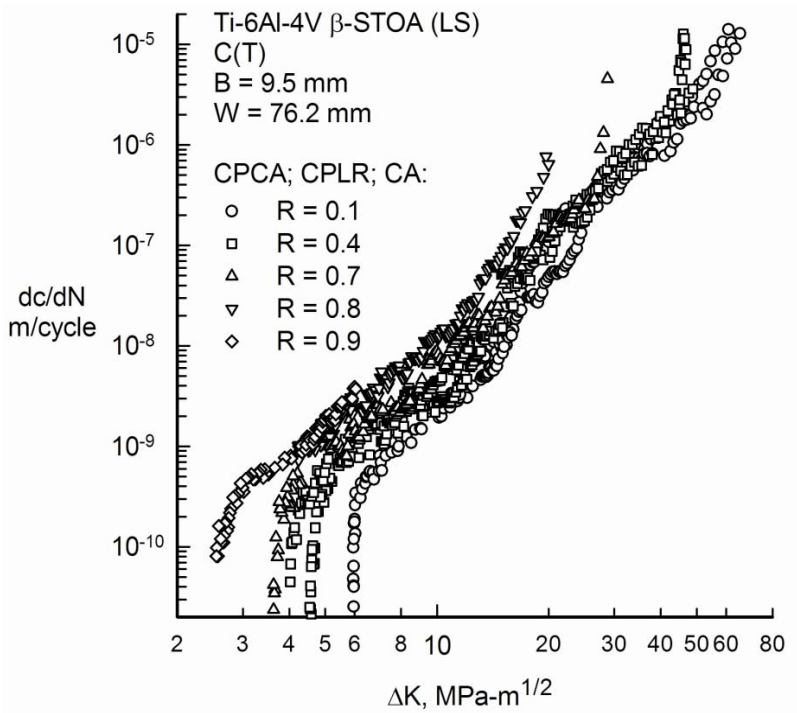

Figure 33. Fatigue Crack Growth Data Over a Wide Range in Stress Ratios and Rates for Ti-6Al-4V β-STOA (LS)

5.2.2 Fatigue Crack Growth Tests (SL Orientation).

Figure 34 shows a comparison of test data generated under R = 0.4 conditions for the SL orientation. Two types of tests were conducted after CP loading, one with CA loading and the other with LR conditions. For SL9, after CP, the CA loads were held constant and data were generated under steady-state conditions. Here, only data that satisfied the two compressive plastic-zone criteria are plotted. For SL2, after CP and growing the crack for several compressive plastic-zone sizes from the V-notch, the standard LR test procedures were used to generate threshold data. Then CA loading at a slightly higher load was used to generate additional data at higher rates. Again, the double arrows mark the boundary between LR and CA loading. In the single ASTM LR test (SL6), no CP loads were applied and the crack was grown from the V-notch under CA loading until the crack growth rate reached the maximum-allowed rate in ASTM E 647. Then a standard LR test with the standard K-gradient was used. The ASTM LR results deviated greatly from the two CP tests in the midregion as well as in the threshold regime.

A summary of all test data generated on the titanium alloy in the SL orientation, again excluding those generated using the ASTM LR test procedures, is shown in figure 35. Again, the plot shows the typical stress ratio (R) shift in the ΔK-rate data, but these results show a larger R shift in the midregion data than those generated under the LS orientation. The R shift in the threshold regime was about the same in both orientations.

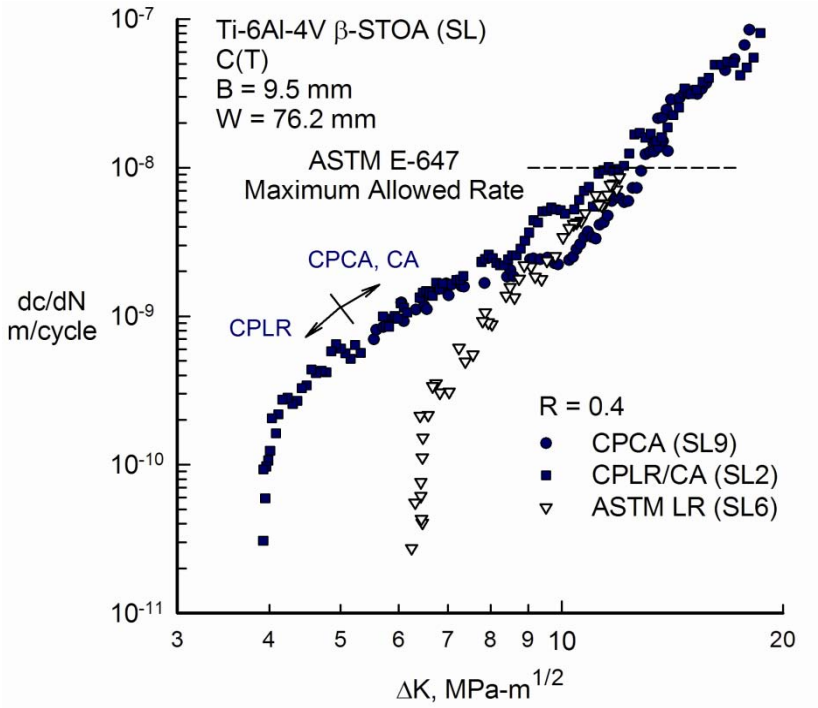

Figure 34. Fatigue Crack Growth During ASTM LR and CPLR Tests for Ti-6Al-4V β-STOA (SL) at R = 0.4

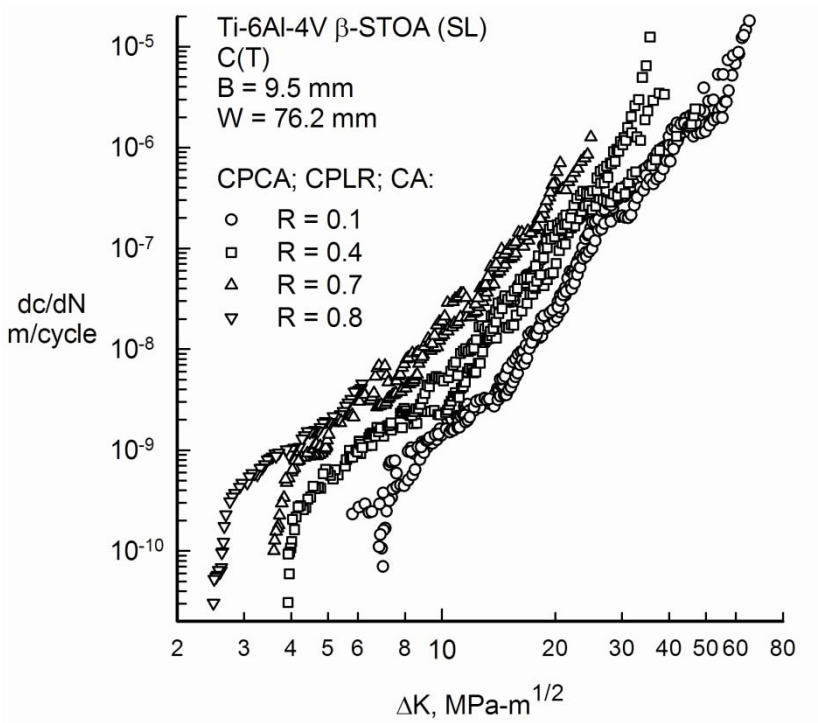

Figure 35. Fatigue Crack Growth Data Over a Wide Range in Stress Ratios and Rates for Ti-6Al-4V β-STOA (SL)

5.2.3 Fatigue Crack Growth Tests (TS Orientation).

Because of the large scatter observed in the LS and SL orientations, duplicate tests were conducted on the TS orientation using the ASTM LR and CPCA/CPLR tests. Figure 36 shows the results for both R = 0.1 and 0.4 test conditions. These results show that the CP test methods consistently produced lower thresholds and faster rates in the near-threshold regime. Very good agreement between all test methods was observed in the midrate region.

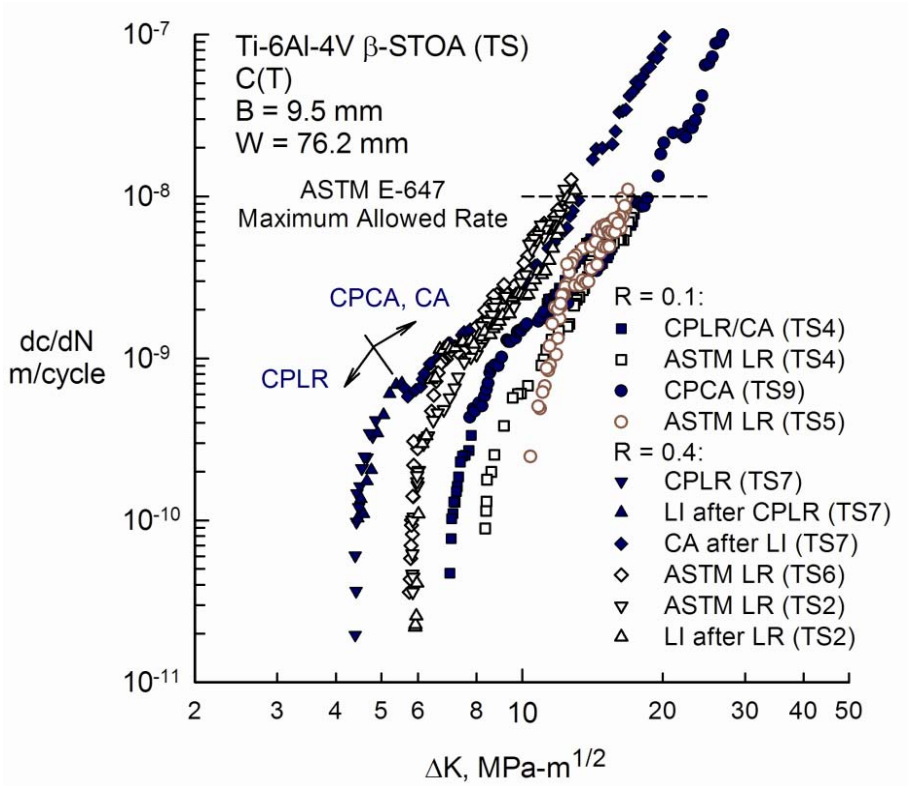

Figure 36. Fatigue Crack Growth During ASTM LR and CPLR Tests for Ti-6Al-4V β-STOA (TS) at R = 0.1 and 0.4

A summary of all test data generated on the titanium alloy in the TS orientation, again excluding those generated using the ASTM LR test procedures, is shown in figure 37. The plot shows the typical stress ratio (R) shift in the ΔK-rate data, but these results show a larger R shift in the midregion data than those generated under the LS orientation.

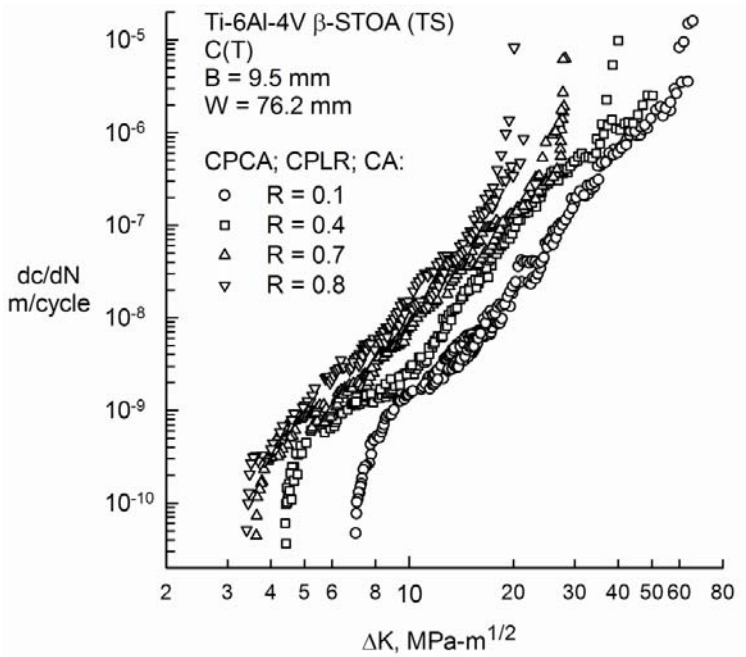

Figure 37. Fatigue Crack Growth Data Over a Wide Range in Stress Ratios and Rates for Ti-6Al-4V β-STOA (TS)

5.2.4 Validation of Crack Extension Criterion for Titanium Alloy.

One of the major concerns with the CP test methods is the tensile residual stresses caused by compressive yielding at the V-notch. Elastic [43] and elastic-plastic [44] finite element modeling on the influence of the tensile residual stresses did not model roughness- and/or fretting debris-induced crack closure effects (only plasticity effects) in establishing the region beyond which the tensile residual stresses and the stabilization of the crack closure behavior would produce steady-state CA loading conditions. Due to the large-grain microstructure, the titanium alloy exhibits a very rough and tortuous crack path with meandering and bifurcating crack surfaces.

CPCK tests were conducted on C(T) specimens from the three orientations at either R = 0.1 or 0.4. These results are shown in figures 38 to 40. The measured crack growth rates during constant ΔK loading, immediately after CP loading, are plotted against crack extension from the notch (Δc) normalized by (1-R) ρc. The plastic-zone size, ρc, was calculated from the Dugdale model small-scale yielding equation (equation 4). The vertical dashed line is at a normalized crack extension value of 2. These test results support even a lower ratio of about 1 for the titanium alloy on all three orientations. These results are significant because the fatigue crack surfaces on the titanium specimens are very rough with meandering and bifurcating cracks. Thus, the current crack extension criterion is validated for a material, which generates a very rough crack surface.

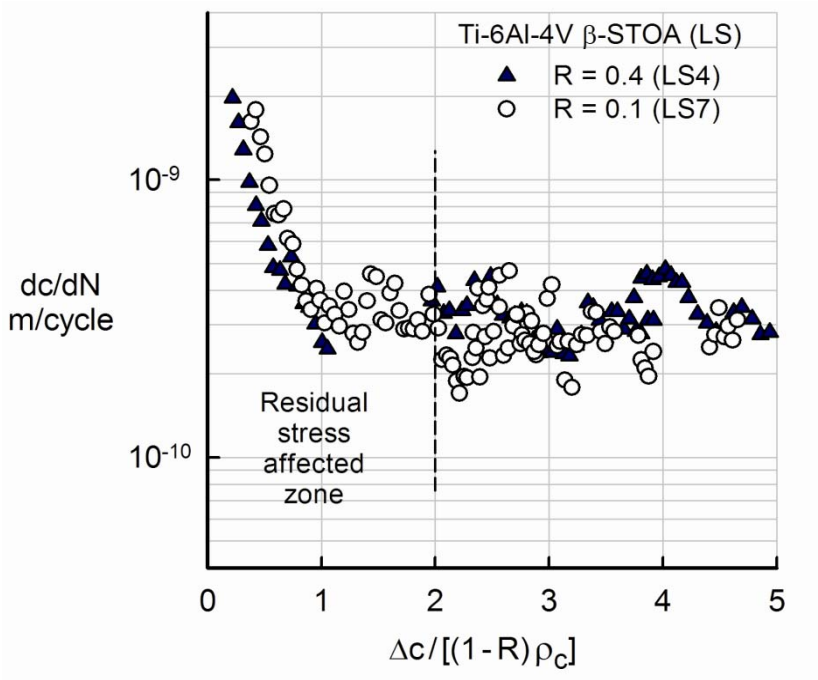

Figure 38. Crack Growth Rates Affected by Tensile Residual Stresses for Ti-6Al-4V β-STOA (LS)

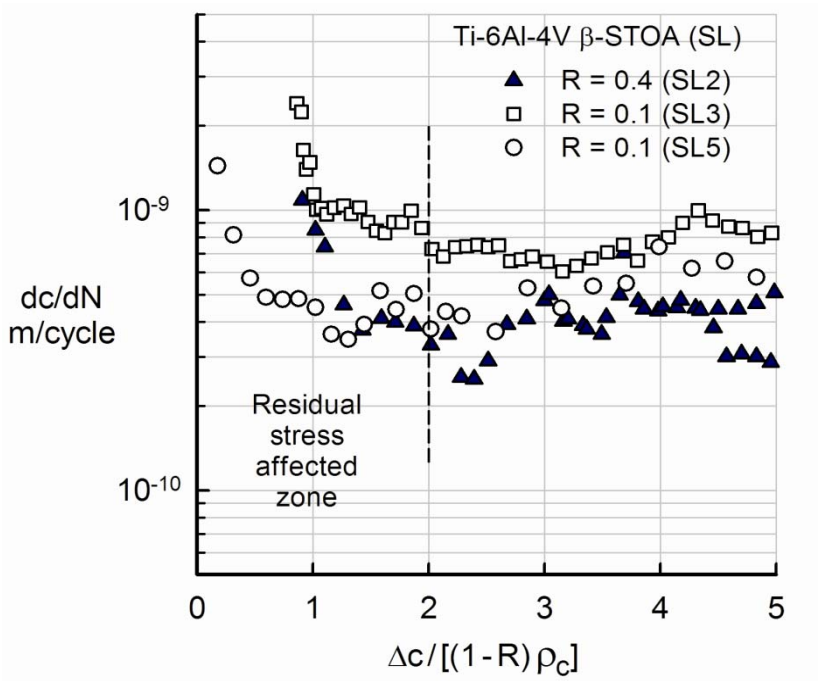

Figure 39. Crack Growth Rates Affected by Tensile Residual Stresses for Ti-6Al-4V β-STOA (SL)

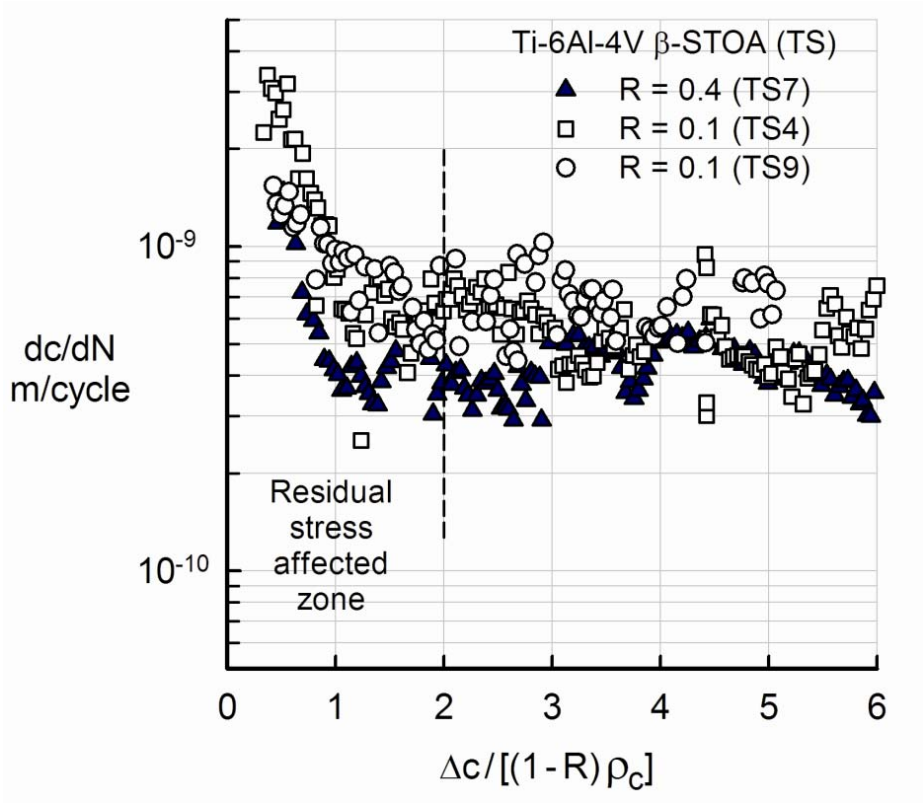

Figure 40. Crack Growth Rates Affected by Tensile Residual Stresses for Ti-6Al-4V β-STOA (TS)

5.2.5 Comparison of Stress Ratio Data.

Testing the three orientations on the titanium alloy showed if grain orientation had a significant effect on crack growth rates. Figures 41 and 42 show comparisons at high and low stress ratios, respectively. At high R, two orientations (LS and TS) agreed well in a tight band over a wide range in rates, except the TS orientation showed significantly lower rates in the near-threshold regime and a higher threshold. Only near-threshold data was generated on the SL orientation. In figure 42, the low-R data for the three orientations exhibited more scatter, but agreed fairly well over the complete range from threshold to near fracture.

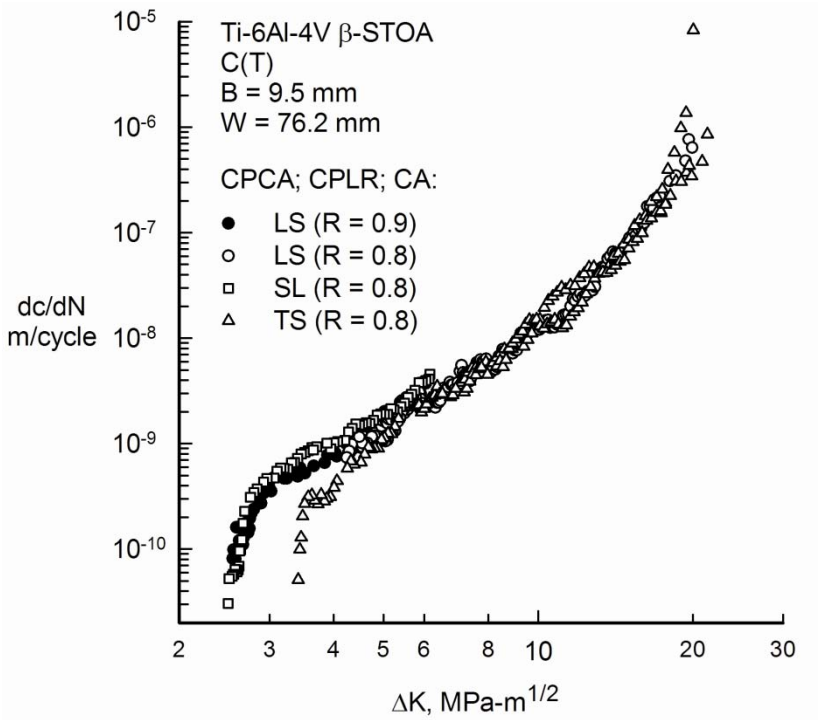

Figure 41. Comparison of Ti-6Al-4V β-STOA Data at High Stress Ratio

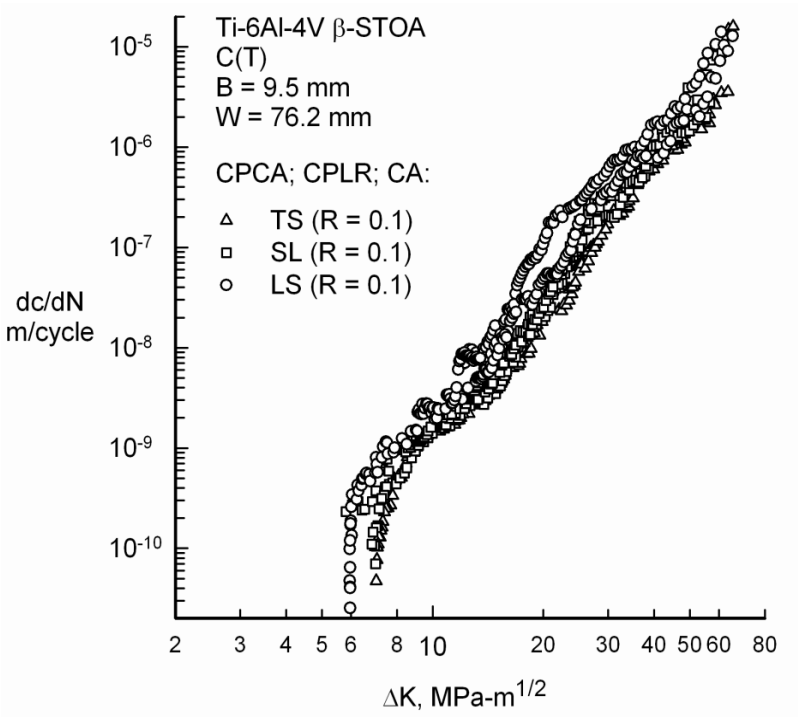

Figure 42. Comparison of Ti-6Al-4V β-STOA Data at Low Stress Ratio

5.2.6 Crack Closure Analyses.

Crack closure analyses were made on each titanium orientation to correlate the crack growth rate data into a narrow band over a wide range in stress ratios and rates from threshold to near fracture. For each orientation, an analysis was conducted to indirectly determine the crack-opening load (P_o/P_{max}) ratio for each R ratio tested. Because the titanium alloy data showed some differences at high R, a trial-and-error procedure was used to determine the crack-opening load ratios. Thus, the results for R = 0.7 were also allowed to shift, but the R = 0.8 and 0.9 data were not allowed to shift (U = 1 for these tests). These results are shown in figure 43, which shows P_o/P_{max} against R. Using the crack-opening stress (or load) equations in reference 54, a value of the constraint factor (α) was selected to best fit the data for each orientation. Surprisingly, the constraint factors were quite low compared to previous data correlations on a wide range of materials. The constraint factors ranged from 1.0 (plane stress) for the SL orientation to 1.5 for the LS orientation. It had been generally suspected that the constraint factors were accounting for plasticity-, roughness- and fretting debris-induced crack closure mechanisms in using α as a fitting parameter.

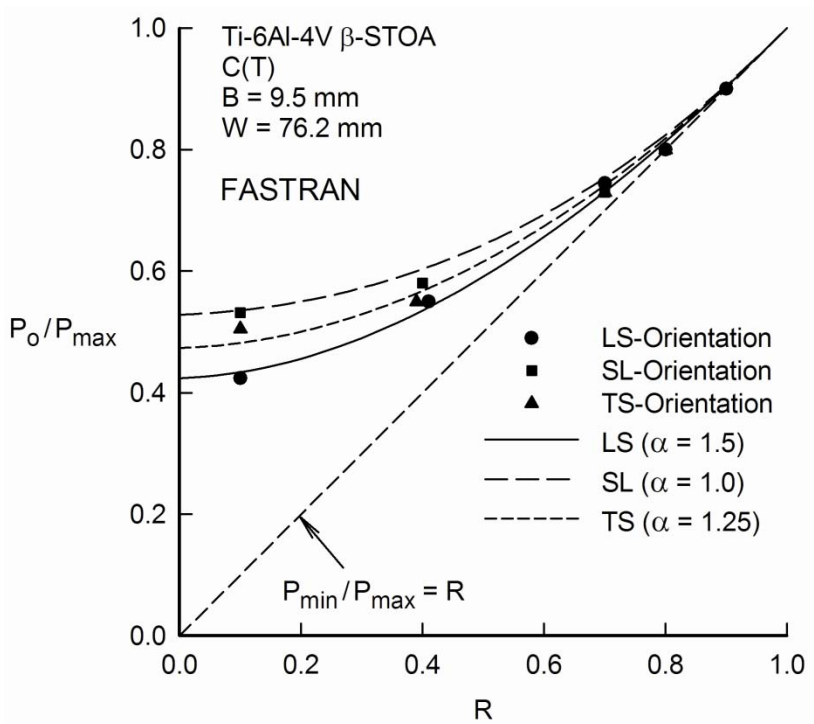

Figure 43. Indirect Determination of Crack-Opening Loads and Constraint Factors for Ti-6Al-4V β-STOA

Using the respective constraint factors, figures 44 to 46 show the effective stress-intensity factor range (ΔK_{eff}) against rate correlations for the LS, SL, and TS orientations, respectively. The LS orientation showed more scatter than the SL and TS orientations. The TS orientation showed the best correlation. It could not be determined whether these differences were due to possible residual stresses from the forging block or to the tortuous crack profiles in measuring crack lengths.

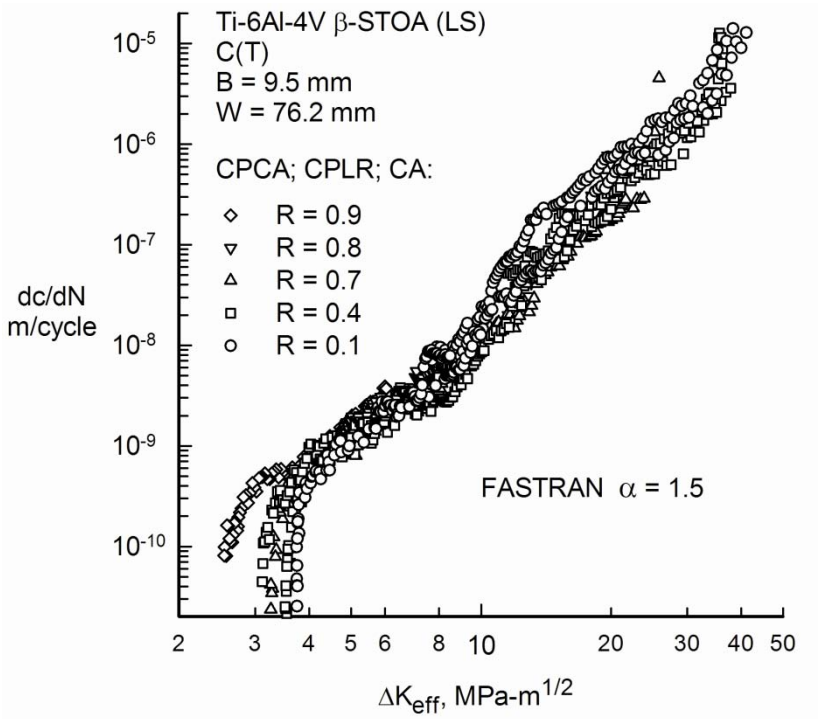

Figure 44. Effective Stress-Intensity Factor Range Against Rates for Ti-6Al-4V β-STOA (LS)

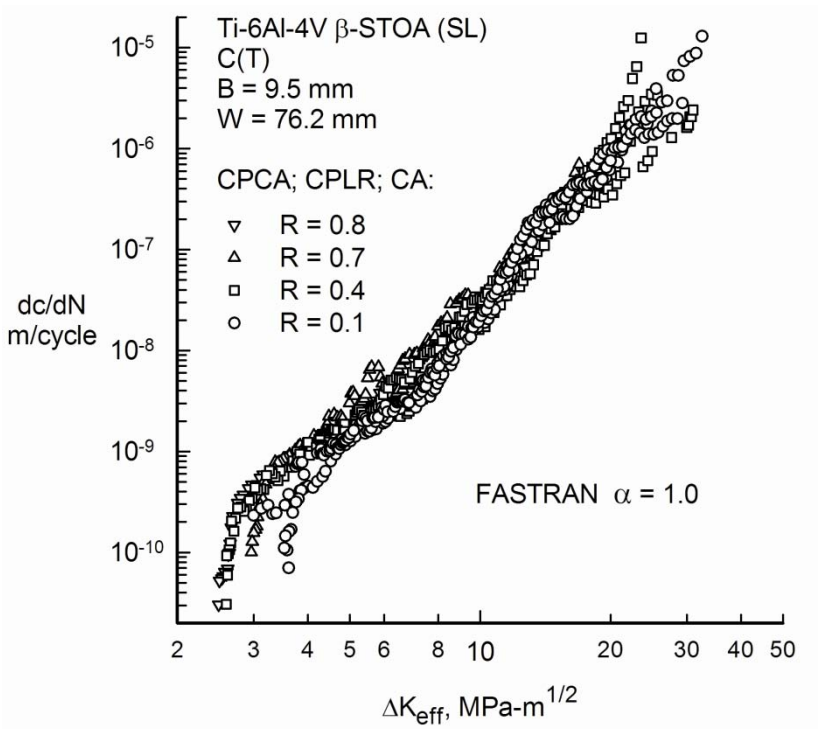

Figure 45. Effective Stress-Intensity Factor Range Against Rates for Ti-6Al-4V β-STOA (SL)

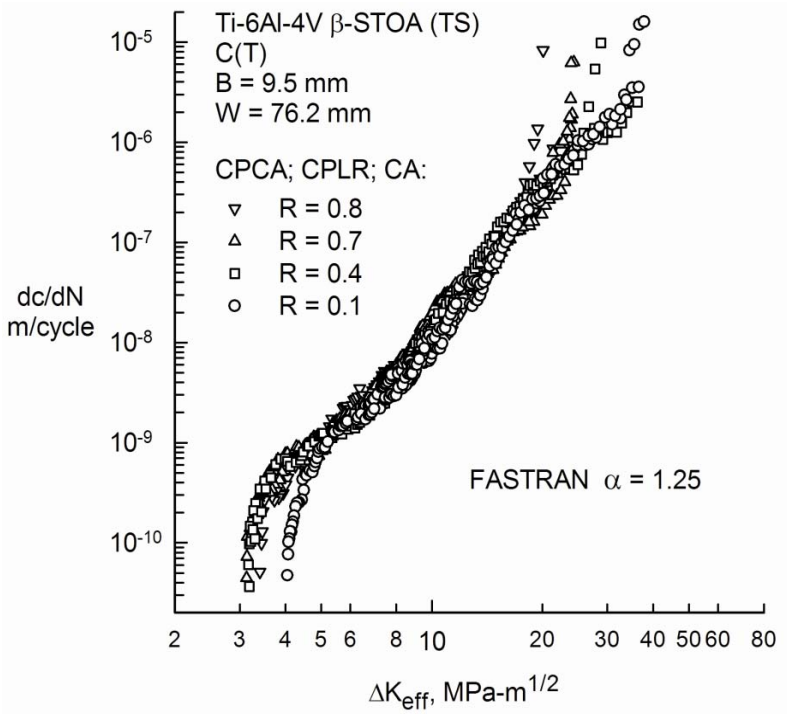

Figure 46. Effective Stress-Intensity Factor Range Against Rates for Ti-6Al-4V β-STOA (TS)

Additional analyses on a similar β-STOA titanium alloy tested at NASA LaRC will be presented in section 6.2.

5.3 STEEL 4340.

Thirty C(T) specimens (W = 50.8 mm) were provided to MSU by Boeing Rotorcraft Systems. All specimens were tested in the LT orientation (crack plane perpendicular to the rolling direction). The specimens were renotched by electrical discharge machining (EDM) to produce a 45-degree V-notch that had a very small notch-root radius (~0.08-mm). Fatigue crack growth tests were conducted over a wide range in stress ratios ($0.1 \leq R \leq 0.95$). The three threshold test methods were only used for the low-R test conditions. Only the CPCA or CPLR test procedures were used for R >0.4.

5.3.1 Fatigue Crack Growth Tests.

To conduct an ASTM LR test, a crack has to be initiated at the V-notch in such a manner that the crack growth rate is equal to or less than 1E-08 mm/cycle. CA loading was selected to match these conditions, but the crack would not initiate at the notch. Thus, higher loading had to be determined by trial-and-error to produce a crack. An example is shown in figure 47 for R = 0.4. At a given CA loading, the crack began to grow away from the V-notch, these data are shown as the solid symbols. Once the crack growth rates matched the CA data, an LR test was conducted (open circles). The open symbols show test data for CA and LR loading well away from the V-notch. The solid curve represents the predicted results under CA loading. This behavior was not expected. In the aluminum and titanium alloys, the crack growth rates for cracks emanating from the V-notch start at high rates and rapidly drop and merge with the constant-R curve as the

crack grows away from the notch. (Note that these tests are CA loading and that the specimens have not been compression precracked.)

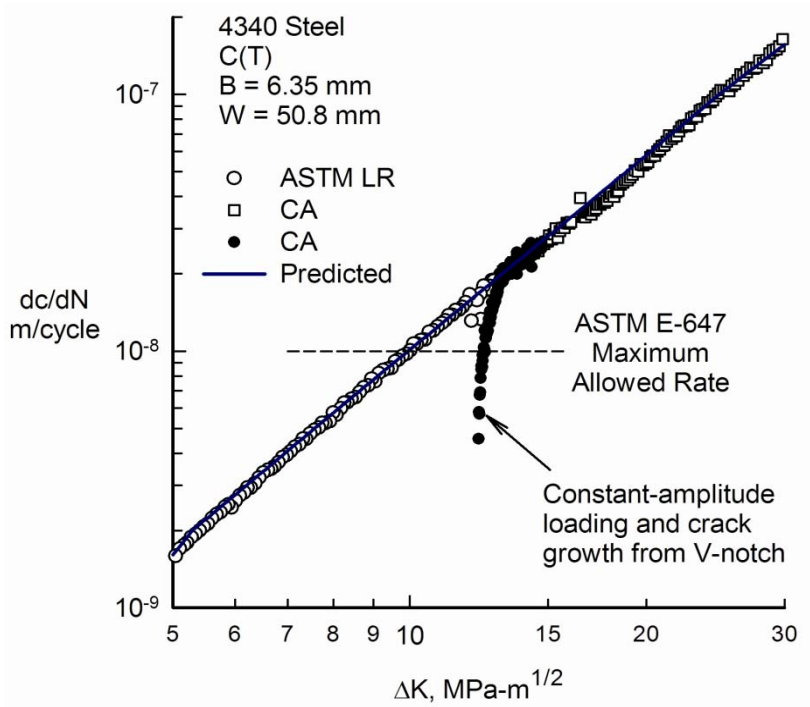

Figure 47. Crack Growth at V-Notch Affected by Possible Residual Stresses or Recast Zone From Machining Notch

Several possible reasons for this behavior include the V-notch influence on stress-intensity factors, residual stresses, and/or a recast zone of annealed material from EDM of the notch. For the notch-affected data, a local ΔK was calculated to force each data point to agree with the open symbols (at the same rate); these results are shown in figure 48. This plot shows the ratio of ΔK_{local} to the applied ΔK from only remote loading against crack extension (Δc) from the V-notch. The test at R = 0.4 and another test at R = 0.1 produced essentially the same results, which indicated that the affected zone extended about 1.3 mm from the notch. Crack growth beyond about 1.3 mm produced the same results as CA (notch unaffected) data. Because of the 45-degree notch, the influence of the stress-intensity factor solution was quite small, as indicated by the solid curve. Thus, it is expected that the notch produced by the EDM process induced either a compressive residual-stress field or a recast zone of annealed material around the V-notch.

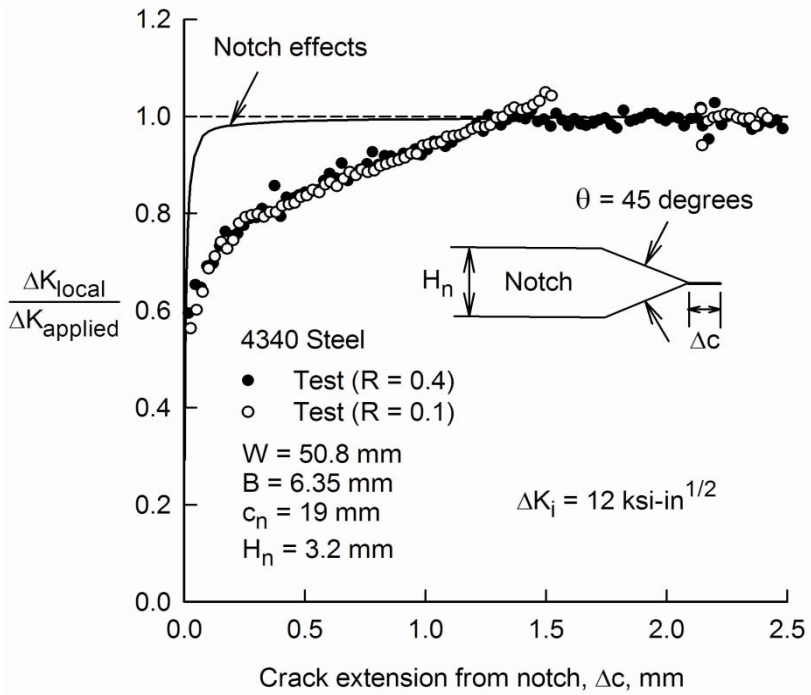

Figure 48. Ratio of Local and Applied Stress-Intensity Factors Over V-Notch-Affected Region

The issue of either compressive residual stresses or a recast zone at the V-notch, supposedly due to the EDM notch, caused difficulties in both ASTM LR and CPCA/CPLR tests. Several methods were considered to remove the affected zone. Basically, the crack must be extended beyond the affected region before unaffected crack growth rate data can be obtained. However, it was decided to use CP to try to eliminate the residual stresses and to grow the crack from the V-notch. Figure 49 shows several examples of crack growth during CP. The horizontal line at 1.3 mm shows the estimated extent of the affected region. The open symbols show the results of two tests using compression stress-intensity factor K_{cp} = -50 MPa√m, which grew the crack about 0.35 mm after about 40,000 cycles. These cracks were very straight, emanating from the V-notch. A higher compressive level on -76 MPa√m was use on another specimen, which grew the crack almost 1 mm from the notch. However, the crack was not straight, which may affect subsequent crack growth. Thus, variable compressive levels (-42, -50, and -85 MPa√m) were used to grow a crack from the V-notch that was very straight (solid-square symbols). But these crack extension values did not exceed the estimated limit on the affected zone. However, since the crack must be grown several compressive plastic-zone sizes from the V-notch, the crack length where crack growth data is valid was beyond the 1.3-mm limit.

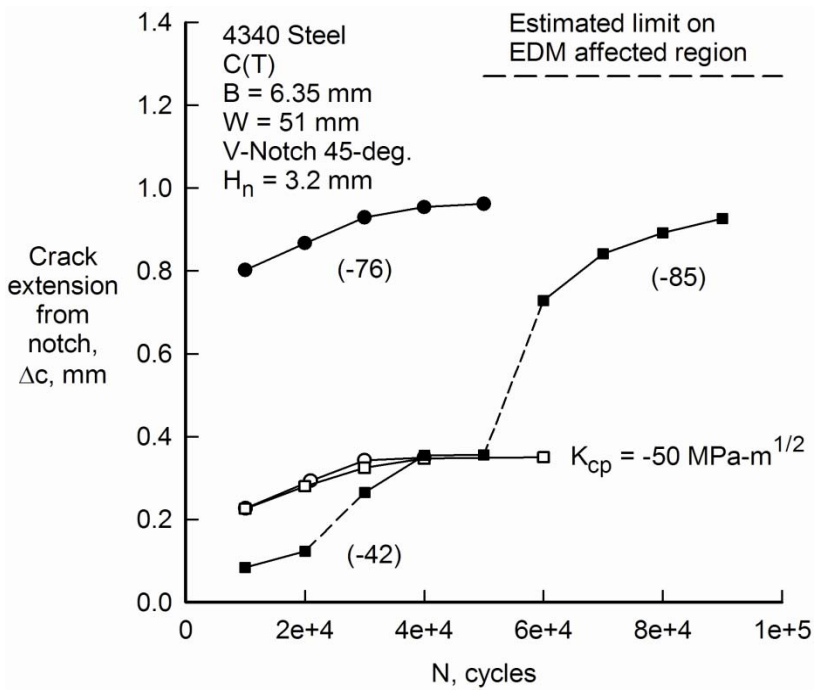

Figure 49. Crack Extension Under Compressive Loading for 4340 Steel C(T) Specimens

An expanded view of the test results for the R = 0.1 conditions are shown in figure 50. Three ASTM LR tests were conducted, but only two went down to near-threshold rates. The first test (S106) had reached near-threshold conditions with a large crack length and the results were sporadic. A second test (S008) reached near-threshold conditions at a smaller crack length than the previous test and the test was well controlled. Cracks in the three CPLR tests began to grow at high rates (near the high-R curve) because the cracks were fully open after CP. The crack growth rates rapidly dropped and approached the steady-state curve after a small amount of crack growth. (Note that the CP overcame the EDM notch effects by growing a crack nearly 2/3 of the affected zone and produced a tensile residual-stress field that allowed the crack to grow at a very low stress-intensity factor range.) After the crack had grown several compressive plastic-zone sizes, a LR test was conducted. The CPLR test produced slightly lower threshold behavior and faster crack growth rates than the ASTM LR tests. However, the differences were not considered significant. One advantage of the CPLR test method is that the LR process was initiated at 8E-10 m/cycle instead of the standard 1E-08 m/cycle.

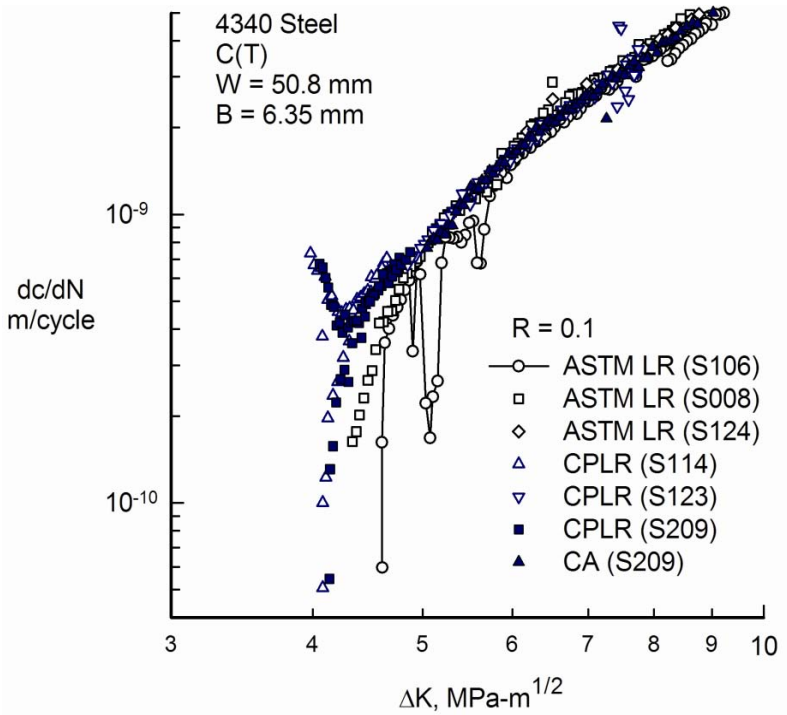

Figure 50. Fatigue Crack Growth During ASTM LR and CPLR Tests on 4340 Steel at R = 0.1

Some typical threshold tests conducted at R = 0.4 are shown in figure 51. Here, a CPCA and an ASTM LR test are compared. After CP loading, a CA loading was selected that had a ΔK level below the estimate threshold (ΔK_{th}). As the crack growth rate slowed down, the load levels were slowly increased, until it was decided to hold the load constant to complete the test. The solid symbols show the CA test data. The diamond symbol shows the location where the crack extension criterion was met. This was one of the first cases where the CPCA test results produced data at slightly higher ΔK levels than the ASTM LR test. It is suspected that the large number of cycles applied before threshold conditions were achieved contributed to a build-up of fretting debris along the crack surfaces and caused slightly higher crack-opening loads.

Figures 52 to 54 show all the results at R = 0.1, 0.4, and 0.7, respectively, using CPCA, CPLR, and CA test procedures. For reference, a single K_{max} equal constant test result is shown as the solid curve. (Note that figure 54 has a different ΔK-axis scale than figures 52 and 53.)

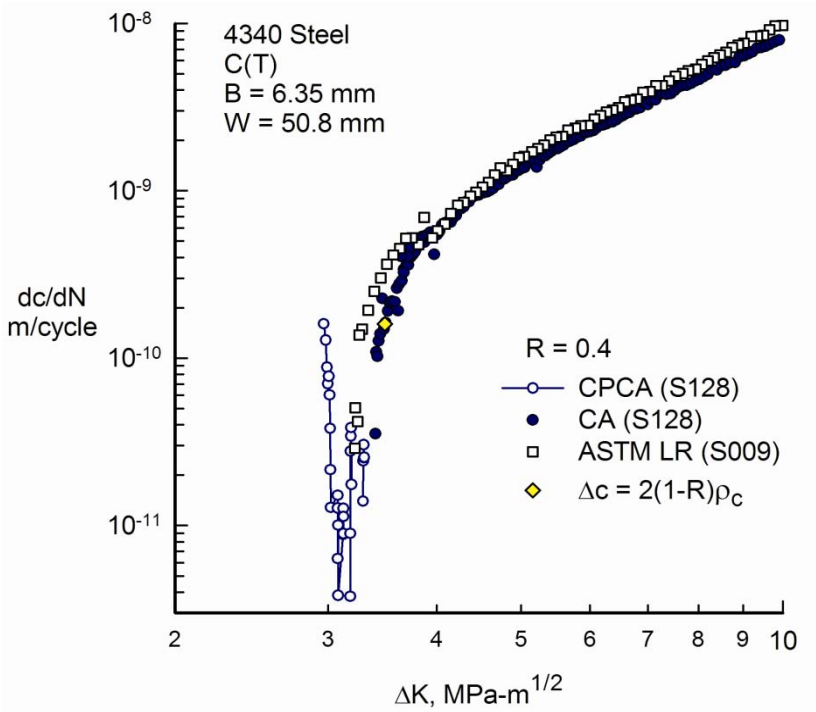

Figure 51. Fatigue Crack Growth During ASTM LR and CPCA Tests on 4340 Steel at R = 0.4

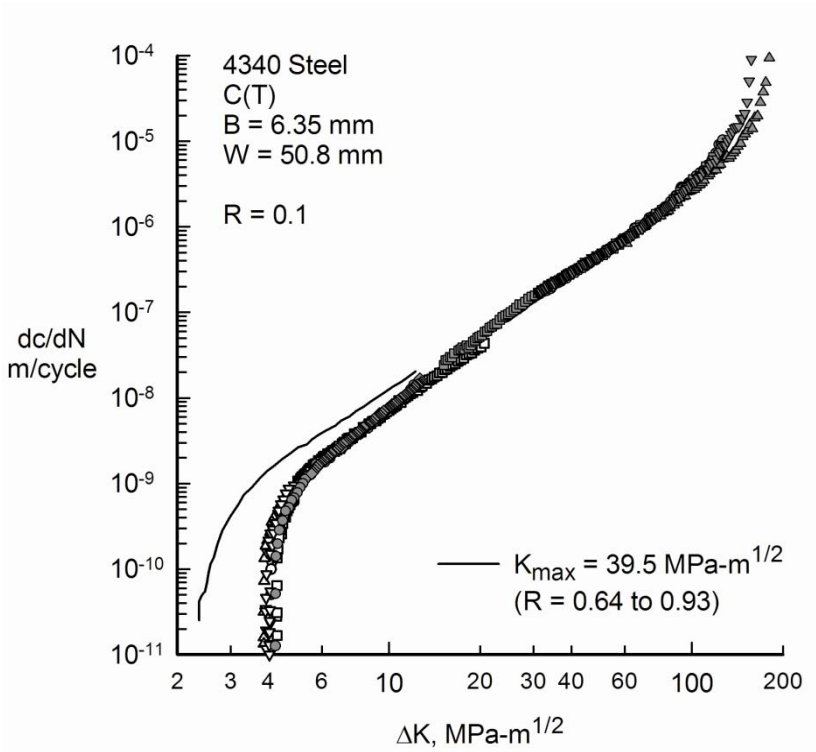

Figure 52. Fatigue Crack Growth Data on 4340 Steel at R = 0.1

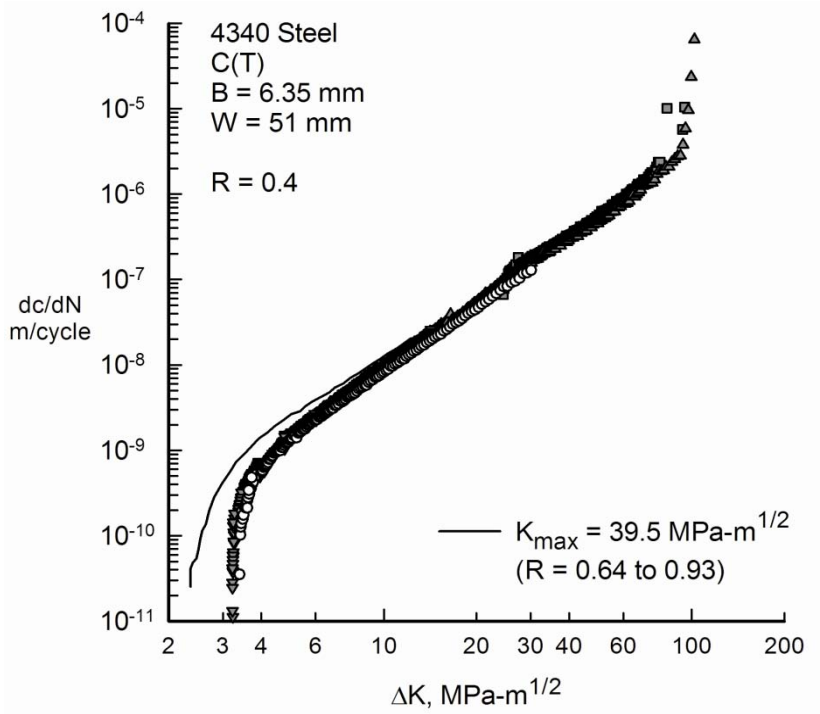

Figure 53. Fatigue Crack Growth Data on 4340 Steel at R = 0.4

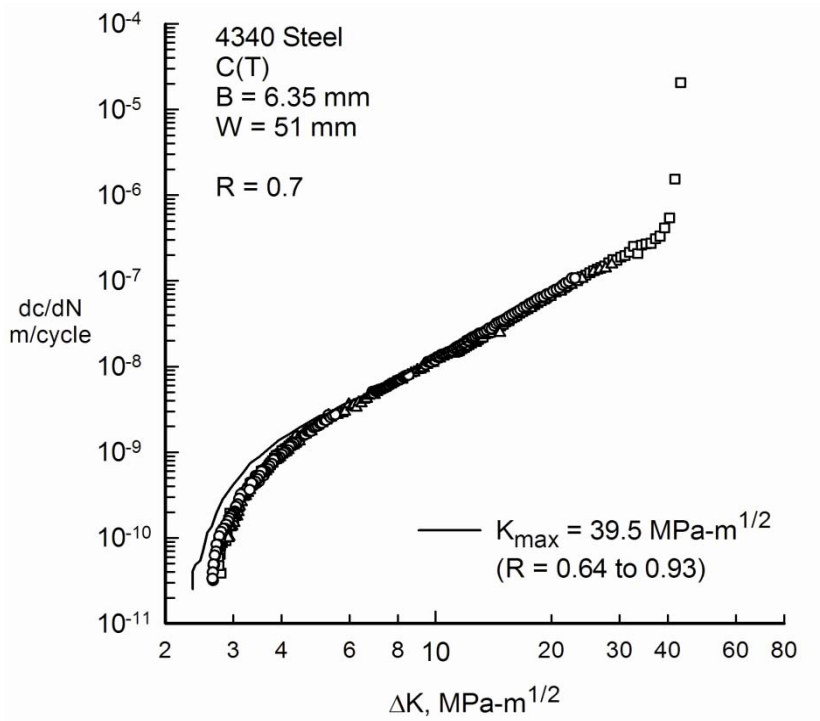

Figure 54. Fatigue Crack Growth Data on 4340 Steel at R = 0.7

A summary of all test data generated on the 4340 steel using CPCA, CPLR, and CA procedures is shown in figure 55. Again, the plot shows the typical stress ratio shift in the ΔK-rate data, but in the midregion (1E-08 to 1E-06 m/cycle) the shift is quite small. However, in the threshold and near-threshold regimes, the data exhibits a large amount of fanning with stress ratio. Also, in the threshold regime, the high stress ratio data continues to shift to lower ΔK values with increasing R. At higher rates approaching fracture, as usual, higher stress ratio tests exhibited failure at lower values of ΔK.

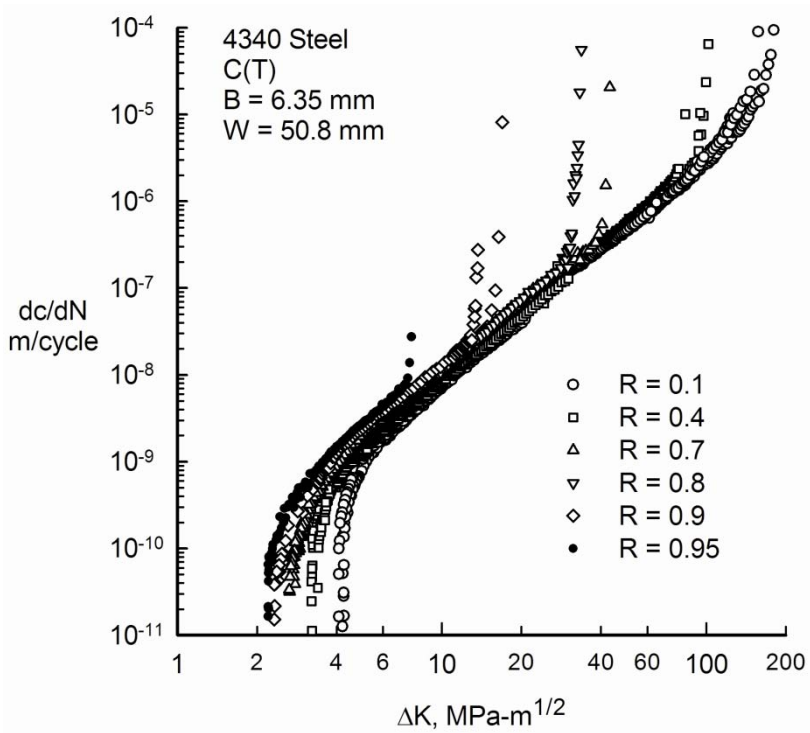

Figure 55. Fatigue Crack Growth Data Over a Wide Range in Stress Ratios and Rates for 4340 Steel

An expanded view of the crack growth rate data in the near-threshold regime is shown in figure 56. In addition, a single K_{max} equal constant test is also shown for comparison. These data show more fanning with stress ratio in the near-threshold regime than in the midregion. In the midregion (~1E-08 m/cycle), the test data shows the usual variation with stress ratio. The high-R test data (0.7 and 0.9) agreed fairly well, but the R = 0.95 test results went to failure.

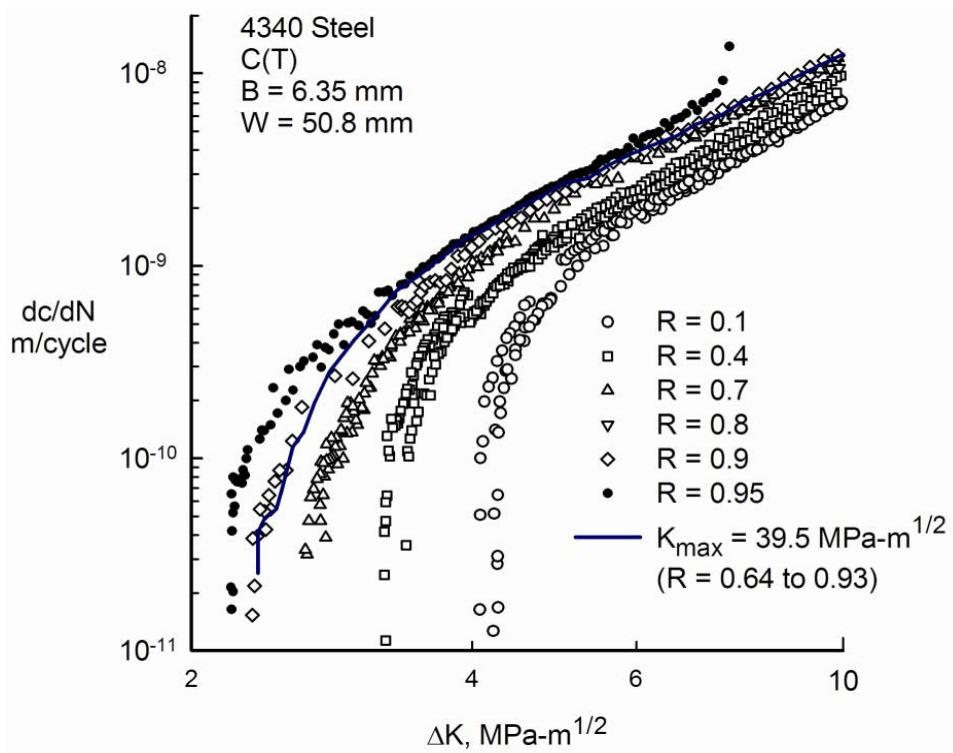

Figure 56. Expanded View of Fatigue Crack Growth Rate Data in Near-Threshold Regime

5.3.2 Crack Closure Analyses.

A crack closure analysis of the fatigue crack growth rate data on the 4340 steel was made to correlate the data into a narrow band over a wide range in stress ratios and rates from the threshold regime to near fracture. From previous crack closure analyses of high-strength 4340 steel, the constraint factor selected was 2.5 (nearly plane-strain conditions) and the ΔK_{eff}-rate results are shown in figure 57. In the midregion (above 1E-09 m/cycle), the data correlated fairly well. Deviations shown at high rates are caused by cracks growing to failure. In the threshold and near-threshold regimes, the test data fanned with stress ratio. The solid curve with open symbols shows the selected ΔK_{eff}-rate baseline curve, which is the leading power-law term in equation 6 (see table 8). The selection of the baseline curve in the midregion is a best fit to the test data, but trial-and-error procedures are used in both the threshold and fracture regions.

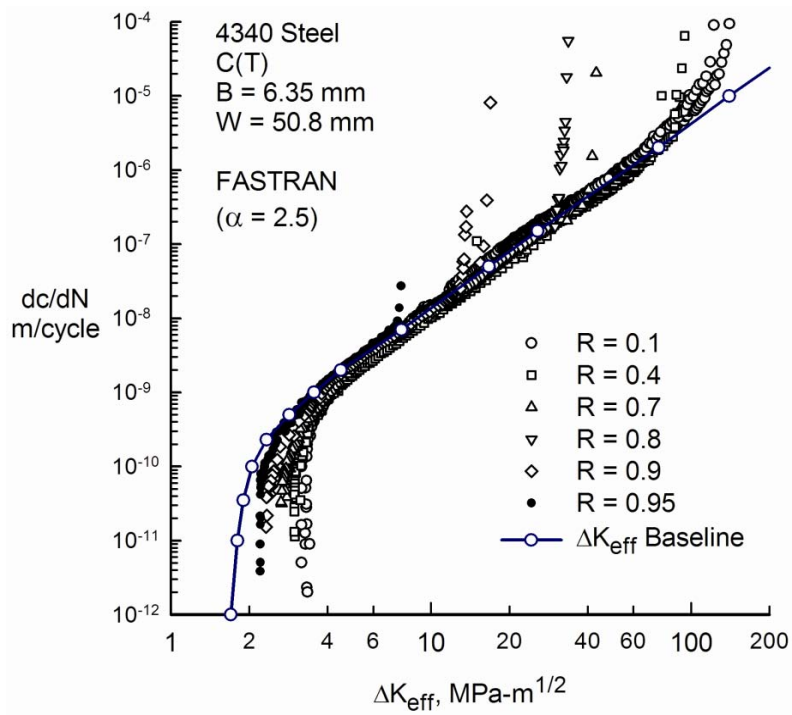

Figure 57. Effective Stress-Intensity Factor Range Against Rates for 4340 Steel

Table 8. Effective Stress-Intensity Factor Range Against Rate Relation for 4340 Steel (B = 6.35 mm)

ΔK_{eff}, MPa√m	dc/dN, m/cycle	ΔK_{eff}, MPa√m	dc/dN, m/cycle
1.70	1.0e-12	16.7	5.0e-08
1.80	1.0e-11	25.7	1.5e-07
1.90	3.5e-11	75.0	2.0e-06
2.05	1.0e-10	140.0	1.0e-05
2.33	2.3e-10	360.0	1.0e-04
2.85	5.0e-10	α = 2.50	All rates
3.55	1.0e-09	C_3 = 3.25 MPa√m	C_4 = 0.14
4.50	2.0e-09	p = 5	—
7.70	7.0e-09	C_5 = 165 MPa√m	q = 8

The coefficients in the threshold term, $[1 - (\Delta K_o/\Delta K_{eff})^p]$, of equation 6 were evaluated by first determining the effective stress-intensity factor range threshold, ΔK_o, as a function of R from the results shown in figure 57. The ΔK_o value for a given R is the limiting asymptotic value as the rate goes to zero and is not defined at a rate of 1E-10 m/cycle as specified in ASTM E 647. These results are plotted in figure 58. Again, the functional form selected is a power-law

equation, like that proposed by Klesnil and Lukas [56], except the effective stress-intensity factor range is used instead of linear-elastic values. A fit to the threshold data on the steel is shown by the solid curve. The power-law term, p = 5, was selected to best match the shape of the ΔK-rate curves as threshold conditions were approached.

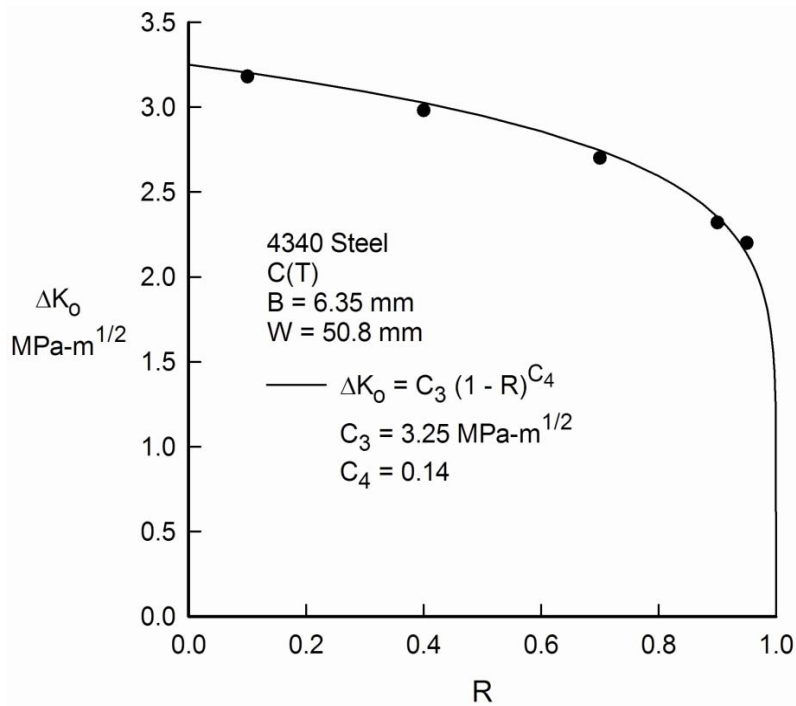

Figure 58. Effective Stress-Intensity Factor Range Thresholds for 4340 Steel

To evaluate the coefficients in the fracture term, $[1 - (K_{max}/C_5)^q]$, in equation 6, the cyclic fracture toughness (C_5) must be determined. Normally, C_5 is equal to the elastic fracture toughness, K_{Ie}, which is usually a function of crack length, width, and crack configuration. K_{Ie} is the elastic stress-intensity factor at failure using the initial crack length and maximum-failure load. But linear-elastic fracture mechanics parameters, such as K, do not work very well for fracture. Nonlinear fracture mechanics concepts, such as J or CTOD, are required to correlate and predict the effects of crack length, width, and crack configuration on fracture. However, the TPFC [57 and 58] has been able to correlate and predict the effects of crack length, width and, in some cases, crack configuration on fracture.

To use the TPFC, the tensile properties of the materials are required. Unfortunately, the tensile properties were not determined. From Boeing, the stated tensile strength was about 1100 MPa. This was confirmed by hardness tests conducted on some specimens. In most of the fatigue crack growth tests, the cracks in the C(T) specimens were grown to failure under cyclic loading. Here, the final recorded crack length and the maximum fatigue load were used to calculate K_{Ie}, and these results are shown in figure 59 as open symbols. Most tests failed at rather large c_i/W ratios (>0.7). But one specimen was fatigue cracked to a lower crack length-to-width ratio and statically pulled to failure (solid symbol), which agreed very well with the one specimen that had been cycled to failure at a high load. The dashed curves in figure 59 show limit-load calculations

using the stated tensile strength (1100 MPa) or a value (1500 MPa) selected to fit the extreme crack length-to-width ratio results. The solid curve shows the TPFC analysis using the 1500 MPa as the tensile strength, which fit the test data very well. However, the large crack length-to-width ratio results also correspond to small uncracked ligament-to-thickness ratios, $b/B = (W-c_i)/B$, as shown on the upper scale in figure 59. It is known that the in-plane and out-of-plane constraint increases as the ligament size becomes smaller. Thus, the deep-crack data may have a constraint elevation that is causing higher K_{Ie} values.

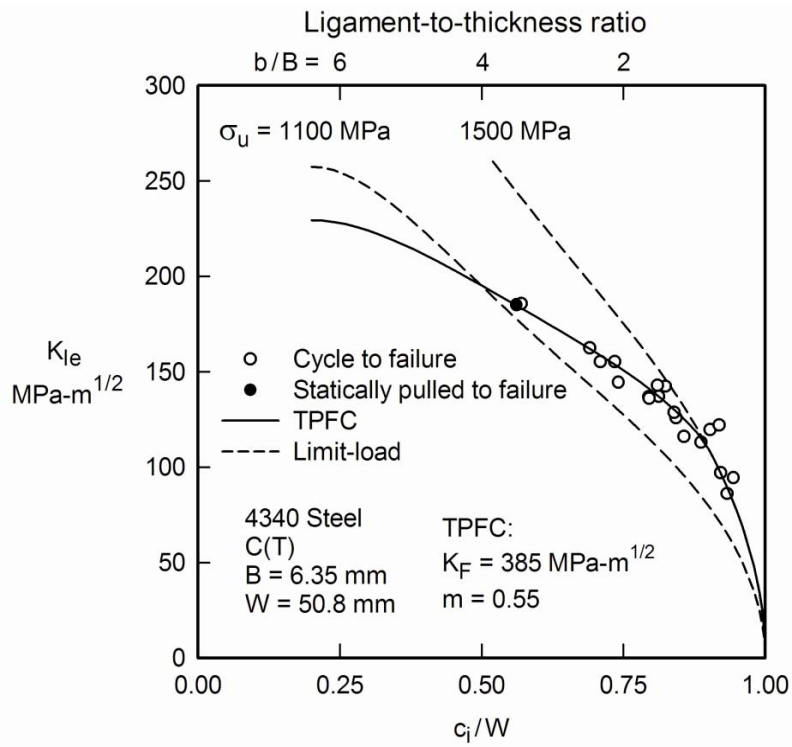

Figure 59. Elastic Stress-Intensity Factors at Failure and Limit-Load Analyses

Figure 60 shows how the elastic stress-intensity factor at failure may be influenced by C(T) specimen width. Using the K_F and m values determined to fit the fracture data in figure 59 with a constraint-elevated tensile strength (1500 MPa), the dashed curves show that larger-width specimens may have higher K_{Ie} values at failure, while smaller-width specimens may have lower K_{Ie} values at failure. For the test data generated on the 50.8-mm-wide specimens, the variations in K_{Ie} with crack length was very significant with values ranging from 180 MPa√m to as low as 80 MPa√m. But when using equation 6, C_5 was held constant at 165 MPa√m for simplicity. In practice, however, the variation in elastic fracture toughness should be accounted for in any fatigue crack growth and fracture analyses.

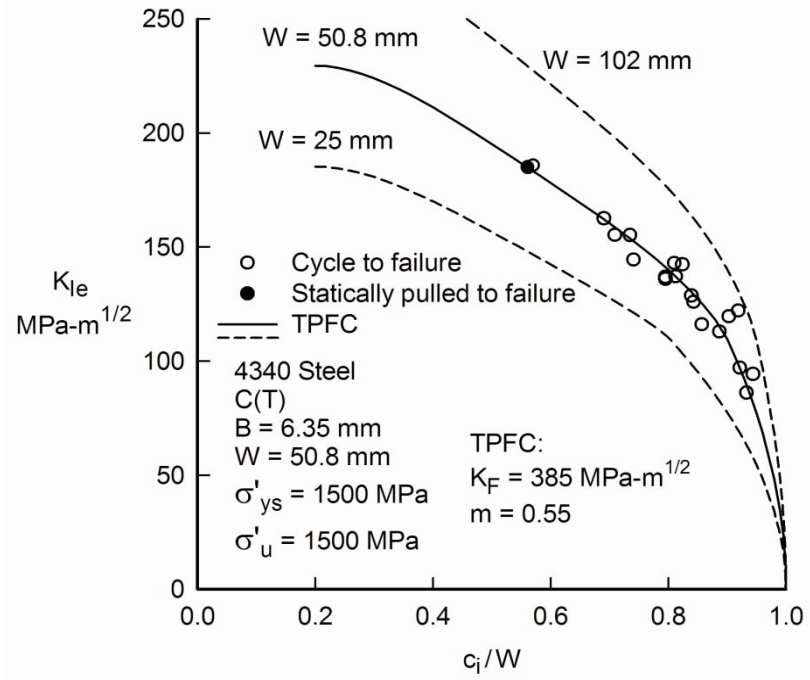

Figure 60. Elastic Stress-Intensity Factors at Failure and TPFC Analyses

Figures 61 to 63 show how well equation 6 can predict the wide-range fatigue crack growth rate data from low to high R, respectively. Figure 61 shows the R = 0.1 data from threshold to near fracture together with a single K_{max} equal constant test and the ΔK_{eff}-rate curve. The solid curve is the predicted results from equation 6 and the parameters are given in table 8. The p and q values in equation 6 were selected to match the shape of the data in either the threshold or fracture regimes, respectively. The ΔK_{eff}-rate curve matches the K_{max} test results very well above a rate of 1E-09 m/cycle.

The R = 0.4 results are shown in figure 62. Here the predicted curve fell to the upper side of the test data scatter band in the midregion. Thus, fatigue crack growth analyses under R = 0.4 loading predicted shorter lives than the tests. In the midregion, it was estimated that the predicted lives would be about 20% shorter that tests. But in the threshold and fracture regions, the predicted threshold and fracture was in very good agreement with the test results.

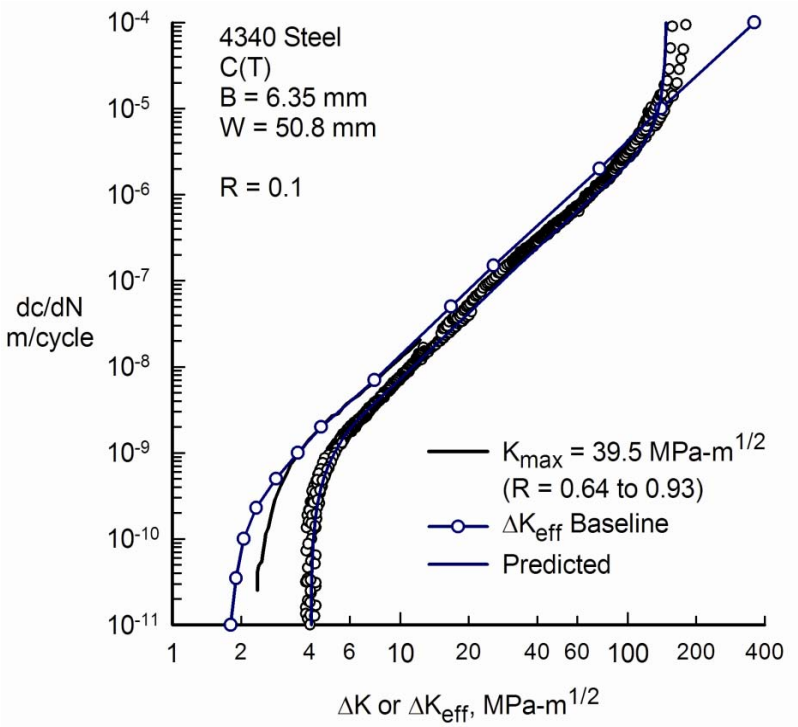

Figure 61. Measured and Predicted Crack Growth Rates on 4340 Steel at R = 0.1

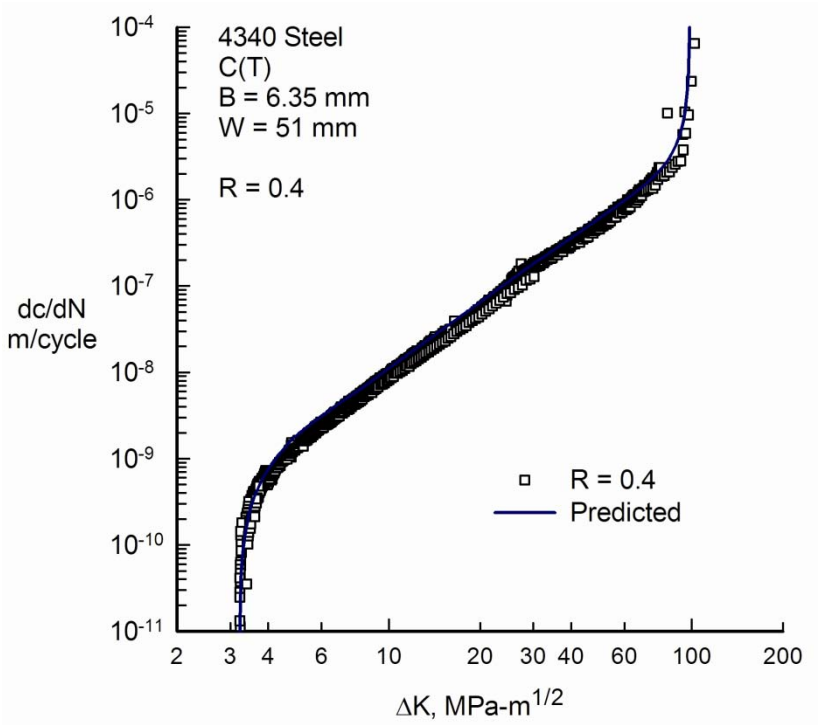

Figure 62. Measured and Predicted Crack Growth Rates on 4340 Steel at R = 0.4

Figure 63 shows the comparisons among predicted and measured results for the high-R cases (R = 0.7 to 0.95). All comparisons were considered very reasonable.

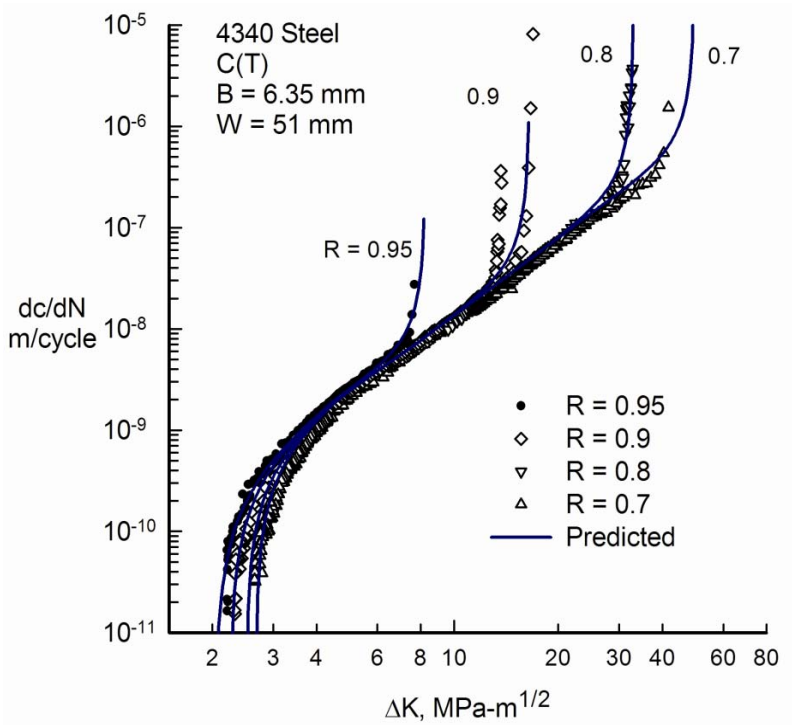

Figure 63. Measured and Predicted Crack Growth Rates on 4340 Steel at High R

6. MATERIALS TESTED AT NASA LaRC.

Four rotorcraft materials were tested at NASA LaRC using the ASTM LR test method. The materials were 7050 (-T7451) aluminum alloy, Ti-6Al-4V β-STOA titanium alloy, AZ91E magnesium alloy, and 4340 steel. A detailed report on the data generated on these materials is presented and discussed in reference 32. Some 7050 C(T) specimens and CPCA test data on 7050 and Mg AZ91E alloys were provided to MSU. The crack growth rate data were analyzed with a crack closure model to develop the ΔK_{eff}-rate curve for all materials except the 4340 steel. CPCA tests were reported on only one of the materials (7050), but a few CPCA tests were conducted on the Mg AZ91E alloy (not presented in reference 32).

6.1 ALUMINUM ALLOY 7050-T7451.

6.1.1 Fatigue Crack Growth Tests.

On the 7050 alloy, tests were conducted at NASA LaRC under K_{max} equal constant (three levels) and constant-R load reduction (three stress ratios). Figure 64 shows the ΔK against rate data for 50.8-mm-wide C(T) specimens. The results for the high-R ratio conditions and the K_{max} data agreed well in the midregion, but separated slightly in the threshold regime. The spread in crack growth rate data with the lower stress ratios was as expected. But the R = 0.1 results show some variations for different test specimens in the near-threshold regime. This may have been due to the influence of residual-stress variations in the forging material or from load-history effects, as

shown in figure 65. Four tests were conducted at R = 0.1 with 4 different initial ΔK_i values to start the LR tests. The data shown by the solid-circular symbols violated the ASTM LR standard (initial rate greater than 1E-08 m/cycle). The tests at the two lowest ΔK_i values satisfied the standard, but produced slightly lower thresholds than the tests with higher ΔK_i values.

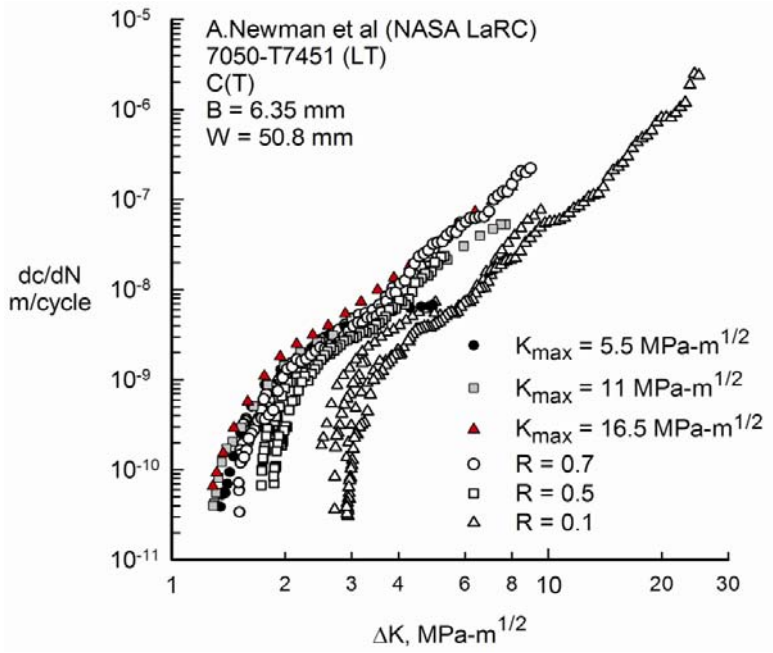

Figure 64. Crack Growth Data Over a Wide Range in Stress Ratios and K_{max} Test for 7050-T7451

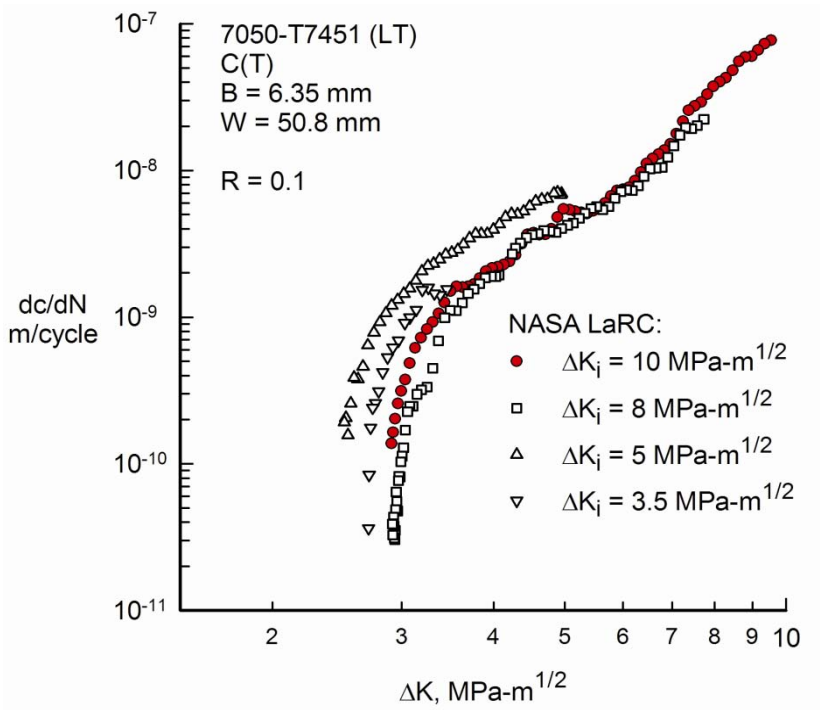

Figure 65. Crack Growth Data for R = 0.1 Test Conditions for 7050-T7451

Two CPCA tests were conducted on this alloy at R = 0.1. Both tests had nearly the same starting location and agreed very well; therefore, only one test is shown in figure 66 for clarity. The CPCA test results are shown as the solid curve. All of the R = 0.1 (ASTM LR) results are also shown for reference. The CPCA test results started on the high-R curve because the crack was fully open ($\Delta K = \Delta K_{eff}$), but as the cracks grew, the crack-opening load levels rose and the data approached the R = 0.1 data. The solid-diamond symbol shows where the crack extension in the CPCA tests had reached the $2(1 - R)\ \rho_c$ criterion, where ρ_c is the compressive plastic-zone size. It was expected that the influence of the CP tensile residual stresses would diminish and the crack-opening loads would stabilize [44]. Below a ΔK level of 3 MPa√m, there were indications of some major differences. The question remains whether the CPCA test data is still being affected by tensile residual stresses or is the data from the ASTM LR tests still being affected by load history, even at a very low starting ΔK_i level.

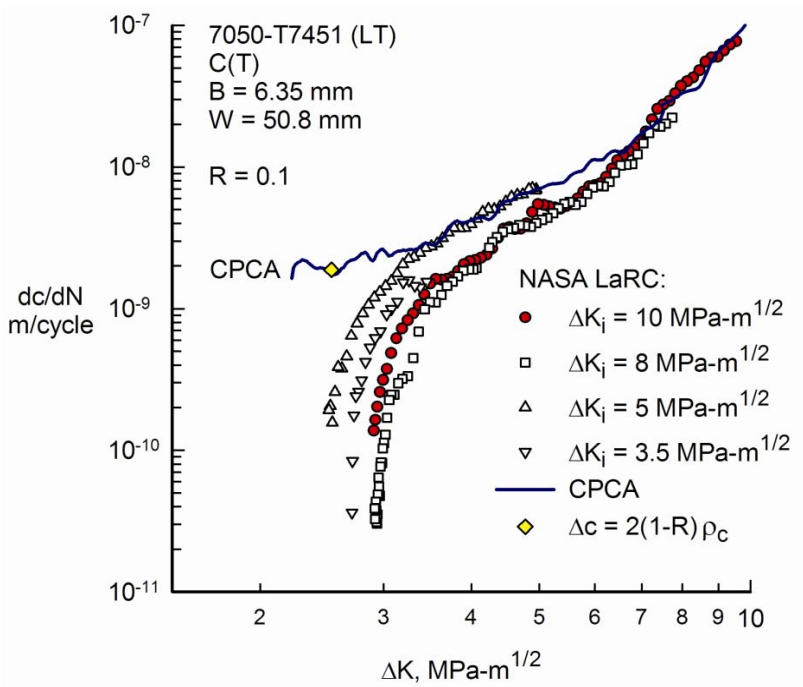

Figure 66. Crack Growth Data for R = 0.1, CPLR, and CPCA Test Conditions for 7050-T7451 (LT)

NASA LaRC gave MSU a number of 7050 alloy C(T) specimens that were machined from the same plate of material as those shown in figures 64 to 66. Thus, MSU tested two specimens at R = 0.1 using the CPLR test procedures. After CP loading, one test had a starting ΔK_i level at the lowest value from the LaRC tests. These results are shown as the solid-square symbols in figure 67. The double arrows show the CPLR tests and the subsequent CA test to generate the upper portion of the curve. These data fell at slightly lower ΔK values than the LaRC tests at the same rate. A second CPLR test had a ΔK_i level of 2.7 MPa√m and these results are shown as solid triangles. These results fell at even lower ΔK values than the previous CPLR test. The latter results confirm the CPCA test results from LaRC. It was very surprising that the very low ΔK_i levels would still have an effect on the near-threshold results.

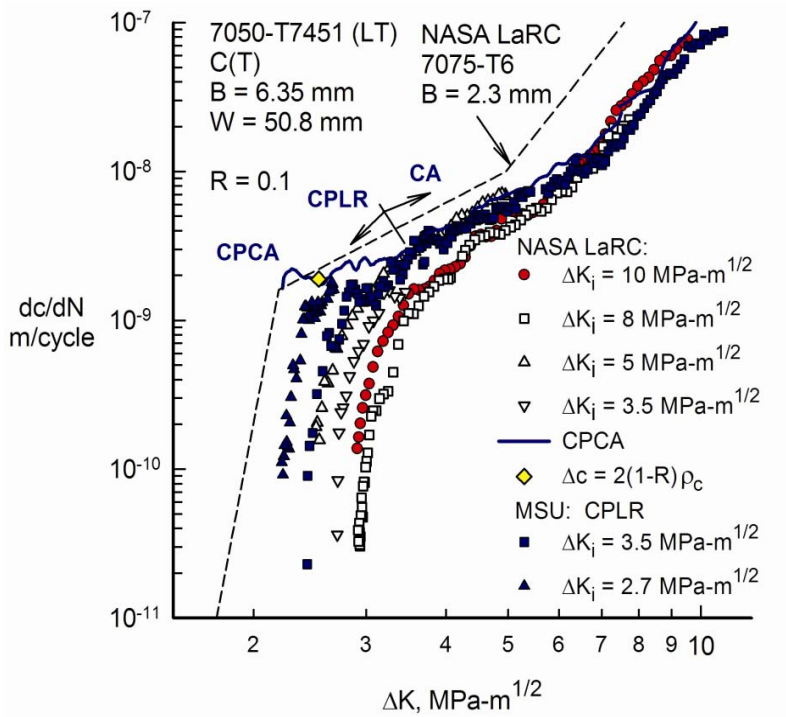

Figure 67. Crack Growth Data for R = 0.1 and CPLR Test Conditions for 7050-T7451

Crack closure measurements made on the R = 0.1 tests at MSU [59] indicated very high crack-opening levels in the threshold and near-threshold regimes, which may be due to both plasticity- and roughness-induced crack closure. The crack surface profiles in the 7050 alloy were very rough. It is also suspected that rough crack surfaces may activate more fretting debris due to contacting asperities. For comparison, the ΔK-rate curve from a thin-sheet 7075-T6 alloy tested at LaRC [53] is shown as the dashed curve in figure 67, which had a very similar shape as the data from the lowest CPLR and CPCA tests.

6.1.2 Crack Closure Analyses.

A crack closure analysis of only the constant-R data shown in figure 64 was made using the FASTRAN crack closure model [54 and 55]. The test data in the threshold and midrate regimes (rates lower than about 1E-8 m/cycle) neglected to establish the ΔK_{eff}-rate baseline curve because, as previously shown, these data can be affected by the LR test procedure. Surprisingly, a very low-constraint factor, $\alpha = 1.3$, was found to correlate the test data fairly well, as shown in figure 68. The solid curve with open-circular symbols shows the ΔK_{eff}-rate baseline curve (see table 9). The baseline curve below a rate of about 1E-08 m/cycle was obtained from reference 59 using crack-opening load measurements made on similar C(T) specimens at various stress ratios and K_{max} equal constant tests. These results also show the classic plateau that occurs on most aluminum alloys in the (1E-09 to 1E-08 m/cycle) rate regime.

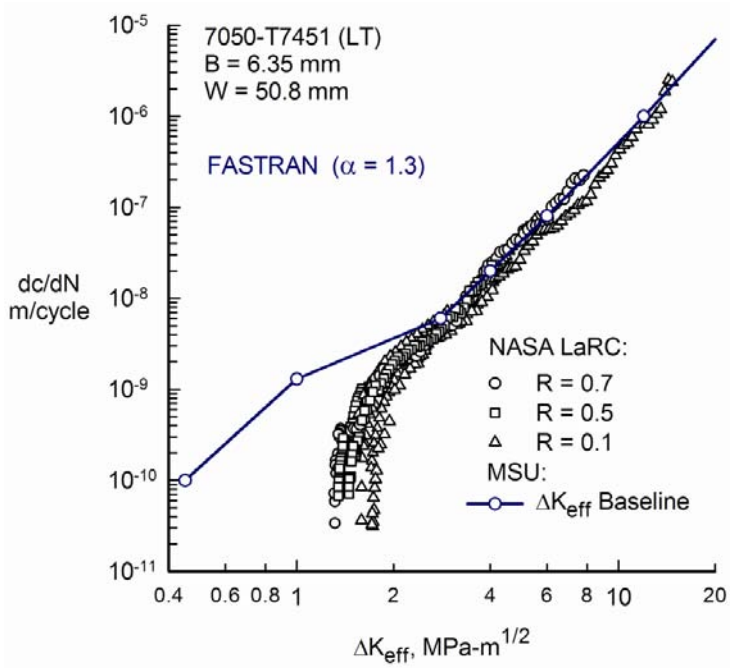

Figure 68. Effective Stress-Intensity Factor Range Against Rates for 7050-T7451 (LT)

Table 9. Effective Stress-Intensity Factor Range Against Rate Relation for 7050-T7451 (B = 6.35 mm)

ΔK_{eff}, MPa√m	dc/dN, m/cycle
0.45	1.0e-10
1.00	1.3e-09
2.80	6.0e-09
4.00	2.0e-08
6.00	8.0e-08
12.0	1.0e-06
22.0	1.0e-05
α = 1.3	All rates
C_3 = 1.3 MPa√m	C_4 = 0
p =5	—
C_5 = 40 MPa√m	q = 5

The coefficients in the threshold term, $[1 - (\Delta K_o/\Delta K_{eff})^p]$, of equation 6 were evaluated from test data presented in reference 59. The ΔK_o values as a function of R are shown in figure 69. The ΔK_o values were found to be nearly independent of R; thus, C_3 = 1.3 MPa√m and C_4 = 0. The power-law term, p = 5, was selected to best match the shape of the ΔK-rate curve from the previous CPLR test (R = 0.1) as the threshold conditions were approached.

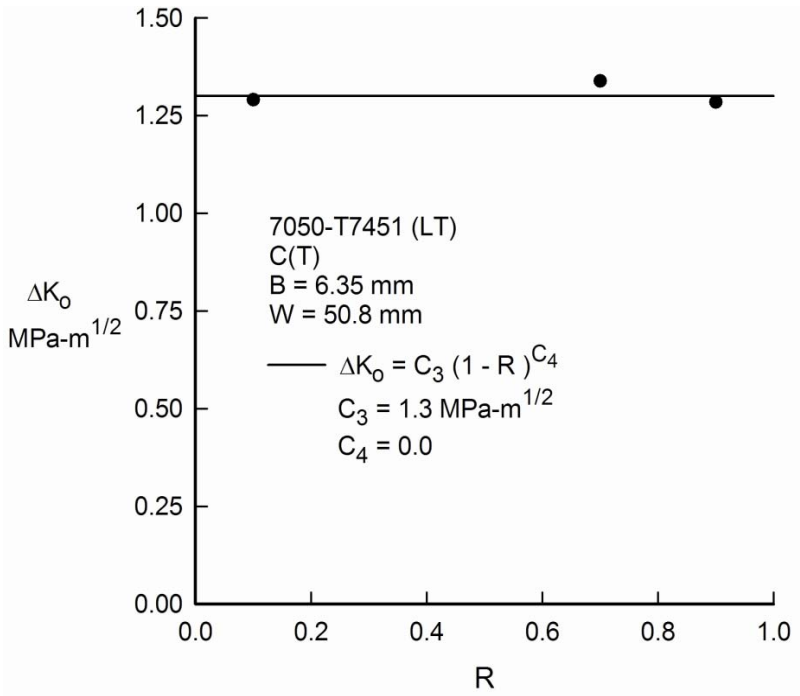

Figure 69. Effective Stress-Intensity Factor Range Thresholds for 7050-T7451 (LT)

Coefficients in the fracture term, $[1 - (K_{max}/C_5)^q]$, were also estimated from test results in reference 59. Several C(T) specimens made of the same material were cycled to failure at both low- and high R. From these results, the cyclic fracture toughness, C_5, was estimated at 40 MPa√m with q = 5. However, it is suspected that the K_{Ie} values are not constant, but vary with crack length and specimen width. However, insufficient test data was available to conduct a TPFC analysis.

A comparison of measured and predicted crack growth rate behavior from the crack closure model on the LaRC data at low- and high R is shown in figure 70. The solid lines with open-circular symbols show the ΔK_{eff}-rate baseline results, which were used to predict the various results at R equal to 0.1 and 0.7. The data shown by the solid-square symbols violated the ASTM LR test method, while the data shown by the open symbols satisfy the current ASTM standard. Above the knee in the ΔK_{eff}-rate curve (~6E-09 m/cycle), the predicted results agree well with the valid test data. But below the knee, the test results either produced a higher threshold and/or slower rates than the predicted results. These results indicate that further CPCA/CPLR tests need to be conducted at both low- and high-R test conditions.

Figure 71 shows all the ASTM valid LR test data and the CPCA/CPLR test data at R = 0.1. The lowest CPLR test and the LaRC CPCA test data fell quite close to the predicted curve in the threshold and near-threshold regimes, but some discrepancies occurred near 1E-08 m/cycle. As shown by the dashed curve, this location in rate is another transitional region for the aluminum alloys. In the upper region, rates greater than about 5E-08 m/cycle (not shown), the test data agreed well with the predicted curve.

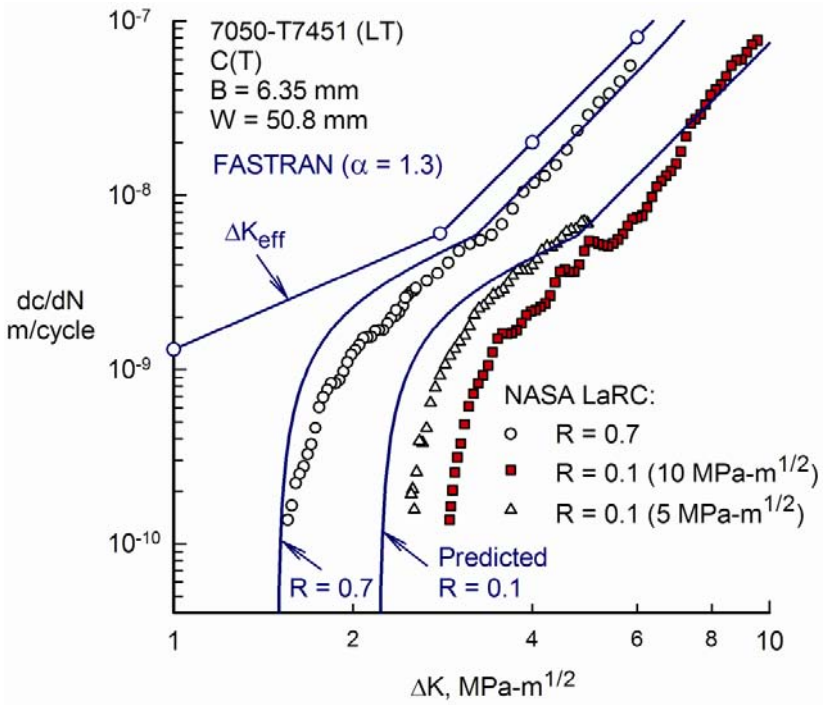

Figure 70. Measured and Predicted Crack Growth Rates on 7050-T7451 for R = 0.1 and 0.7

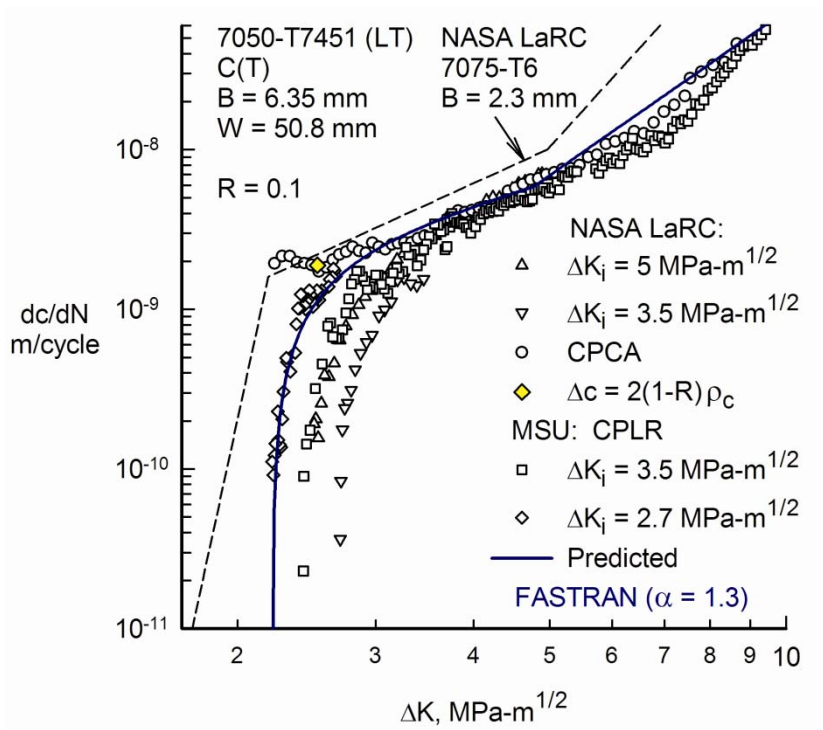

Figure 71. Measured and Predicted Crack Growth Rates on 7050-T7451 for R = 0.1

6.1.3 Validation of Crack Extension Criterion for 7050 Alloy.

James, et al. [43], conducted CPCK tests at R = 0.1 on the 7050 alloy C(T) specimens made of two thicknesses. The thicker material (B = 12.7 mm) was in the LT orientation and the specimen width was 76 mm; while the thinner material (B = 6.35 mm) was in the TL orientation and the specimen width was 50.8 mm. In conducting the CPCK tests, the compression loading was applied through the pinholes (see figure 7a) at compressive loads about twice as high as those proposed for the annex to ASTM E 647. Also, they had calculated the compressive stress-intensity factor, K_{cp}, using the standard C(T) specimen equation 4, which underestimates the stress-intensity factor for initial notch length-to-width (c_n/W) ratios less than 0.5 (see figure 8).

Figure 72 shows crack extension from the initial notch, Δc, plotted against cycles. Initially, the rates are affected by the tensile residual stresses caused by the compressive yielding at the starter notch. But once the effects of the residual stresses have decayed and the crack-opening load levels have stabilized, the rate of crack growth should be constant (ΔK = 3.3 MPa√m) at R = 0.1. The applied K_{cp} was 43.9 MPa√m and the compressive plastic-zone size, ρ_c, is shown by the dashed line. The lower arrow shows where the steady-state crack growth rate begins and the upper arrow shows where the crack extension criterion was met.

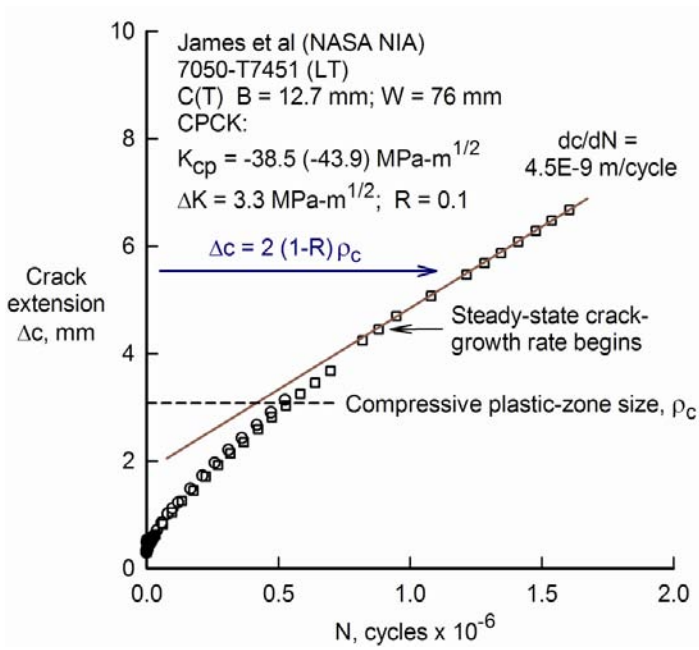

Figure 72. CPCK Test Results of 12.7-mm-Thick 7050-T7451 (LT)

Similar CPCK results on the thinner material are shown in figure 73. Here, the crack was grown about 4 compressive plastic-zone sizes under ΔK equal constant. However, beyond about 3 plastic-zone sizes, a slight drop in crack growth rate was observed. It is suspected that further crack growth may lead to an additional drop in rates and the development of a possible threshold, even under constant ΔK (if the ΔK level is slightly above threshold conditions). Note that the CPCK test method is basically a LR test method and premature contact of the fatigue surfaces is possible with further crack extension.

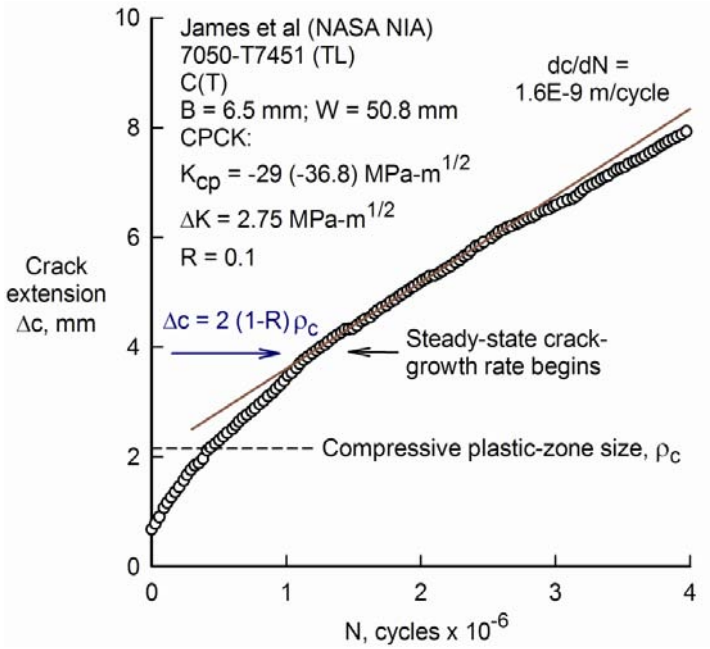

Figure 73. CPCK Test Results of 6.35-mm-Thick 7050-T7451 (TL)

The development of a threshold condition during CPCK testing on C(T) specimens made of a D6AC steel was demonstrated by Forth, et al. [60] (also see reference 61 for detailed explanations). Two CPCK tests (R = 0.1) were conducted on D6AC steel to study the influence of the tensile residual stresses caused by compressive yielding at the notch tip during CP. These tests were both subjected to CP loads and then to loading, which would maintain a constant ΔK range for the duration of the test. The two tests were conducted at ΔK levels of 4.4 and 7.7 MPa√m, respectively. The results showed that after crack extension values of about 2 ρ_c, the crack growth rate reached a constant value over about 2 mm of crack growth (or about 6 compressive plastic-zone sizes). This indicated that the influence of the tensile residual stresses was acting over about 2 ρ_c. For crack extension values greater than about 6 ρ_c, the crack began to slow down and essentially stopped in the lowest ΔK test. The crack tip had maintained the same ΔK, but as the applied loads were reduced, the crack surface displacements were also decreasing. The development of threshold conditions may be caused by remote closure or by an interaction with the laboratory air environment and build-up of oxide debris along the crack surfaces, which would promote higher closure loads and slower rates.

6.2 TITANIUM ALLOY Ti-6Al-4V β-STOA.

6.2.1 Fatigue Crack Growth Tests.

Tests were conducted at NASA LaRC under K_{max} equal constant (three levels) and constant-R load reduction (three stress ratios) on the β-STOA titanium alloy. The C(T) specimens were machined from a forging component supplied by Boeing Rotorcraft Systems, but the particular orientation was not specified. Figure 74 shows the ΔK against rate data for 76.2-mm-wide C(T) specimens. The results for the K_{max} tests exhibited a significant spread in the threshold regime. The question remains whether the spread was due to the so-called K_{max} effect or due to crack

closure. Because of the very rough and tortuous crack path in the β-STOA alloy, it is suspect that the spread is due to crack closure from roughness and not due to any K_{max} effects. But further study and local crack closure measurements are needed to adequately address this issue.

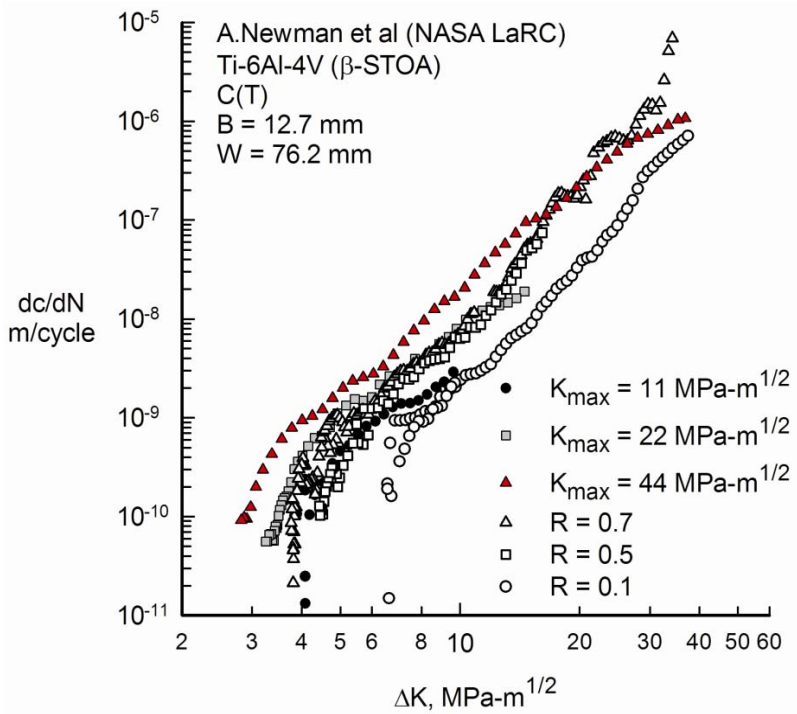

Figure 74. Fatigue Crack Growth Data Over a Wide Range in Stress Ratios and K_{max} Test Conditions for Ti-6Al-4V β-STOA

The data at constant R exhibits fanning in the threshold regime. The fanning is most likely due to load-history effects, as shown in figure 75. Four tests were conducted at R = 0.1 with four different initial ΔK_i values to start the LR tests. The two test results shown by solid symbols violated the ASTM LR standard (initial rate greater than 1E-08 m/cycle). A third test that started at the ASTM maximum specified rate also produced a threshold and rate data that agreed with the previous two invalid tests. A fourth test, which started at a much lower ΔK_i value, produced significantly lower results than the other three tests. The diamond symbols show the ΔK-increasing test results on the fourth specimen. These results alone suggest that the maximum rate specified in the ASTM standard is too high and strictly following the standard can produce load-history-affected results.

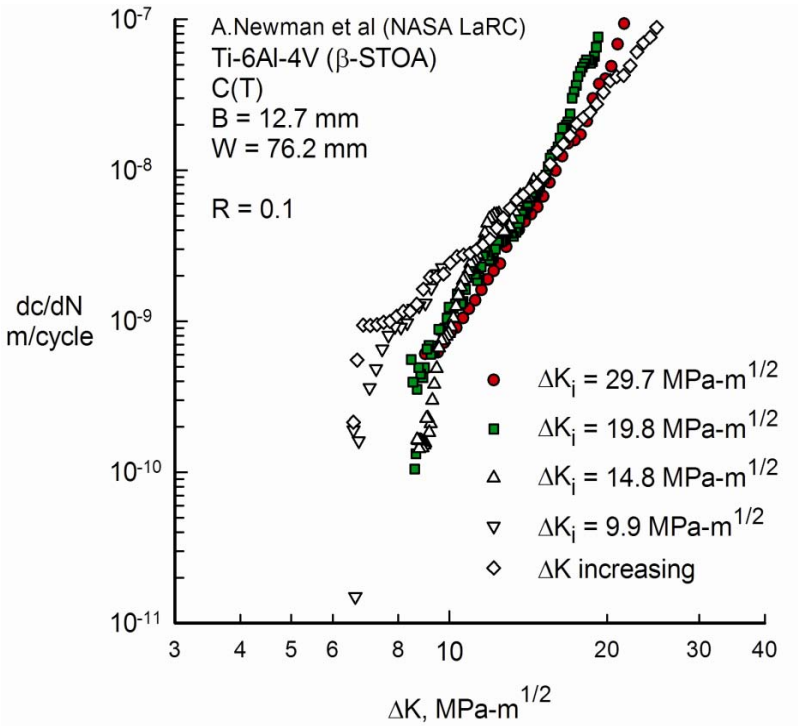

Figure 75. Fatigue Crack Growth Data for R = 0.1 Test Conditions for Ti-6Al-4V β-STOA

At MSU, three orientations of the β-STOA alloy were tested. From a comparison of data, it was concluded that the LS orientation best matched the NASA LaRC test data. Figure 76 shows the results of a CPCA test that compared very well with the NASA LaRC test at the lowest ΔK_i value above 1E-09 m/cycle, but produced an even lower threshold.

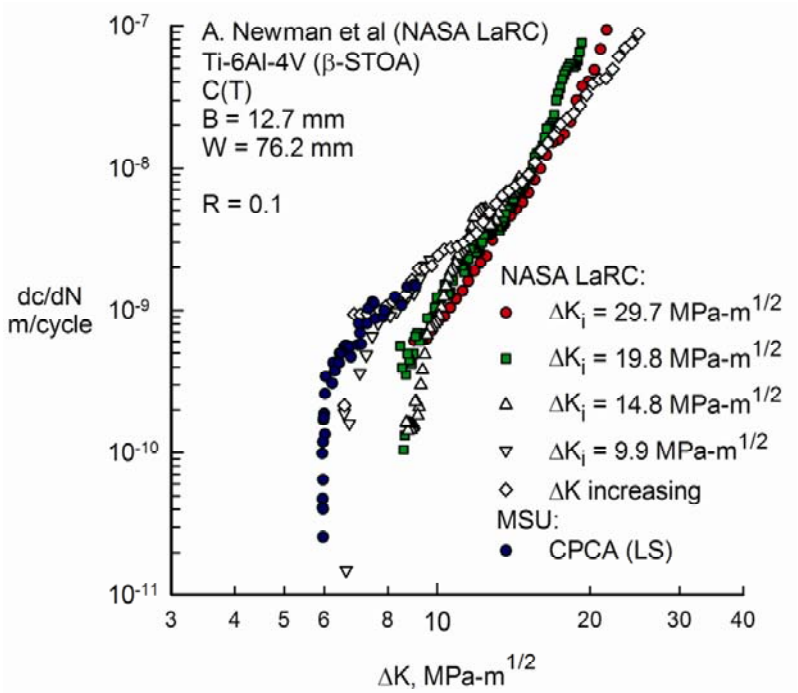

Figure 76. Fatigue Crack Growth Data for R = 0.1 and CPCA Test for Ti-6Al-4V β-STOA

6.2.2 Crack Closure Analyses.

A crack closure analysis of only the constant-R data, shown in figure 74, was conducted to correlate the data into a narrow band on a ΔK_{eff}-rate plot and to determine the constraint factor. Again, an indirect method was used. Figure 77 shows the previous crack-opening load (P_o/P_{max}) ratio against R results for the β-STOA material tested at MSU. The results from the NASA LaRC data in figure 74 (ignoring the data for rates lower than about 3E-09 m/cycle) are shown as open symbols. These results agreed very well with the previous results in the LS orientation. Thus, the constraint factor (α) was 1.5 to correlate the constant-R data on a ΔK_{eff}-rate plot, as shown in figure 78, and the data for the baseline curve is shown in table 10. The data correlated very well in the mid- and upper-rate regimes, except for a slight spread in the threshold regime with stress ratio (i.e., the low-R test showed a higher threshold). The higher threshold for R = 0.1 data is believed to have been caused by the LR test procedure. The curve with open-circular symbols shows the ΔK_{eff}-rate curve. Above a rate of about 2E-09 m/cycle, the curve was a best fit to the data shown, but at lower rates the curve was estimated from an R = 0.9 test (see figure 44). However, further study and measurements of crack-opening loads in the threshold and near-threshold regimes need to be made.

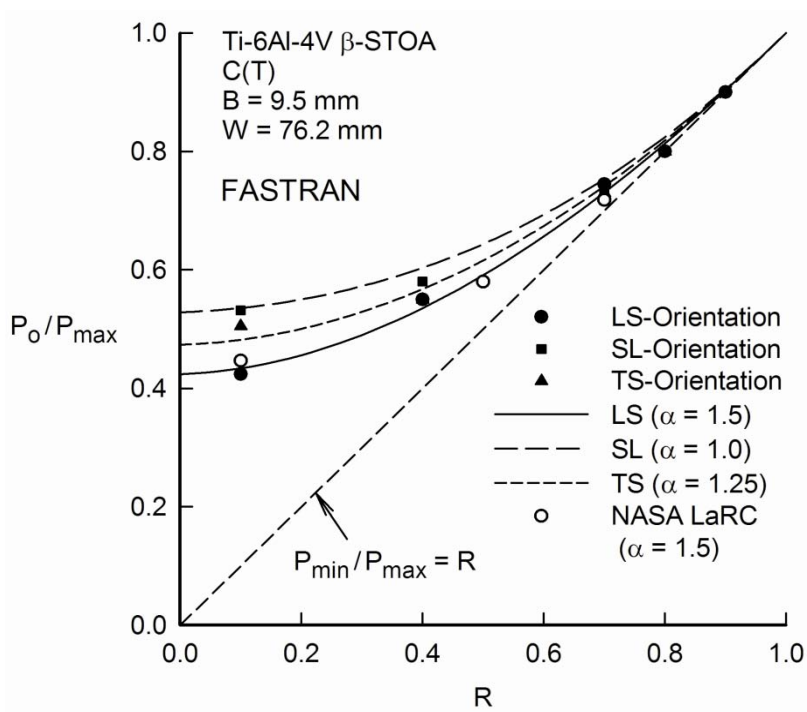

Figure 77. Indirect Determination of Crack-Opening Loads and Constraint Factor for Ti-6Al-4V β-STOA Tested at NASA LaRC

The coefficients in the threshold term, $[1 - (\Delta K_o/\Delta K_{eff})^p]$, were evaluated from test data presented in figure 44 from the MSU tests on the LS orientation and figure 74 for the NASA LaRC tests. The ΔK_o values as a function of R are shown in figure 79. The tests from NASA LaRC produced higher effective thresholds than the MSU tests, again, indicating the load-history effects. Here, the power-law was fit to the MSU tests and a power, p = 10, was selected to best match the shape of the ΔK-rate curves.

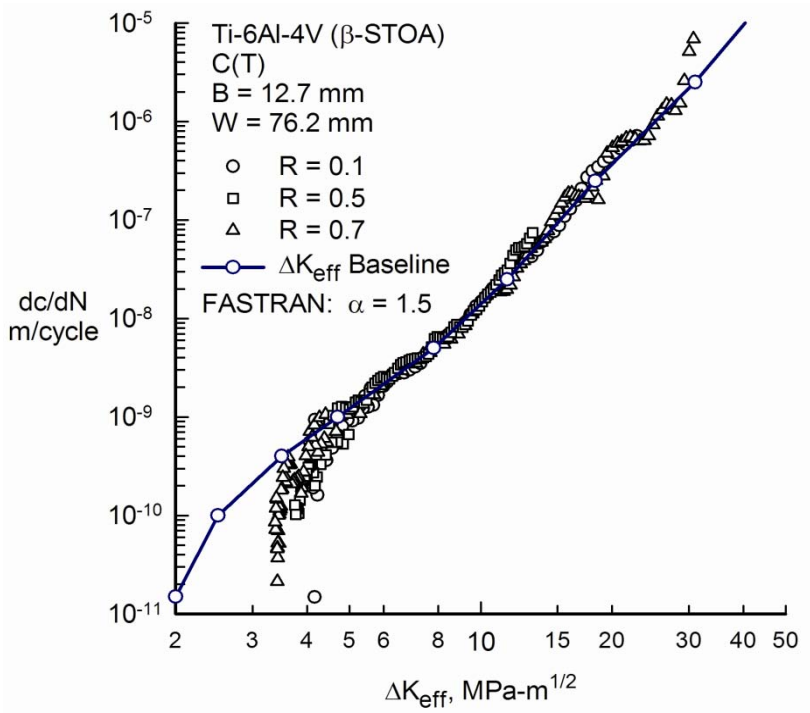

Figure 78. Effective Stress-Intensity Factor Range Against Rates for Ti-6Al-4V β-STOA

Table 10. Effective Stress-Intensity Factor Range Against Rate Relation for Ti-6Al-4V β-STOA (B = 12.7 mm)

ΔK_{eff}, MPa√m	dc/dN, m/cycle
2.00	1.50e-11
2.50	1.00e-10
3.50	4.00e-10
4.70	1.00e-09
7.80	5.00e-09
11.5	2.50e-08
18.3	2.50e-07
31.0	2.50e-06
48.0	2.50e-05
α = 1.5	All rates
C_3 = 3.8 MPa√m	C_4 = 0.15
p = 10	—
C_5 = 115 MPa√m	q = 4

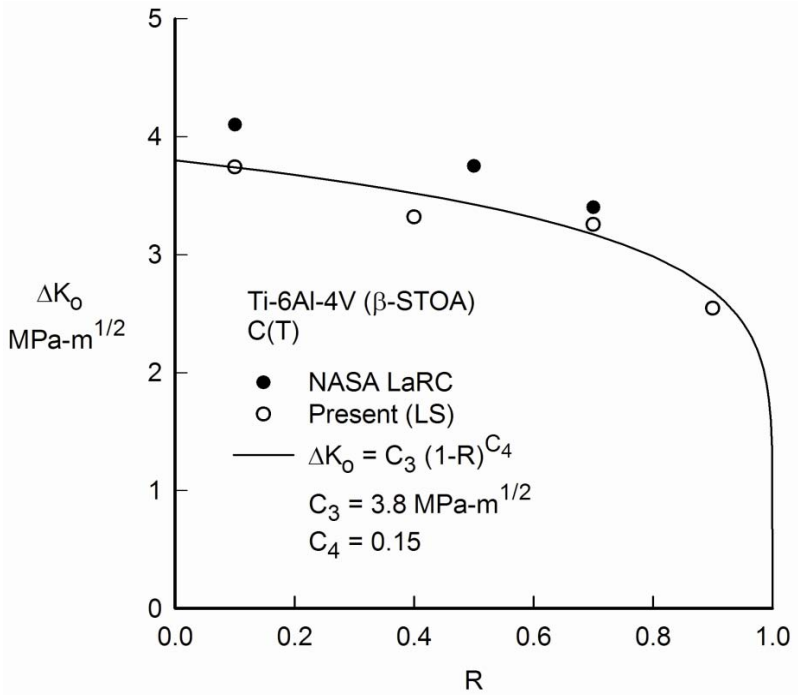

Figure 79. Effective Stress-Intensity Factor Range Thresholds for Ti-6Al-4V β-STOA

Coefficients in the fracture term, $[1 - (K_{max}/C_5)^q]$, were also estimated from test results from MSU for the LS orientation. Several C(T) specimens made of a similar material were cycled to failure at both low and high R. From these results, the cyclic fracture toughness, C_5, was estimated at 115 MPa√m with q = 4. However, it is suspected that the K_{Ie} values are not constant, but vary with crack length and specimen width. However, insufficient test data was available to conduct a TPFC analysis.

A comparison of measured and predicted crack growth rate behavior from the crack closure model on the NASA LaRC data at low and high R is shown in figure 80. The dashed lines with open symbols show the ΔK_{eff}-rate baseline results, which were used to predict the various results at an R equal to 0.1, 0.5, and 0.7. Above a rate of about 1E-09 m/cycle, the predicted results agreed well with the valid test data. But in the threshold and near-threshold regimes, the test results produced slightly higher thresholds and slower rates than the predicted results.

Figure 81 shows all valid data from NASA LaRC, using the ASTM LR method, and from MSU, using the CPCA method, for R = 0.1. The predicted curve agreed well with the CPCA test results and the NASA LaRC test results with the lowest ΔK_i value used with the LR method. The NASA LaRC test results shown by the solid-triangular symbols also satisfied the ASTM LR test standard, but clearly demonstrated an elevated threshold and slower rates due to load-history effects from load shedding.

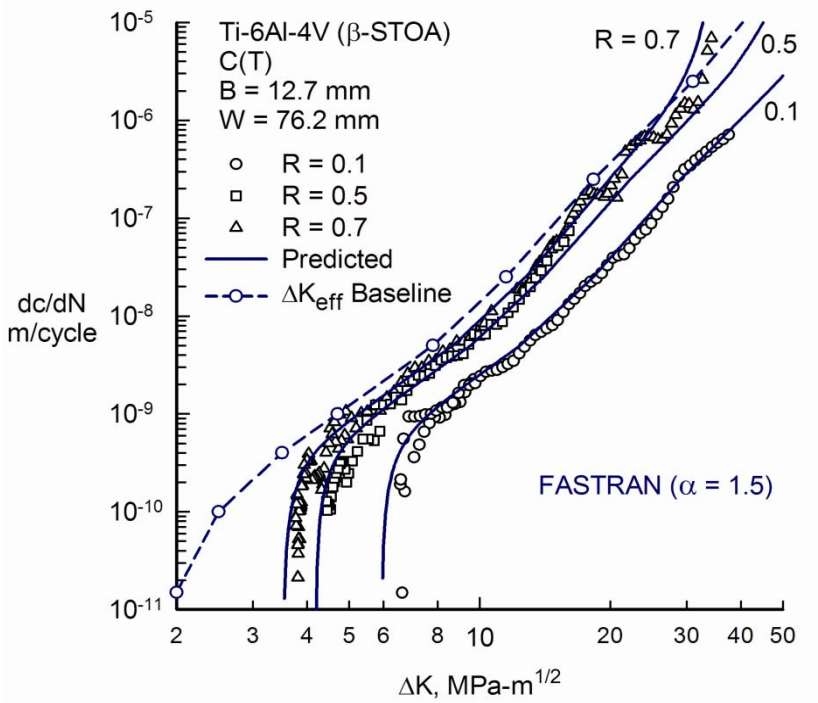

Figure 80. Measured and Predicted Crack Growth Rates on Ti-6Al-4V β-STOA for a Wide Range in Stress Ratios

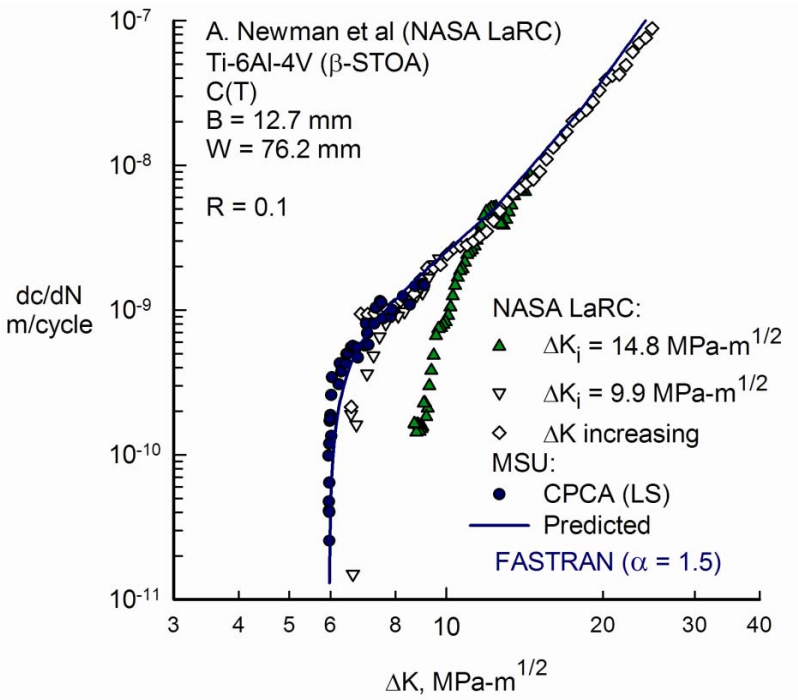

Figure 81. Measured and Predicted Crack Growth Rates on Ti-6Al-4V β-STOA for Near-Threshold Regime for R = 0.1

6.3 MAGNESIUM ALLOY AZ91E.

Fatigue crack growth rate data on the AZ91E magnesium alloy was received from NASA LaRC [32]. C(T) specimens were used to generate test data from threshold to near fracture (in laboratory air and at room temperature). Two test methods were used: (1) ASTM LR and (2) CPCA loading. The material temper and tensile properties (yield stress, ultimate tensile strength, and modulus of elasticity) were not provided and were not reported in reference 32.

Figure 82 shows the R = 0.1 and 0.7 data. These data show the usual behavior with the high-R ratio test giving higher rates at the same stress-intensity factor range and lower threshold than low R. Cracks in the high-stress ratio tests have previously been considered to be fully open cracks (no crack closure). Thus, the R = 0.7 data was used to help establish the effective stress-intensity factor against rate (ΔK_{eff}-rate) baseline curve for the material and test conditions, as shown in figure 83. Because the high-R tests fracture is at lower values of ΔK than low-R tests, i.e., $\Delta K_c = K_c\ (1\text{-}R)$, the low-R test results are also used to estimate the ΔK_{eff}-rate curve at high rates. A constraint factor (α) of 1.55 was found to correlate the low- and high-R test data over a wide range in rates. The solid curve with symbols shows the ΔK_{eff} baseline curve for the magnesium alloy (see table 11). This curve was chosen as a best fit to the average behavior of the test data. The threshold and fracture terms in equation 6 were not used on the magnesium alloy. Multilinear equation 6 was used to model the threshold behavior. The fracture toughness (K_c) was estimated to be 16.5 MPa√m.

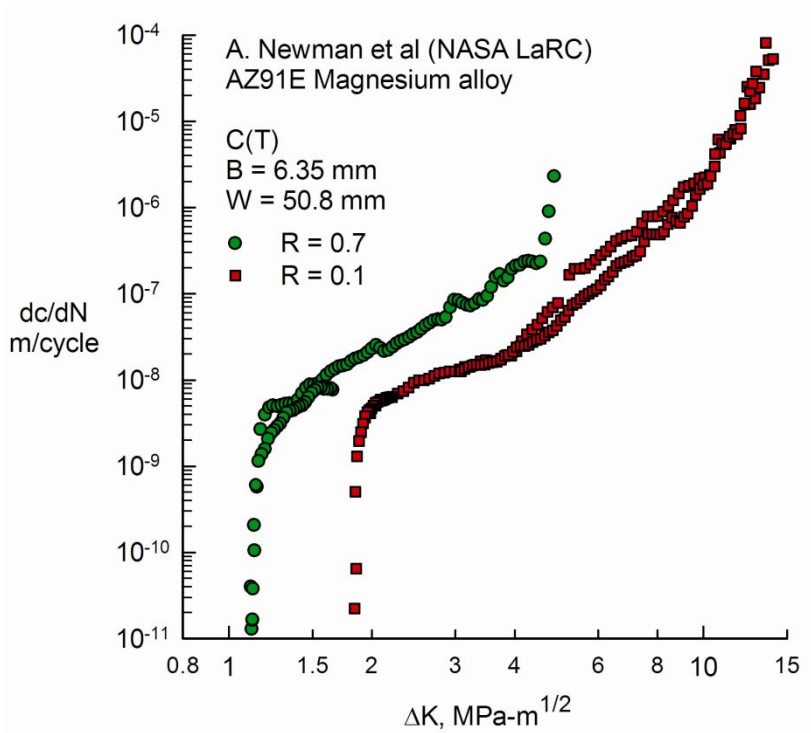

Figure 82. Fatigue Crack Growth Data for R = 0.1 and 0.7 for Mg AZ91E

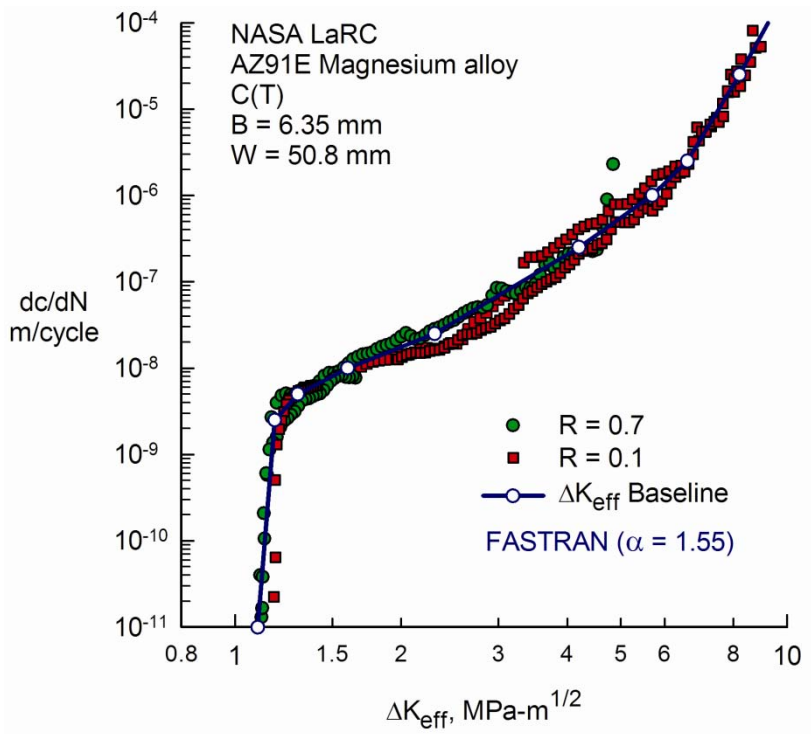

Figure 83. Effective Stress-Intensity Factor Range Against Rates for Mg AZ91E

Table 11. Effective Stress-Intensity Factor Range Against Rate Relation for Mg AZ91E (B = 6.35 mm)

ΔK_{eff}, MPa√m	dc/dN, m/cycle
1.10	1.0e-11
1.18	2.5e-09
1.30	5.0e-09
1.60	1.0e-08
2.30	2.5e-08
4.20	2.5e-07
5.70	1.0e-06
6.60	2.5e-06
8.20	2.5e-05
10.0	2.5e-04
α = 1.55	All rates
C3 = 0	$C_4 = 0$
C_5 = 16.5 MPa√m	q = ∞

Figure 84 shows how well the crack closure model can predict the crack growth behavior at various stress ratios. The vertical arrows indicated when K_{max} is equal to K_c and fracture occurs.

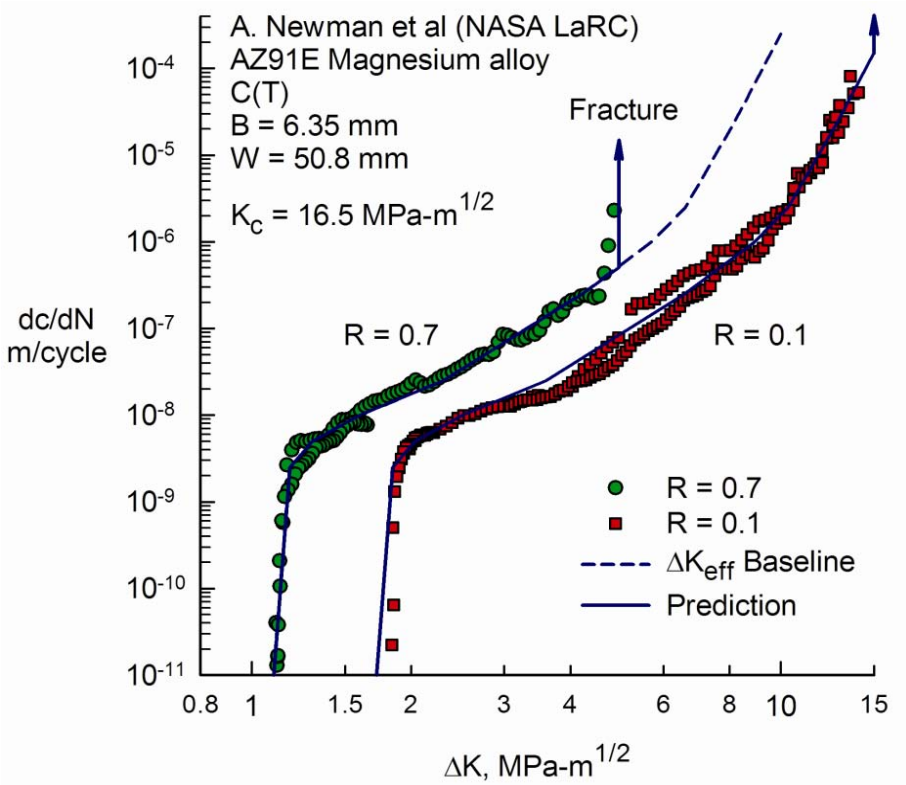

Figure 84. Measured and Predicted Crack Growth Rates on Mg AZ91E for Low and High Stress Ratios

The results from two CPCA tests at R = 0.1 are shown in figure 85 as solid circles and open-square symbols. The rates start on the high-R (ΔK_{eff}-rate) curve because the crack is fully open after compression pre-cracking, but the rates rapidly approach the steady-state behavior and merge with the LR results at R = 0.1. Because the tensile properties were not determined, evaluation of the crack extension criterion (equation 2) could not be made. However, once the CPCA test results start to steadily increase, it is suspected that the crack extension criterion has been met. These results demonstrate that for some materials there may be very little difference between the ASTM LR and CPCA threshold test results. However, further tests at R = 0.1 at lower initial ΔK_i values and at high R need to be conducted.

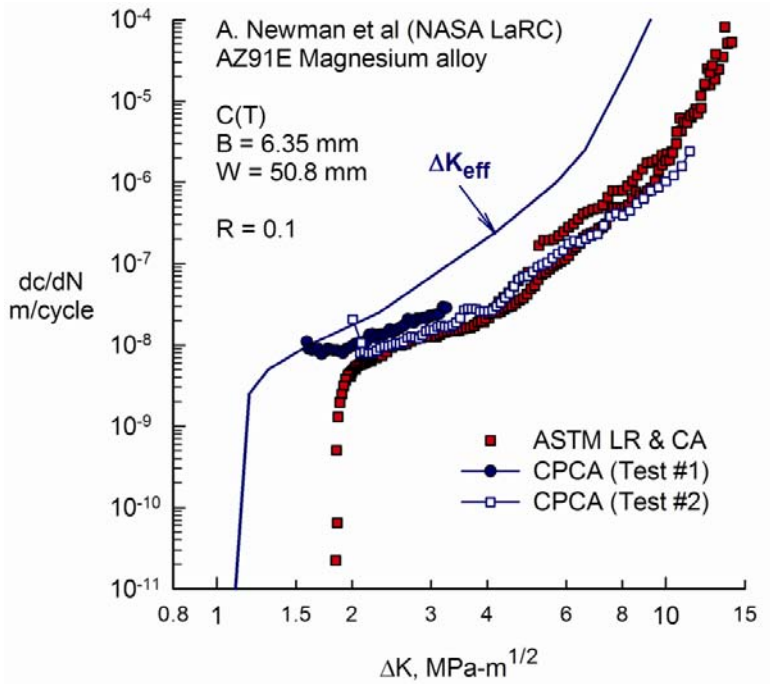

Figure 85. Fatigue Crack Growth Data for R = 0.1 and CPCA Test Conditions for Mg AZ91E

7. DISCUSSION.

Since 2003, a large number of materials have been tested with the three threshold test methods (ASTM LR, CPCA, and CPLR). These materials were four aluminum alloys, two titanium alloys, one magnesium alloy, one superalloy, and steel. These materials are listed in table 12, and those that have experimentally shown major differences among the various test methods are indicated along with the appropriate sources of information.

Table 12. Materials Tested With Three Threshold Test Methods (ASTM LR, CPCA, and CPLR)

Material	Major Differences Among Test Methods	Source
2324-T39	(a)	22 and 29
7050-T7451	Yes	32, 59, and in this report
7075-T651	No	30 and in this report
7075-T7351	Yes	27 and 29
Ti-6Al-4V STOA	Yes	30 and 31
Ti-6Al-4V β-STOA	Yes	32 and in this report
Magnesium AZ91E	(b)	32
4340 Steel	No	In this report
Inconel-718	Yes	21

(a) The CPCA method produced slightly lower thresholds than LR.
(b) An insufficient number of CP tests were conducted to identify the trends.

Of the nine materials tested under Federal Aviation Administration (FAA)- and Office of Naval Research-sponsored research, using the three threshold test methods, two of the materials (7075-T651 and 4340 steel) showed very little difference. Five materials (7050-T7451, 7075-T7351, Ti-6Al-4V STOA, Ti-6Al-4V β-STOA, and Inconel-718) showed large differences, with the CPCA and CPLR test methods producing lower thresholds and faster rates in the near-threshold regime. One aluminum alloy, 2324-T39, produced slightly lower thresholds using the CPCA method compared to the LR method; and for the magnesium alloy (AZ91E) not enough CP tests were conducted to make an assessment. The materials that showed very little difference had crack surfaces that were very flat and straight, while the materials that showed a significant difference exhibited either very rough crack surface profiles or produced fretting debris along the crack surfaces. Thus, it is suspected that load-history effects, due to residual plastic deformations in combination with roughness- and fretting debris-induced crack closure, cause the ASTM LR to induce inadvertently high thresholds and slower crack growth rates in the midregion approaching threshold conditions due to premature crack surface contact. Whereas, the CP methods produced a tensile residual-stress field that caused initially high (invalid) rates. But the crack must be grown under CA loading at least two compressive plastic-zone sizes from the crack starter notch to approach steady-state conditions. At this point, CA loading could either be continued or an LR test could be conducted.

For some materials, like the 4340 steel, a crack could not be initiated at the standard crack starter notch at the ΔK level corresponding to the maximum-allowed rate (1E-8 m/cycle), and higher stress-intensity factors were required. However, CP tests allowed cracks to be initiated at ΔK levels close to the ΔK_{th} values, and thus, load-history effects would be minimized.

In reference 21, the differences observed between ASTM LR and CPLR/CA loading on the Inconel-718 alloy at high R (0.7) was very surprising. These results suggest that high-R closure [21 and 22] may be activated during the LR test. Previous tests at high-R conditions on aluminum alloys [29] and titanium alloy [30 and 31] showed excellent agreement between all methods.

In references 30 and 31, a C(T) specimen width effect on thresholds was observed using the ASTM LR method, where larger-width specimens produced higher thresholds and slower crack growth rates in the near-threshold regime. But threshold and near-threshold results using the CPCA test method were found to be independent of width. These results are very similar to those reported by Garr and Hresko [50] on an Inconel-718 alloy.

In another project sponsored by the FAA with the NASA LaRC [32], four rotorcraft materials (7050, 4340 steel, AZ91E magnesium, and Ti-6Al-4V β-STOA) were tested with the ASTM LR test method. But they presented CPCA results on only one of the materials (7050), and here, only a few tests at R = 0.1 were conducted. From these results, it was concluded that the ASTM LR method showed little or no apparent load-history effects when ASTM E 647 LR reduction procedures were strictly followed. (NASA LaRC gave additional CPCA and CPCK test data to MSU that were not presented in the subject reference. Some of these data were presented in this report.) Because extensive CP tests were not performed on the 7050 aluminum and AZ91E magnesium alloys in reference 32, a proper assessment between the ASTM LR and CPCA/CPLR methods could not be made. Tests conducted at MSU on the same batch of 7050 C(T) specimens

(received from NASA LaRC) showed a significant difference between ASTM LR and CPLR tests at R = 0.1. On a similar β-STOA titanium alloy, as tested at NASA LaRC, significant differences were observed between the methods. However, the large scatter observed in this material, due to the large-grain microstructure and possible forging residual stresses, is of concern. But the CP methods consistently produced significantly lower thresholds and faster crack growth rates in the near-threshold regime. Also, the 4340 steels tested at MSU and NASA LaRC showed drastically different behavior in the threshold and near-threshold regimes. For example, the ΔK_{th} thresholds at R = 0.1 from both organizations were more than a factor of 2 different (4 versus 8.8 MPa√m). The reason for the large difference is unknown, but 4340 steel C(T) specimens previously tested at NASA LaRC may not have been heat treated (see reference 59), and these tests also produced a high threshold (7.7 MPa√m).

In the ASTM E 647 standard, it is stated that a ΔK-increasing (LI) test should be conducted immediately after the ΔK-decreasing test to verify that both test procedures give nearly the same results, which would validate the LR results. However, the validity of this statement needs further study. If a load-history event influenced the threshold development, then the increasing ΔK test would exhibit the same influence as the crack grows away from the threshold condition. This effect was demonstrated on the β-STOA titanium alloy, in that the LI test results agreed well with the LR test results, but both LI and LR results had significantly higher thresholds and slower rates than that produced by CPLR tests.

It is suspected that the maximum-allowed rate in the ASTM LR standard (10^{-8} m/cycle) is too high for some materials and produces elevated thresholds and slower crack growth rates. But in the CPLR method, the CP allowed the initial ΔK levels to be nearly a factor of 2 lower, and at a corresponding rate nearly an order of magnitude (10^{-9} m/cycle) lower, than the ASTM standard LR method. Therefore, many less residual plastic deformations are left along the crack surfaces than in the current LR method (if started at the maximum-allowed rate).

From a mechanic standpoint, when using the LR method, it is difficult to overcome load-history effects, because as the ΔK level is reduced, the crack surface displacements also become progressively smaller until the crack surfaces contact from plasticity, roughness, and fretting debris mechanisms. Elimination of any of these mechanisms would delay crack surface contact and cause higher crack growth rates. On the other hand, the CP methods induced tensile residual stresses at the crack starter notch and developed fully open cracks before CA loading is applied. Here, the crack surface displacements increased as the crack grew, making it more difficult for the crack surfaces to make contact. However, the crack must be grown at least two compressive plastic-zone sizes to eliminate notch effects, tensile residual-stress effects, and the stabilization of the crack closure mechanisms.

8. CONCLUSIONS.

The scope of this research project was to: (1) further develop the compression precracking (CP) threshold test methods, (2) determine fatigue crack growth rates in the near-threshold regime and over a wide range in rates (from threshold to near fracture) for three materials (7075-T651, Ti-6Al-4V β-STOA, and 4340 steel), and (3) analyze the fatigue crack growth data from three rotorcraft materials (7050-T7451, Ti-6Al-4V β-STOA, and Mg AZ91E) tested at the National

Aeronautics and Space Administration (NASA) Langley Research Center (LaRC). In addition, a few tests on the 7050-T7451 alloy were conducted at Mississippi State University (MSU) using new threshold test methods. At MSU, three types of threshold tests were conducted on each material. They were (1) the ASTM E 647 load-reduction (LR) procedure, (2) the compression precracking, constant-amplitude (CPCA) test method, and (3) the compression precracking, load-reduction (CPLR) test method. An additional test method, compression precracking constant-ΔK was also used on one material tested at NASA LaRC and another material tested at MSU. All tests were conducted under a laboratory air environment at room temperature. These test results were used to develop alternative test methods to determine threshold and near-threshold fatigue crack growth rate behavior for metallic materials. The 7050-T7451 aluminum alloy and the Ti-6Al-4V β-STOA titanium alloy showed significant differences between ASTM LR and CPCA/CPLR tests, but the 7075-T651 and 4340 steel showed small differences.

In conclusion:

1. Procedures were established to prepare test specimens, to apply compressive loading to initiate a crack at a crack starter notch, and to generate steady-state, constant-amplitude loading, crack growth rate data for metallic materials.

2. The CP test methods, CPCA and CPLR, tended to generate lower thresholds and faster fatigue crack growth rates in the near-threshold regime than the standard ASTM LR method for all materials. For some materials, the differences in ΔK_{th} were small (~10%), but for other materials the differences were as large as 50%.

3. Constant-amplitude fatigue crack growth rate data was generated on three materials (7075-T651, Ti-6Al-4V β-STOA, and 4340 steel) from threshold to near fracture over a wide range in stress ratios.

4. Tests conducted at very high stress ratios (R >0.7) show a continuously shifting crack growth rate curve to lower stress-intensity factor ranges with increasing stress ratio that could be caused by either maximum-applied stress-intensity factor, MPa√m (K_{max}), and/or crack closure effects. This observation will require further study and local crack closure measurements taken to help identify the cause(s).

5. The effective stress-intensity factor range against rate (ΔK_{eff}-rate) relation has been developed for most of the materials tested and analyzed in this report. These relations may be used in various damage tolerance life-prediction codes to assess the fatigue crack growth lives of structural components.

9. REFERENCES.

1. Paris, P.C. and Erdogan, F., "A Critical Analysis of Crack Propagation Laws," Transactions of the ASME, *Journal of Basic Engineering*, Series D, Vol. 85, No. 3, 1963.

2. Barsom, J.M., "Fatigue Crack Propagation in Steels of Various Yield Strengths," Transactions of the ASME, *Journal of Engineering for Industry*, Series B, Vol. 93, No. 4, 1971.

3. McEvily, A.J., Jr. and Illg, W., "The Rate of Fatigue Crack Propagation in Two Aluminum Alloys," NACA TN 4394, 1958.

4. Standard Test Method for Measurement of Fatigue Crack Growth Rates, ASTM International E 647, Vol. 03.01, 2006.

5. Paris, P.C., Bucci, R., Wessel, E., Clark, W., and Mager, T., "Extensive Study of Low Fatigue Crack Growth Rates in A533 and A508 Steels," *ASTM STP 513*, American Society for Testing and Materials, Philadelphia, Pennsylvania, 1972, pp. 141-176.

6. Schmidt, R.A. and Paris, P.C., "Threshold for Fatigue Crack Propagation and the Effects of Load Ratio and Frequency," *ASTM STP-536*, American Society for Testing and Materials, Philadelphia, Pennsylvania, 1973, pp. 79-94.

7. Hudak, S., Jr., Saxena, S., Bucci, R., and Malcolm, R., "Development of Standard Methods of Testing and Analyzing Fatigue Crack Growth Rate Data," AFML TR 78-40, Air Force Materials Laboratory, Wright Patterson Air Force Base, Ohio, 1978.

8. Bucci, R., "Development of a Proposed ASTM Standard Test Method for Near-Threshold Fatigue Crack Growth Rate Measurement," *ASTM STP-738*, American Society for Testing and Materials, Philadelphia, Pennsylvania, 1981, pp. 5-28.

9. Ohta, A. and Sasaki, E., "A Method for Determining the Stress Intensity Threshold Level for Fatigue Crack Propagation," *Engineering Fracture Mechanics*, Vol. 9, No. 3, 1977, pp. 655-662.

10. Minakawa, K. and McEvily, A.J., "On Near-Threshold Fatigue Crack Growth in Steels and Aluminum Alloys," *Proceedings of International Conference on Fatigue Thresholds*, Stockholm, Sweden, Vol. 2, 1981, pp. 373-390.

11. Newman, J.C., Jr., "A Nonlinear Fracture Mechanics Approach to the Growth of Small Cracks," Behavior of Short Cracks in Airframe Components, AGARD CP-328, 1983, pp. 6.1-6.27.

12. Newman, J.C., Jr., "Analysis of Fatigue Crack Growth and Closure Near Threshold Conditions," *ASTM STP-1372*, American Society for Testing and Materials, West Conshohocken, Pennsylvania, 2000, pp. 227-251.

13. McClung, R.C., "Analysis of Fatigue Crack Closure During Simulated Threshold Testing," *ASTM STP-1372*, American Society for Testing and Materials, West Conshohocken, Pennsylvania, 2000, pp. 209-226.

14. Suresh, S., Zaminski, G.F., and Ritchie, R.O., "Oxide-Induced Crack Closure: An Explanation for Near-Threshold Corrosion Fatigue Crack Growth Behavior," *Metallurgical Transactions*, Vol. A12A, 1981, pp. 1435-1443.

15. Ritchie, R.O., "Mechanisms of Fatigue Crack Propagation in Metals, Ceramics and Composites: Role of Crack Tip Shielding," *Material Science and Engineering*, Vol. 103, 1988, pp. 15-28.

16. Kirby, B.R. and Beevers, C.J., "Slow Fatigue Crack Growth and Threshold Behaviour in Air and Vacuum of Commercial Aluminium Alloys," *Fatigue and Fracture of Engineering Materials and Structures*, Vol. 1, 1979, pp. 203-216.

17. Herman, W., Hertzberg, R., and Jaccard, R., "A Simplified Laboratory Approach for the Prediction of Short Crack Behavior in Engineering Structures," *Fatigue and Fracture of Engineering Materials and Structures*, Vol. 11, 1988, pp. 303-320.

18. Marci, G., "Fatigue Crack Growth Threshold Concept and Test Results for Al- and Ti-Alloys," *ASTM STP-1372*, American Society for Testing and Materials, West Conshohocken, Pennsylvania, 2000, pp. 81-95.

19. Newman, J.A., Riddell, W.T., and Piascik, R.S., "Effects of K_{max} on Fatigue Crack Growth Threshold in Aluminum Alloys," *ASTM STP-1372*, American Society for Testing and Materials, West Conshohocken, Pennsylvania, 2000, pp. 63-77.

20. Vasudevan, A.K., Sadananda, K., and Louat, N., "A Review of Crack Closure, Fatigue Crack Threshold, and Related Phenomena," *Materials Science and Engineering*, Vol. A188, 1994, pp. 1-22.

21. Yamada, Y. and Newman, J.C., Jr., "Crack Closure Under High Load-Ratio Conditions for Inconel-718 Near Threshold Behavior," *Engineering Fracture Mechanics*, Vol. 76, 2009, pp. 209-220.

22. Yamada, Y. and Newman, J.C., Jr., "Crack Closure Behavior of 2324-T39 Aluminum Alloy Near Threshold Conditions for High-Load Ratio and Constant K_{max} Tests," *International Journal of Fatigue*, Vol. 31, 2009, pp. 1780-1787.

23. Hubbard, R.P., "Crack Growth Under Cyclic Compression," *Journal of Basic Engineering*, Vol. 91, 1969, pp. 625-631.

24. Topper, T. H. and Au, P., "Fatigue Test Methodology," AGARD Lecture Series 118, The Technical University of Denmark, Denmark, 1981.

25. Pippan, R., "The Growth of Short Cracks Under Cyclic Compression," *Fatigue and Fracture of Engineering Materials and Structures*, Vol. 9, 1987, pp. 319-328.

26. Pippan, R., Plöchl, L., Klanner, F., and Stüwe, H.P., "The Use of Fatigue Specimens Precracked in Compression for Measuring Threshold Values and Crack Growth," *ASTM Journal of Testing Evaluation*, Vol. 22, 1994, pp. 98.

27. Forth, S.C., Newman, J.C., Jr., and Forman, R.G., "On Generating Fatigue Crack Growth Thresholds," *International Journal of Fatigue*, Vol. 25, 2003, pp. 9-15.

28. Forth, S.C., Newman, J.C., Jr., and Forman, R.G., "Evaluation of Fatigue Crack Thresholds Using Various Experimental Methods," *ASTM STP-1461*, West Conshohocken, Pennsylvania, ASTM International, 2005, pp. 203-218.

29. Newman, J.C., Jr., Schneider, J., Daniel, A., and McKnight, D., "Compression Precracking to Generate Near Threshold Fatigue Crack Growth Rates in Two Aluminum Alloys," *International Journal of Fatigue*, Vol. 27, 2005, pp. 1432-1440.

30. Ruschau, J. and Newman, J.C., Jr., "Compression Precracking to Generate Near-Threshold Fatigue Crack Growth Rates in an Aluminum and Titanium Alloy," *Journal of ASTM International*, Vol. 5, No. 7, 2008.

31. Ruschau, J. and Newman, J.C., Jr., "Improved Test Methods for Very Low Fatigue Crack Growth Rate Data," *American Helicopter Society International 64th Annual Forum & Technology Display*, Montréal, Canada, 2008.

32. Newman, J.A., James, M.A., Johnston, W.M., and Le, D.D., "Fatigue Crack Growth Threshold Testing of Metallic Rotorcraft Materials," NASA/TM-2008-215331, ARL-TR-4472, July 2008.

33. Donald, J.K. and Paris, P.C., "An Evaluation of ΔK_{eff} Estimation Procedures on 6061-T6 and 2024-T3 Aluminum Alloys," *Proceedings of Fatigue Damage of Structural Materials II*, Cape Cod, Massachusetts, 1998.

34. *Metals Handbook, Vol. 2, Properties and Selection: Nonferrous Alloys and Special-Purpose Materials*, ASM International, 10th Ed., 1990.

35. Jordon, J.B., "Experiments and Modeling of Fatigue and Fracture of Aluminum Alloys," Ph.D. Dissertation, Mississippi State University, Mississippi State, MS, 2009.

36. Forth, S.C., Favrow, L.H., Keat, W.D., and Newman, J.A., "Three-Dimensional Mixed-Mode Fatigue Crack Growth in a Functionally Graded Titanium Alloy," *Engineering Fracture Mechanics*, Vol. 70, 2003, pp. 2175-2185.

37. Newman, J.A., James, M.A., Johnston, W.M., and Le, D.D., "Fatigue Crack Growth Threshold Testing of Metallic Rotorcraft Materials," NASA/TM-2008-215331, ARL-TR-4472.

38. *ASM Metals Reference Book*, 2nd Edition, American Society for Metals, Metals Park, Ohio, 1983.

39. Elber, W., "The Significance of Fatigue Crack Closure," Damage Tolerance in Aircraft Structures, *ASTM STP-486*, American Society for Testing and Materials, Philadelphia, Pennsylvania, 1971, pp. 230-242.

40. Walker, N. and Beevers, C.J., "A Fatigue Crack Closure Mechanism in Titanium," *Fatigue of Engineering Materials and Structures*, Vol. 1, No. 1, 1979, pp. 135-148.

41. Suresh, S. and Ritchie, R.O., "A Geometric Model for Fatigue Crack Closure Induced by Fracture Surface Roughness," *Metallurgical Transactions*, Vol. 13A, 1982, pp. 1627-1631.

42. Suresh, S., Parks, D., and Ritchie, R., "Crack Tip Oxide Formation and Its Influence on Fatigue Thresholds," *Proceedings Symposium on Fatigue Thresholds*, Backlund, J., Blom, A., and Beevers, C., eds., EMAS Ltd., Warley, United Kingdom, 1982, pp. 391-408.

43. James, M.A., Forth, S.C., and Newman, J.A., "Load History Effects Resulting From Compression Precracking," *ASTM STP-1461*, ASTM International, West Conshohocken, Pennsylvania**,** 2005, pp. 43-59.

44. Yamada, Y., Newman, J.C., III, and Newman, J.C., Jr., "Elastic-Plastic Finite Element Analyses of Compression Precracking and its Influence on Subsequent Fatigue Crack Growth," *Journal of ASTM International*, Vol. 5, No. 8, 2008.

45. Chang, C. and Mear, M.E., "A Boundary Element Method for Two-Dimensional Linear Elastic Fracture Analysis," *International Journal of Fracture*, Vol. 74, 1996, pp. 219-251.

46. James, M.A. and Swenson, D.V., "A Software Framework for Two-Dimensional Mixed Mode-I/II Elastic-Plastic Fracture," *ASTM STP-1359*, American Society for Testing and Materials, Philadelphia, Pennsylvania, 1999, pp. 111-126.

47. Tada, H., Paris, P.C., and Irwin, G.R., *The Stress Analysis of Cracks Handbook*, Third Edition, The American Society of Mechanical Engineers, 2000.

48. Newman, J.C., Jr., "A Finite Element Analysis of Fatigue Crack Closure," *ASTM STP-590*, American Society for Testing and Materials, Philadelphia, Pennsylvania, 1976, pp. 281-301.

49. Dugdale, D.S., "Yielding of Steel Sheets Containing Slits," *Journal of the Mechanics and Physics of Solids*, Vol. 8, 1960, pp. 100-104.

50. Garr, K.R. and Hresko, G.C., "A Size Effect on the Fatigue Crack Growth Rate Threshold of Alloy 718," *ASTM STP-1372*, West Conshohocken, Pennsylvania, 2000, pp. 155-174.

51. Pearson, S., "Initiation of Fatigue Cracks in Commercial Aluminum Alloys and the Subsequent Propagation of Very Short Cracks," *Engineering Fracture Mechanics*, Vol. 7, No. 2, 1975, pp. 235-247.

52. Private communication with Dr. H.R. Zonker, Alcoa Technical Center, Alcoa Center, Pennsylvania, 2005.

53. Newman, J.C., Jr., Wu, X. R., Venneri, S.L., and Li, C.G., "Small-Crack Effects in High-Strength Aluminum Alloys—A NASA/CAE Cooperative Program," *NASA RP-1309*, May 1994.

54. Newman, J.C. Jr. "A Crack Opening Stress Equation for Fatigue Crack Growth," *International Journal of Fracture*, Vol. 24, 1984, R131-Rl35.

55. Newman, J.C., Jr., "FASTRAN-II—A Fatigue Crack Growth Structural Analysis Program," NASA TM 104159, 1992.

56. Klesnil, M. and Lukas, P., "Effect of Stress Cycle Asymmetry on Fatigue Crack Growth," *Material Science and Engineering*, Vol. 9, 1972, pp. 231-240.

57. Newman, J.C., Jr., "Fracture Analysis of Surface- and Through-Cracked Sheets and Plates," *Engineering Fracture Mechanics*, Vol. 5, 1973, pp. 667-689.

58. Newman, J.C., Jr., "Fracture Analysis of Various Cracked Configurations in Sheet and Plate Materials," *Properties Related to Fracture Toughness*, *ASTM STP 605*, American Society for Testing and Materials, Philadelphia, Pennsylvania, 1976, pp. 104-123.

59. Newman, J.C., Jr. and Yamada, Y., "Crack Closure Behavior of Two Aluminum Alloys Near-Threshold Conditions for High Load Ratio and Constant K_{max} Tests," *Ninth International ASTM/ESIS Symposium on Fatigue and Fracture Mechanics*, Vancouver, California, May 2009.

60. Forth, S.C., James, M.A., Newman, J.A., and Everett, R.A., Jr., "Mechanical Data for Use in Damage Tolerance Analyses," NASA/TM-2004-213503.

61. Newman, J.C., Jr., "Analyses of Fatigue Crack Growth Databases for Use in Damage Tolerance Approach for Aircraft Propellers and Rotorcraft," FAA report DOT/FAA/AR-07/49, November 2007.

APPENDIX A—CRACK LENGTH AND BACK-FACE STRAIN GAGE RELATION FOR COMPACT SPECIMENS

A.1 INTRODUCTION.

Compact tension C(T) specimens are the most widely used test specimens to measure fatigue crack growth rates in metallic materials. Two methods were used to automatically monitor crack length in these specimens as a function of cycles. They are the crack mouth opening displacement (CMOD) gage and the back-face strain (BFS) gage, as shown in figure A-1. Compliance relations were developed between CMOD or BFS and the crack length, c, specimen width, W, specimen thickness, B, material elastic modulus, E, and the applied load, P.

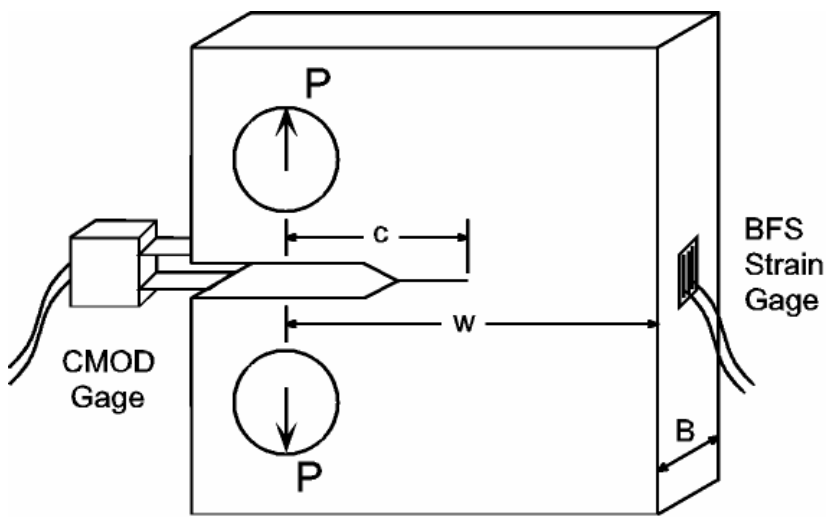

Figure A-1. Compact Specimen With CMOD and BFS Gages

A.2 BACKGROUND.

During the past decade, a number of BFS and crack length relations have been developed for the standard C(T) specimen. Figure A-2 shows a comparison of a number of these relations. Riddell and Piascik [A-1] used FRANC2D [A-2 and A-3] (finite element code) and developed a relation shown by the solid curve. Although not stated, the range of validity of the equation was most likely $0.1 < c/W < 0.9$, since this was the range of their analyses. However, the functional form of the equation was not well suited for use in commonly used crack monitoring systems. Later, Newman and Johnston [A-4] using the Riddell-Piascik FRANC2D results developed an improved equation with the same form as the CMOD equation used in the ASTM E 647 standard [A-5]. This was done so the commonly used crack length monitoring systems could be used by inputting the curve-fitting coefficients and by changing the strain gage polarity due to compressive strains being measured at the back-face. The expression by Newman-Johnston is

$$c/W = A_0 + A_1 U + A_2 U^2 + A_3 U^3 + A_4 U^4 + A_5 U^5 \qquad \text{(A-1)}$$

where $U = 1/(\sqrt{A} + 1)$ and $A = |\varepsilon EBW/P|$ for $0.2 < c/W < 0.8$. Equation A-1 is shown as the small-dashed curve.

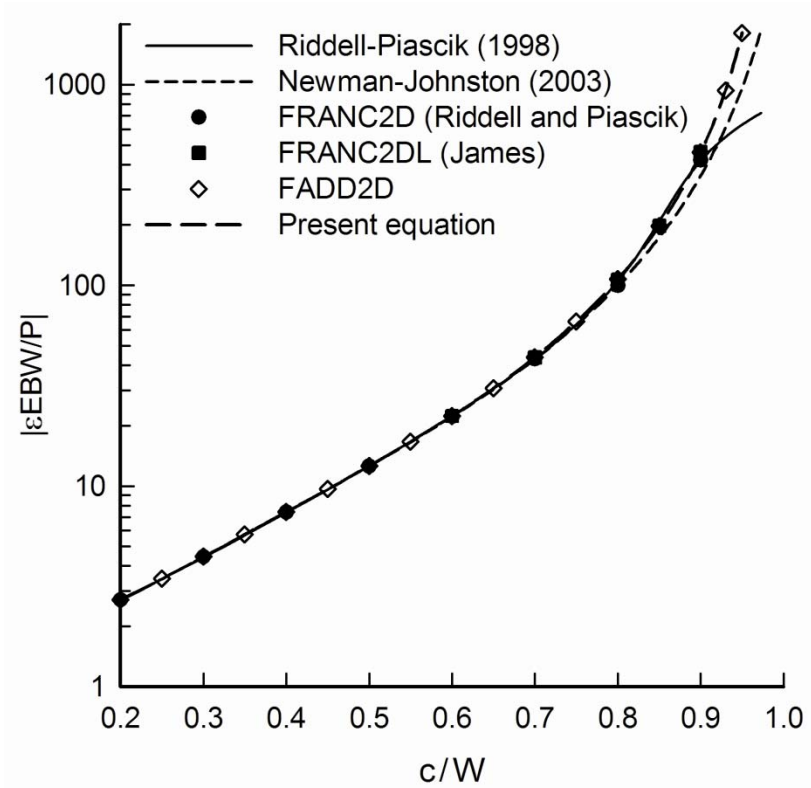

Figure A-2. Normalized BFS for Cracks in Compact Specimens

A.3 ANALYSES.

In experiments, the Newman-Johnston [A-4] BFS expression worked very well for c/W ratios less than 0.8. However, discrepancies between actual and measured crack lengths for c/W ratios greater than approximately 0.8 were observed. Efforts were then made to independently verify the Newman-Johnston equation for extremely deep cracks. Two analyses were conducted: (1) FRANC2DL and (2) FADD2D. Mark James from the National Institute of Aerospace at the National Aeronautics and Space Administration (NASA) Langley Research Center used FRANC2DL [A-6 and A-7] (finite element code) to determine the normalized BFS results for very deep cracks (square symbols). The FADD2D [A-8] boundary element code was also used at Mississippi State University (MSU) to analyze the full range of crack length-to-width ratios (0.1 to 0.95) and these numerical results are shown as diamond symbols. These results are also given in table A-1. Using the FADD2D results, an improved wide-range equation was developed and is given by

$$c/W = A_0 + A_1 U + A_2 U^2 + A_3 U^3 + A_4 U^4 + A_5 U^5 \qquad \text{(A-2)}$$

$A_0 = 1.0033$ $\quad A_1 = -2.35$ $\quad A_2 = 1.3694$

$A_3 = -15.294$ $\quad A_4 = 63.182$ $\quad A_5 = -74.42$

where $U = 1/(\sqrt{A} + 1)$ and $A = |\varepsilon EBW/P|$ for $0.2 < c/W < 0.95$. Equation A-2 is shown as the large-dashed curve in figure A-2.

Table A-1. The FADD2D Normalized BFS Results

c/W	|εEBW/P|	c/W	|εEBW/P|
0.10	1.783	0.60	22.348
0.15	2.162	0.65	30.736
0.20	2.704	0.70	43.832
0.25	3.449	0.75	65.925
0.30	4.443	0.80	107.271
0.35	5.742	0.85	197.996
0.40	7.437	0.90	460.045
0.45	9.660	0.93	936.53
0.50	12.618	0.95	1808.2
0.55	16.656	—	—

The results in figure A-2 show that the Riddell-Piascik equation applies for c/W ratios from 0.2 to 0.9, while the Newman-Johnston equation can only be applied up to c/W ratios of 0.8. But equation A-2 can be applied from c/W of 0.2 to 0.95.

Figure A-3 shows the percent difference in calculating c/W values using either the various analyses or the equations and the Newman-Johnston equation as a function of c/W. These results show that the Riddell-Piascik equation is within 2% for c/W ratios less than 0.9 and show that the Newman-Johnston equation is within ±1% for $0.2 < c/W < 0.8$, and within 2% for $c/W < 0.9$. The results from FRANC2DL and FADD2D codes (open symbols) agreed well for deep cracks ($0.6 < c/W < 0.9$). The coefficients in the Newman-Johnston equation were re-evaluated by fitting to the FADD2D results from c/W ratios from 0.2 to 0.95.

Figure A-4 shows the percent difference in calculating c/W values using equation A-2 and the FADD2D results as a function of c/W. Here, two BFSstrain conditions were used: (1) a standard strain gage size (g = 3.2 mm, height of active strain gage section) and (2) a point value (g = 0). The standard strain gage size was used in all fatigue crack growth rate tests. For the standard strain gage size, the strains calculated from the FADD2D code were integrated over the gage length. The agreement between the equation and the analysis results for the standard strain gage size were within ±0.05% over a very wide range in c/W ratios. Using a smaller- or larger-length strain gage would have resulted in larger differences for very deep cracks ($c/W > 0.8$).

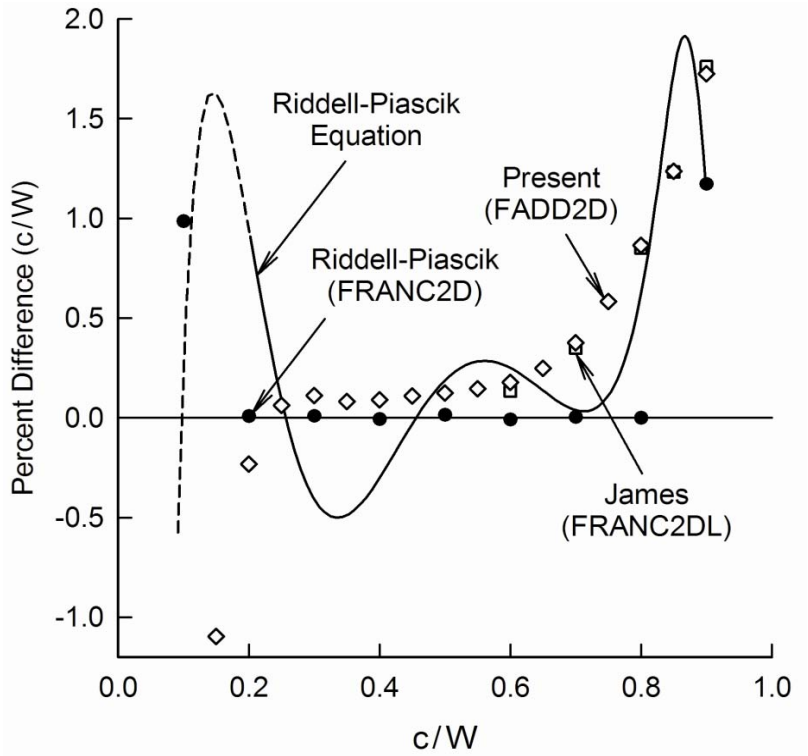

Figure A-3. Percent Difference in Crack-Length Determination From Newman-Johnston Equation

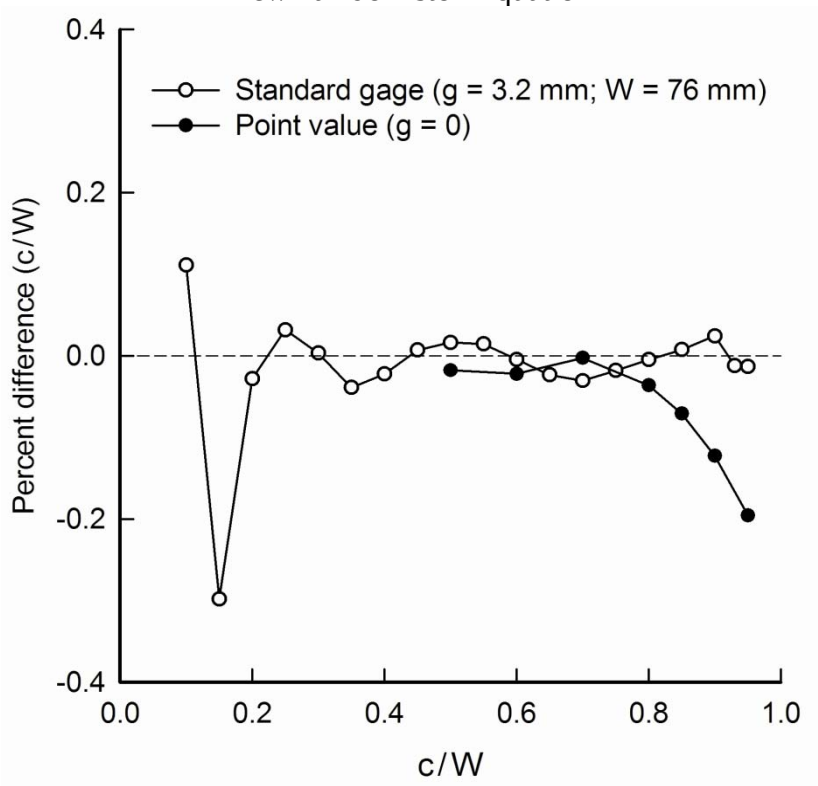

Figure A-4. Percent Difference in Crack Length Determination From Equation A-2

A BFS gage compliance system [A-9] was used in all fatigue crack growth rate tests to monitor crack lengths. The original crack length monitoring system was set up to operate with a CMOD gage, but using the BFS gage, only the coefficients in the compliance equation (same as CMOD expression) and the strain gage polarity had to be updated. During the tests on three materials for very deep cracks, experimental strain gage compliance values were found to differ from the Newman-Johnston equation, but they compare well with the improved wide-range equation, as shown in figure A-5. The 4340 steel C(T) specimens exhibited very flat cracks, and the cracks were grown to very deep c/W ratios, as shown by the square symbols. The Inconel-718 specimens also had fairly flat cracks, but the titanium alloy (Ti-6Al-4V β-STOA) had very rough, nonstraight, and meandering cracks. But the agreement between the measured and calculated crack length-to-width ratios from BFSs was very satisfactory.

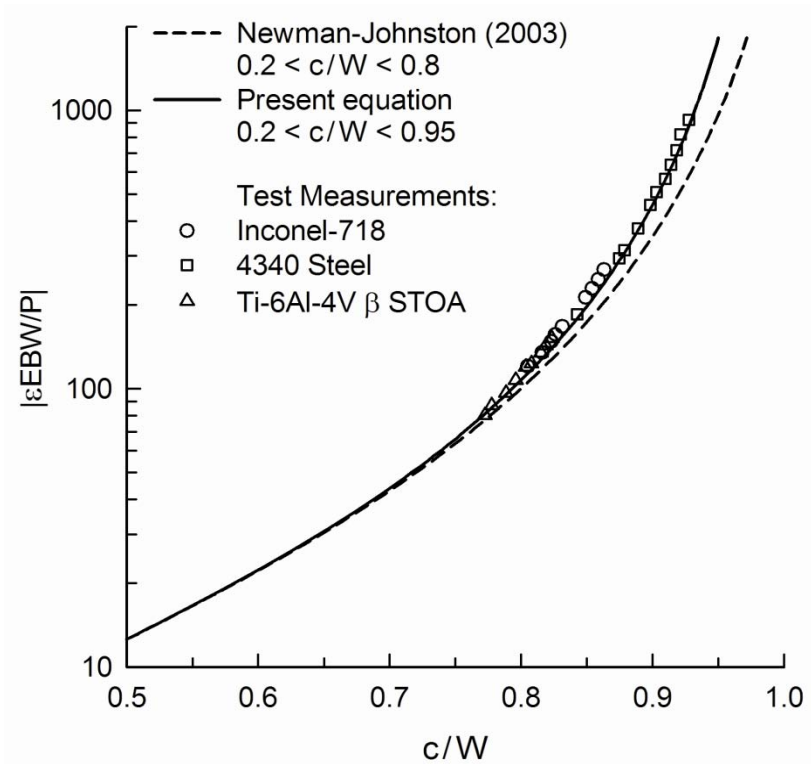

Figure A-5. Comparison of Measured and Calculated Normalized BFS Compliance

A.4 REFERENCES.

A-1. Riddell, W.T. and Piascik, R.S., "A Back-Face Strain Compliance Expression for the Compact Tension Specimen," NASA TM-208453, October 1998.

A-2. Wawrzynek, P.A. and Ingraffea, A.R., "Interactive Finite Element Analysis of Fracture Processes: An Integrated Approach," *Theoretical and Applied Fracture Mechanics*, Vol. 8, 1987, pp. 137-150.

A-3. Wawrzynek, P.A. and Ingraffea, A.R., "FRANC2D: A Two-Dimensional Crack Propagation Simulator," NASA CR-4572, March 1994.

A-4. Private communication with Dr. John A. Newman, U.S. Army at the National Aeronautics and Space Administration, Langley Research Center, 2003.

A-5. "Standard Test Method for Measurement of Fatigue Crack Growth Rates," ASTM International E 647, Vol. 03.01, 2006.

A-6. Gondhalekar, S., "Development of a Software Tool for Crack Propagation Analysis in Two-Dimensional Layered Structures," M.S. Thesis, Kansas State University, 1992.

A-7. James, M.A. and Swenson, D.V., "A Software Framework for Two-Dimensional Mixed Mode-I/II Elastic-Plastic Fracture," ASTM STP-1359, American Society for Testing and Materials, Philadelphia, Pennsylvania, 1999, pp. 111-126.

A-8. Chang, C.C. and Mear, M.E., "A Boundary Element Method for Two-Dimensional Linear Elastic Fracture Analysis," *International Journal of Fracture*, Vol. 74, 1996, pp. 219-251.

A-9. Private communication with Dr. Keith J. Donald, Fatigue Technology Associates, LLC, Bethlehem, Pennsylvania, 2003.

APPENDIX B—PLASTICITY-INDUCED CRACK CLOSURE MODELING

B.1 INTRODUCTION.

The plasticity-induced crack closure model and the FASTRAN code [B-1 and B-2] were developed for a central through crack and two-symmetric through cracks emanating from a circular hole in a finite width plate subjected to uniform remote applied stress. The model was based on the Dugdale strip yield model [B-3], but was modified to leave plastically deformed material in the wake of the crack. The details of the model are given in reference B-1. One of the most important features of the model is the ability to model three-dimensional constraint effects. A constraint factor (α) is used to elevate the flow stress (σ_o) at the crack tip to account for the influence of stress state ($\alpha\sigma_o$) on plastic-zone sizes and crack surface displacements. (The flow stress σ_o is taken as the average between the yield stress σ_{ys} and ultimate tensile strength σ_u of the material.) For plane-stress conditions, α is equal to unity (original Dugdale model); and for simulated plane-strain conditions, α is equal to 3. Although the strip yield model does not model the correct yield-zone pattern for plane-strain conditions, the model with a high-constraint factor is able to produce crack surface displacements and crack-opening stresses quite similar to those calculated from three-dimensional, elastic-plastic finite element analyses of crack growth and closure for finite thickness plates [B-4 and B-5]. The calculations performed herein were made with FASTRAN Version 3.82.

B.2 EFFECTIVE STRESS-INTENSITY FACTOR RANGE.

For most damage tolerance and durability analyses, linear-elastic fatigue crack growth analyses have been found to be quite adequate. However, for small crack growth from notches or holes, plasticity effects have been found to be significant and must be accounted for in the crack growth analyses [B-6]. To account for plasticity, a portion of the cyclic plastic-zone length (ω) was added to the crack length. Thus, the corrected cyclic plastic-zone effective stress-intensity factor is

$$(\Delta K_p)_{eff} = (S_{max} - S_o)\sqrt{(\pi d)}\,F \qquad \text{(B-1)}$$

where S_{max} is the maximum stress, S_o is the crack-opening stress, $d = c + \omega/4$, c is crack length and F is the boundary correction factor. The boundary correction factor accounts for the configuration (boundaries, holes, and crack shape) on stress-intensity factors. The $(\Delta K_p)_{eff}$ parameter is approximately equal to ΔJ_{eff}, which is proportional to the cyclic crack tip opening displacement. S_o is calculated from the FASTRAN code [B2].

For large-crack configurations, such as compact tension C(T) and middle-crack tension M(T) specimens, the cyclic plastic-zone correction is very small and may be neglected. Thus, in general, for any large-crack configuration, the effective stress-intensity factor range [B-7 and B-8] is given by

$$\Delta K_{eff} = U\,\Delta K = [(1 - S_o/S_{max})/(1 - R)]\,\Delta K \qquad \text{(B-2)}$$

Herein, the elastic effective stress-intensity factor, as given by equation B-2, is used in all correlations and analyses of fatigue crack growth rate data.

B.3 CONSTANT-AMPLITUDE LOADING.

Newman [B-9] developed steady-state, crack-opening stress equations from the plasticity-induced crack closure model for an M(T) specimen subjected to constant-amplitude loading at various stress levels, stress ratios (R), and constraint factors (α). Crack closure transients, before the crack-opening stresses stabilize under constant-amplitude loading, are not included in these equations. The FASTRAN model had to be exercised to determine these transient behaviors. Later, the FASTRAN model and the equations were modified to account for extreme crack growth rates, such as those under high loads or proof tests. Equations were then fit to the results from the model, which gave crack-opening stress (S_o) as a function of stress ratio (R), maximum stress level (S_{max}/σ_o), the constraint factor (α), and the amount of crack growth during a cycle [B-10]. Since the crack-opening stress equation was developed for an M(T) specimen, K-analogy [B-2 and B-11] is used to calculate the crack-opening stresses for other crack configurations. Here, it is assumed that the same K_{max} and ΔK will result in the same stabilized crack-opening stress. These equations are then used to correlate fatigue crack growth rate data in terms of ΔK_{eff} on M(T) and C(T) specimens.

B.4 CONSTRAINT EFFECTS.

In general, the plastic-zone size at a crack front increases as a crack grows in a metallic material under cyclic loading (constant applied maximum and minimum stresses). At low stress-intensity factor levels, plane-strain conditions should prevail, but as the plastic-zone size becomes large compared to thickness, a loss of constraint is expected (see reference B-5). This constraint loss has been associated with the transition from flat-to-slant crack growth behavior, as shown in figure B-1. Schijve [B-12] showed that the transition occurs at nearly the same fatigue crack growth rate over a wide range in stress ratios for an aluminum alloy. Since Elber's concept [B-8] correlates fatigue crack growth rates, then the transition should occur at the same ΔK_{eff}. This observation has been used to help select the constraint loss regime. Newman [B-10] developed an expression to predict the transition from flat-to-slant crack growth and the ΔK_{eff} at transition is given by

$$(\Delta K_{eff})_T = 0.5\, \sigma_o \sqrt{B} \qquad \text{(B-3)}$$

where σ_o is the flow stress and B is the material thickness. The range of the constraint loss regime, in terms of rate or ΔK_{eff}, is a function of thickness, but this relation has yet to be developed. Trial-and-error methods are currently used to establish the range in crack growth rates where the constraint loss regime will occur for a given material and thickness.

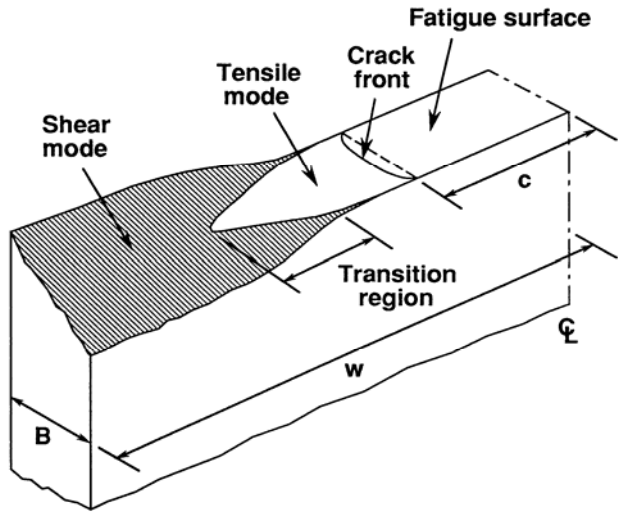

Figure B-1. Flat-to-Slant Fatigue Crack Growth Behavior in Metallic Materials

In the application of FASTRAN, the constraint loss regime is controlled by crack growth rates. For rates lower than a certain (input) value, the constraint factor is high (like plane strain), but if the rate is higher than another (input) rate, then the constraint factor is low (like plane stress). For intermediate rates, a linear relation on log of the rates is used to estimate the constraint factor between the upper and lower constraint values. The constraint factor only changes the forward plastic-zone size and crack surface displacements under the current loading. The crack growth model does not physically model the shear-lip or slant crack growth process under either constant- or variable-amplitude loading. Obviously, the crack growth process under variable-amplitude loading is quite complex and the FASTRAN model is a simple engineering approximation.

B.5 CRACK GROWTH RATE RELATION.

The crack growth relation used in FASTRAN is

$$dc/dN = C_{1i} (\Delta K_{eff})^{C_{2i}} [1 - (\Delta K_o/\Delta K_{eff})^p]/[1 - (K_{max}/C_5)^q] \qquad \text{(B-4)}$$

where C_{1i} and C_{2i} are the coefficient and power for each linear segment, ΔK_{eff} is the effective stress-intensity factor, ΔK_o is the effective stress-intensity factor at threshold, K_{max} is the maximum stress-intensity factor, C_5 is the cyclic elastic fracture toughness (usually C_5 is set equal to K_{Ie}, which is generally a function of crack length, specimen width, and specimen type), p and q are constants selected to fit test data in either the threshold or fracture regimes. Whenever the applied K_{max} value reached or exceeded C_5 (or K_{Ie}), then the specimen or component would fail (see equation B-4). The effective threshold stress-intensity factor range, ΔK_o, is expressed as a function of stress ratio and is:

$$\Delta K_o = C_3 (1 + C_4 R) \quad \text{for negative } C_4 \qquad \text{(B-5)}$$

or

$$\Delta K_o = C_3 (1 - R)^{C_4} \quad \text{for positive } C_4 \tag{B-6}$$

The values of p and q have ranged from 2 to 10 depending upon the material. A table lookup form is used for the power-law because many materials, especially aluminum alloys, show sharp changes in the crack growth rate curves at unique values of rates. These sharp changes have been associated with monotonic and cyclic plastic-zone sizes, grain sizes, and environments [B-13 and B-14].

B.6 FRACTURE.

Newman [B-15 and B-16] proposed the Two-Parameter Fracture Criterion (TPFC) to correlate fracture data and to predict failure loads on metallic materials. The TPFC equation is

$$K_F = K_{Ie} / (1 - m\, S_n/S_u) \text{ for } S_n < \sigma_{ys} \tag{B-7}$$

where K_F and m are the two fracture parameters; K_{Ie} is the elastic fracture toughness (elastic stress-intensity factor at failure); S_n is the net section stress; and S_u is the plastic hinge stress based on the ultimate tensile strength. For example, for an M(T) specimen S_u is equal to σ_u, the ultimate tensile strength, and for a pure bend specimen, $S_u = 1.5\ \sigma_u$. A similar equation was derived for $S_n > \sigma_{ys}$, see reference B-16. The m-value is both a material and configuration parameter. It is a function of material, thickness, and, in general, specimen type (tension, bending, etc.). For brittle materials, m = 0 and the fracture toughness K_F is equal to the elastic stress-intensity at failure (like, K_{Ic}, the plane-strain fracture toughness). However, for very ductile materials, m = 1 and the fracture toughness K_F is the elastic-plastic fracture toughness; and K_F is the largest limiting value for very large cracked panels, at very low failure stresses. For m = 1 and a very large K_F value, equation B-7 reduces to a net-section-stress-equal-plastic-hinge-stress ($S_n = S_u$) failure criterion. Once K_F and m are known for a material, thickness, and specimen configuration, then the K_{Ie} values can be calculated as

$$K_{Ie} = K_F / \{1 - m\, K_F /[S_u \sqrt{(\pi c)}\, F_n]\} \text{ for } S_n < \sigma_{ys} \tag{B-8}$$

for a given crack length and specimen width. Note that F_n is the usual boundary correction factor (F) on the stress-intensity factor with a net-to-gross section conversion [B-16], because the net section stress is used in equation B-7. For $S_n > \sigma_{ys}$, a more complicated equation is given in reference B-16.

B.7 REFERENCES.

B-1. Newman, J.C., Jr., "A Crack Closure Model for Predicting Fatigue Crack Growth Under Aircraft Spectrum Loading," ASTM STP 748, American Society for Testing and Materials, Philadelphia, Pennsylvania, 1981, pp. 53-84.

B-2. Newman, J.C., Jr., "FASTRAN II—A Fatigue Crack Growth Structural Analysis Program," NASA TM 104159, 1992.

B-3. Dugdale, D.S., "Yielding of Steel Sheets Containing Slits," *Journal of Mechanics and Physics of Solids*, Vol. 8, 1960, pp. 100-104.

B-4. Blom, A., Wang, G., and Chermahini, R., "Comparison of Crack Closure Results Obtained by 3-D Elastic-Plastic FEM and Modified Dugdale Model," *Localized Damage: Computer-Aided Assessment and Control*, M.H. Aliabadi, et al., eds., Computational Mechanics Publications, Springer-Verlag, Berlin, 1990, pp. 57-68.

B-5. Newman, J.C., Jr., Bigelow, C.A., and Shivakumar, K.N., "Three-Dimensional Elastic-Plastic Finite Element Analyses of Constraint Variations in Cracked Bodies," *Engineering Fracture Mechanics Journal*, Vol. 46, 1993, pp. 1-13.

B-6. Newman, J.C., Jr., "Fracture Mechanics Parameters for Small Fatigue Cracks," *ASTM STP-1149*, Larsen, J. and Allison, J.E., eds., 1992, pp. 6-33.

B-7. Elber, W., "Fatigue Crack Closure Under Cyclic Tension," *Engineering Fracture Mechanics*, Vol. 2, 1970, pp. 37-45.

B-8. Elber, W., "The Significance of Fatigue Crack Closure," *ASTM STP 486*, American Society for Testing and Materials, Philadelphia, Pennsylvania, 1971, pp. 230-242.

B-9. Newman, J.C., Jr., "A Crack-Opening Stress Equation for Fatigue Crack Growth," *International Journal of Fracture*, Vol. 24, 1984, R131-R135.

B-10. Newman, J.C., Jr., "Effects of Constraint on Crack Growth under Aircraft Spectrum Loading," *Fatigue of Aircraft Materials*, A. Beukers, et al., eds., Delft University Press, 1992, pp. 83-109.

B-11. McClung, R.C., "Finite Element Analysis of Specimen Geometry Effects on Fatigue Crack Closure," *Fatigue and Fracture of Engineering Materials and Structures*, Vol. 17, 1994, pp. 861-872.

B-12. Schijve, J., "Significance of Fatigue Cracks in Micro-Range and Macro-Range," *ASTM STP 415*, American Society for Testing and Materials, Philadelphia, Pennsylvania, 1967, pp. 415.

B-13. Yoder, G.R., Cooley, L.A., and Crooker, T.W., "On Microstructural Control on Near-Threshold Fatigue Crack Growth in 7000-Series Aluminum Alloys," *Scripta Metallurgica*, Vol. 16, 1982, pp. 1021-1025.

B-14. Piascik, R.S. and Gangloff, R.P., "Environmental Fatigue of an Al-Li-Cu Alloy: Part II. Microscopic Hydrogen Cracking Processes," *Metallurgical Transactions*, Vol. 24A, 1993, pp. 2751-2762.

B-15. Newman, J.C., Jr., "Fracture Analysis of Surface- and Through-Cracked Sheets and Plates," *Engineering Fracture Mechanics*, Vol. 5, 1973, pp. 667-689.

B-16. Newman, J.C., Jr., "Fracture Analysis of Various Cracked Configurations in Sheet and Plate Materials," ASTM STP 605, American Society for Testing and Materials, Philadelphia, Pennsylvania, 1976, pp. 104-123.